Towards a Setup for Narrowband Terahertz Generation Through Difference-Frequency Mixing of Chirped Ultrashort Pulses

MASTER THESIS

By
Isa Clementsson

Supervisor: Prof. Jörgen Larsson
Assistant Supervisor: Eric Nilsson

Division of Atomic Physics
Faculty of Engineering, LTH

LUND UNIVERSITY

October 17, 2023

Abstract

Terahertz radiation is a useful tool for inducing lower-energy excitations in matter, where it can be used to cause structural changes through direct interaction with the crystal lattice. Sub-picosecond optical pulses can be used to generate intense broadband terahertz pulses through optical rectification in nonlinear crystals, reaching peak electric fields of several MV/m and conversion efficiencies as high as a few percent. For certain applications it may be desirable to only generate terahertz frequencies within a narrow band. One such way, using broadband optical pulses, is through chirped-pulse beating, where two linearly chirped pulse copies are delayed relative each other in time, causing them to beat. This results in an output optical pulse with an intensity envelope modulated at a single beat frequency. When incident on a nonlinear crystal lacking inversion symmetry, such a modulated pulse generates difference-frequencies only within a narrow band, centered around the beat frequency of the intensity modulation.

This scheme for narrowband terahertz generation was implemented in the project, and an electro-optic sampling setup was built to characterize the temporal profile of the terahertz pulses. In the project, terahertz radiation was generated using the organic crystal DSTMS pumped with 1500 nm light from an optical parametric amplifier. Pulse characterization was done using the electro-optic crystals ZnTe and GaP with a frequency-doubled 750 nm probe pulse. Chirp and delay was implemented using a transmission grating chirp filter and a Michelson interferometer. Few-cycle terahertz pulses were successfully generated and sampled with electro-optic sampling. The pulse stretching and the delay between pulse copies were implemented, but narrowband terahertz pulses were not sampled with the electro-optic sampling within the time frame of the Master thesis.

Acknowledgments

I would like to thank my supervisor Prof. Jörgen Larsson. Jörgen, thank you for the many many hours spent in the lab with me, and for sharing your knowledge and enthusiasm for optics. Thank you for always having you door open for discussions, providing guidance and useful insights when I felt stuck and encouragement whenever I needed it. Also, thank you for coming up with the idea of such an interesting Master's project. However challenging at times, I feel that I have learnt a lot from it, and had a lot of fun along the way.

I would also like to thank my assistant supervisor Eric Nilsson. Eric, thank you for the many many hours spent in the lab with me and for always keeping a positive attitude when nothing seemed to work, thank you for staying late more than one evening so that I could work in the lab, and for always being helpful and having time for discussions.

I would also like to thank to Dr. Anders Persson for lending his camera to use in the electro-optic sampling setup, and for giving me access to the program he had developed for controlling it. I am also grateful for all helpful pointers and tips on LabVIEW, which were of big help, and for being generally helpful when I needed to borrow optics or mounts.

Generating terahertz pulses consisting of few frequencies

Matter is built up by atoms, consisting of a positively charged nucleus surrounded by a "cloud" of negatively charged electrons. Charged particles are affected by electric forces. An electromagnetic wave consists of a coupled time-varying electric and magnetic field, where the electric field exerts and electric force on the charged nucleus and the electrons, so that electromagnetic waves will interact with matter[1]. How energetic an electromagnetic wave is depends on its frequency, where higher frequencies correspond to higher energies.

Light can be used to induce changes in matter, since the electric field in the light wave interacts with the charged particles. The kind of interaction that occurs depends on how energetic the light is. Light in the optical region, which is light that we can see, often interacts with the electrons in an atom, giving them energy and moving them to higher energy states. Lower-energy electromagnetic waves, around terahertz frequencies, can cause molecules to rotate or vibrate. When many atoms are ordered periodically in a crystal, the atoms and molecules can vibrate relative each other only in certain ways, called vibrational *modes*. Vibrational modes can be excited with electromagnetic waves with terahertz frequencies and through this it is possible to change the structure of a material. The change in the material can later be probed by another light pulse to see how the vibrations decay in the crystal.

If the pulse used to excite the crystal contains many frequencies, it is not possible to control what vibrations are excited, but all vibrations that match a frequency in the pulse can be excited. Each vibrational mode then decays into other vibrational modes, and there is no way to tell which parts of the decay process is attributed to which original vibrational mode. If the crystal was instead excited with a pulse consisting of fewer frequencies, ideally few enough to only cover one vibrational mode in the crystal, it would be possible to investigate the decay processes in the material for a specific vibrational mode.

The goal of this project was to generate such a terahertz pulse, that consists of few frequencies. An infrared (1500 nm) pulse was used to pump a nonlinear crystal. When the intensity in the pulse is high and sent through a nonlinear crystal, the frequencies in the pulse can mix, so that other frequencies are emitted from the crystal. For the crystal and pulse used in the project, the frequencies that overlap in time are mixed by being subtracted with each other. This way, terahertz frequencies can be generated if the difference frequency between each mixing frequency pair is in the terahertz range. If the pump pulse frequencies overlap in time, the generated terahertz pulse will consist of many frequencies since many frequencies can mix. In order to generate a terahertz pulse that contains fewer frequencies, the frequencies in the pump pulse can be displaced linearly in time, so that they don't overlap anymore. If the pulse is then overlapped with an identical pulse copy, that arrives at a slightly different time and has its frequencies displaced in the same way, only a few frequencies from each pulse will overlap at a specific time, so that only specific pairs of frequencies can be subtracted in the crystal. The difference between the frequencies in each pair will be centered around a constant difference frequency, so that difference frequencies are generated only within a narrow band.

[1]The force exerted by the magnetic field can be neglected for weak field strengths.

Contents

1 Introduction

The electromagnetic spectrum covers a very wide range of frequencies, from exceptionally low Schumann resonances (7 Hz, corresponding to wavelengths on the order of 10^9 m) to extremely rapidly oscillating gamma frequencies (10^{18} Hz, corresponding to wavelengths on the order of 10^{-24}m). A continuously growing field is that of generating electromagnetic waves in the different wavelength ranges. In the transition from electronics to photonics lies the terahertz frequency region, a range of frequencies for which the generation methods remained undeveloped longer than for its neighboring bands. The terahertz band is usually defined between 0.1-10 THz, sometimes called the terahertz *gap* due to the historically lacking means of generating such frequencies.

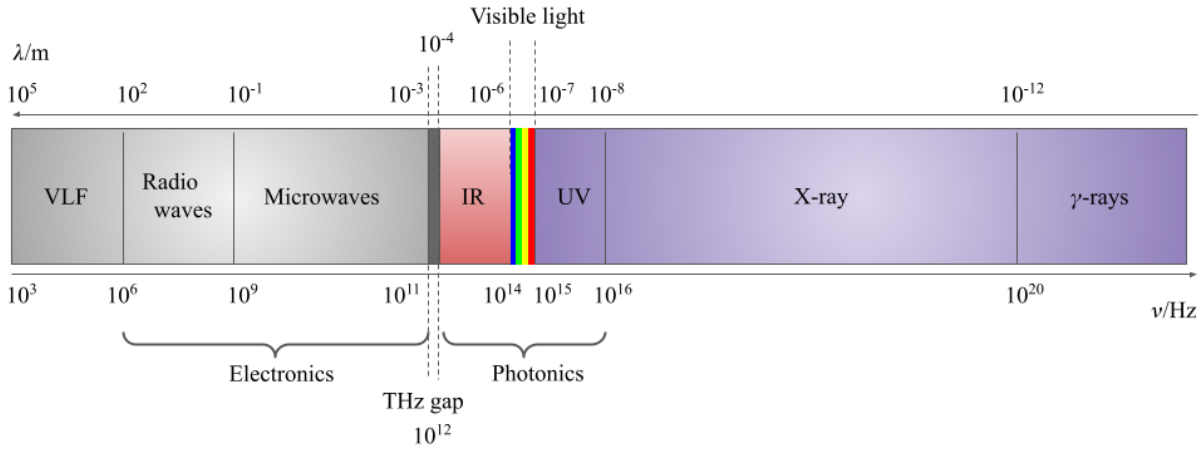

Figure 1: Electro-magnetic spectrum with approximate orders of magnitude, not to scale.

Terahertz generation is the main concern of this project, more specifically creating narrowband terahertz pulses. The field of terahertz science has grown a lot the past decades. A main reason is the development of femtosecond lasers and chirped pulse amplification, providing means of generating ultrashort, high-intensity pulses, allowing for portable, table-top optical setups, capable of producing intense few-cycle terahertz pulses. There has also been an increasing number of applications where terahertz radiation can be used as a tool in both industry and science, further piquing the interest for terahertz generation [2].

1.1 Terahertz science and narrowband applications

Electromagnetic waves, consisting of coupled time-varying electric and magnetic fields, interact with matter. The nature of the interaction depends strongly on the frequency of the incident electromagnetic wave. Electromagnetic waves in the terahertz frequency range are less energetic than, for instance, those in the optical regime, making terahertz frequencies an efficient tool for inducing lower-energy excitations for investigating structural dynamics in solids. It can cause molecules to rotate or spin, and induce vibrations in the crystal lattice [1].

Much of the properties of a material lie in its lattice geometry, which can be altered through excitation of vibrational modes. Energy quanta of the vibrational lattice modes are called phonons, and the allowed vibrational modes of the lattice are consequently

denoted phonon modes. Phonon modes can be excited indirectly using optical pump pulses, exciting valence electrons to the conduction band, and the system to a higher energy state. As the system decays back to its equilibrium, vibrational modes of the crystal are a part of the non-radiative decay process and are reached through electron-phonon coupling of the relaxing electrons [3]. Optical pulses excite the system to a higher energy level than necessary for phonon mode excitation and provide less control of what phonon modes are excited, since these are determined by the electron-phonon and subsequent phonon-phonon couplings in the system. Terahertz radiation is a direct way of interacting with the lower-energy resonances in the material, matching the energy level of dipole-active phonon modes, and is additionally not limited by amplitude-strengths determined by the coupling mechanisms [2, 3].

More techniques have been developed over the past few decades for generating intense, broadband pulses, with which phonon modes in crystals have been excited with high amplitudes, sufficient to induce nonlinear resonance phenomena in the lattice structure [2]. In order to excite specific phonon resonances, such as dipole active optical phonons, it can be advantageous to use narrowband terahertz pulses, since more of the energy is focused into exciting the specific phonon mode of interest.

1.2 Methods of terahertz generation

Terahertz can be generated in many ways. Intense and widely tunable terahertz pulses can be produced by free-electron lasers [2]. However, they present a relative inaccessibility compared to optical lasers, usually being parts of larger user facilities. Schemes developed for terahertz generation using femtosecond lasers are in general a more attractive approach, in which portable, table-top setups can be constructed, producing intense broadband terahertz pulses, reaching peak field as high as a few MV/m [2].

The first experiments in generating terahertz pulses with femtosecond lasers were done using photoconductive antennas. These are semiconductors over which a bias is applied. When a femtosecond laser pulse excites charge carriers across the bandgap of the semiconductor, they are accelerated by the bias field. The terahertz pulse from the induced current follows the temporal derivative of the pump intensity envelope [4, 5]. Another approach for generating terahertz radiation is through four-wave rectification, where a laser pulse and its second harmonic are focused to create a plasma. The fundamental can mix with the second harmonic and produce a fourth photon in the terahertz range [6].

1.2.1 Terahertz generation through optical rectification

An approach differing from the current-induced terahertz pulses described above is generating terahertz in nonlinear crystals, where the terahertz pulses originate from an induced nonlinear polarization density in the material. This is the method of terahertz generation used in the project. A subpicosecond pulse, with a bandwidth of several terahertz, can be used to generate a terahertz pulse through optical rectification, where difference-frequencies of the pump pulse spectral content are generated, corresponding to an output pulse centered in the terahertz band. Neglecting dispersion effects, the induced nonlinear polarization density follows the temporal derivative of the pump intensity envelope, so that few-cycle terahertz pulses can be created [5].

One of the first crystals used to generate terahertz radiation through optical rectification was the semiconductor crystal ZnTe. Semiconductor crystals are limited to pump pulses of lower intensity due to nonlinear absorption over the bandgap for higher intensities. Pumping with longer wavelengths can decrease the effect, but semiconductor crystals remain at relatively low conversion efficiencies around 10^{-4} [2]. While semiconductor crystals in general have good phase-matching between terahertz and pump wavelengths, the nonlinear coefficient is relatively low. Ferroelectric crystals, such as $LiNbO_3$, have significantly higher nonlinear coefficient, but poor phase-matching. A tilted-pulsefront technique (TPFT) can be used to compensate for the bad phase-matching, which has resulted in conversion efficiencies as high as 2-3% when cooling the crystal [2].

Both semiconductor and ferroelectric crystals have the apparent advantage of phase-matching (TPFT phase-matching) when pumped by wavelengths around 800 nm, within the tuning range of the Ti:Sapphire laser. Another group of crystals are organic crystals, examples being DSTMS, DAST and OH1, with exceedingly high nonlinear coefficients. Conversion efficiencies of a few percent, peak electric fields exceeding 1 MV/m and frequencies ranging 0.1-8 THz (DSTMS, DAST) and 0.1-4 THz (OH1) can be achieved by pumping with wavelengths between 1.2-1.6 μm, with respective optima around 1500 nm (DSTMS, DAST) and 1300 nm(OH1) [9]. This results in the need for an optical parametric amplifier, if using a Ti:Sapphire laser, to up-convert the wavelengths to longer ones. Relatively new lasers for longer wavelengths, such as the Erbium-doped laser [10] together with post-compression of the pulses, or the Cr:Frostrite laser [9] centered around 1200 nm are also alternatives, providing more average power to the frequency-mixing process.

1.2.2 Narrowband terahertz generation

Optical rectification of broadband, transform-limited pulses in nonlinear media results in a broadband, few-cycle output from the multitude of frequencies that can mix. For some applications it is of interest to generate terahertz pulses with narrower spectra.

A scheme for narrowband terahertz generation using chirped-pulse beating was proposed and implemented by Weling et. al. using a photoconductive antenna [11, 12]. By linearly chirping two pulses and introducing a relative temporal delay between the two, the intensity envelope of the resulting pulse is modulated at a single beat frequency. By exciting the semiconductor antenna with the modulated pulse, a multi-cycle, narrowband terahertz pulse can be generated, centered around the beat frequency of the intensity modulation. This scheme can be implemented for optical rectification in crystals as well, where the modulated pulse introduces a corresponding modulation of the nonlinear polarization density in the crystal, through which the electric field of the terahertz pulse is controlled. This has been done in, for instance, $LiNbO_3$ [13], ZnTe [15] and in organic crystals such as DSTSMS [14, 16], achieving bandwidths narrower than 1 THz.

Since the nonlinear polarization density depends on the second-order susceptibility, $\chi^{(2)}$, as well, an alternate approach to modulating the pump pulse is modulating the nonlinear coefficient of the generation crystal [17]. Narrowband terahertz pulses have been generated using periodically poled $LiNbO_3$, where the sign of $\chi^{(2)}$ is periodically inverted. Each domain contributes a half-cycle to the electric field of the terahertz pulse [18, 19]. A drawback to modulating the material properties instead of the pump pulse is

that the center frequency is not tunable, since this would require modifying the poling period of the material. Through chirped-pulse beating, the center frequency can be continuously tuned by either varying the chirp rate or the relative delay between pulse copies.

1.3 Terahertz pulse characterization

Terahertz radiation can be detected with terahertz powermeters and cameras sensitive to those wavelengths, but none of these can reconstruct the temporal profile of the pulse. This is a general problem when characterizing ultrashort pulses, where the pulses are too short for the rise-time of conventional photodetectors to be sufficient in representing their temporal profiles. Commonly, other light pulses that are (ideally) much shorter than the pulse of interest are used to sample different parts of the short pulse, by changing the relative delay between pulses [20].

In electro-optic sampling, the terahertz pulse is used to induce a birefringence in a nonlinear crystal through the Pockels effect. A probe pulse is used to probe the induced birefringence, which will rotate the polarization of the probe pulse. The rotation of the probe pulse is linearly related to the electric field in the terahertz pulse, so that by measuring the rotation, the electric field of the terahertz pulse can be reconstructed when varying the relative delay of pump and probe pulses to overlap with different parts of the terahertz pulse [29].

The process can be considered as a form of frequency mixing, and an "inverse optical rectification". In optical rectification, two frequencies of similar frequencies mix to produce a quasi-DC output frequency (the terahertz), while in electro-optic sampling the quasi-DC terahertz pulse is instead mixed with a significantly higher frequency (the probe pulse), and results in another photon of similar frequency, with a changed polarization. Measuring the amount of photons of different polarization is thus a measurement of how many terahertz photons there are at a certain location along the pulse envelope [29].

1.4 The goal of the project

This Master's project aimed at building an experimental setup for generating narrowband terahertz pulses through optical rectification of chirped-and-delayed pulses in an organic crystal, as well as building an electro-optic sampling setup for characterizing the terahertz pulses. An implicit goal of the experimental setup is to be able to generate narrowband terahertz pulses centered around 5.8 THz, corresponding to a phonon resonance in InSb. Although not the formal goal of the thesis, it would at times influence the choices made during the project. In the final outlook, possible improvements of the setup are briefly discussed, with consideration to reaching the specific phonon resonance.

2 Theoretical background

This project is concerned with constructing a setup for generating narrowband terahertz pulses through difference-frequency mixing of chirped-and-delayed, ultrashort pulses, making the topics of optical pulses, terahertz generation through optical rectification and pulse characterization with electro-optic sampling of apparent interest. These areas are introduced in the following sections.

2.1 Chirped ultrashort pulses

A pulsed electromagnetic wave is defined as an electric field of finite duration in time and is as such, by necessity of the inverse time-frequency relation, a superposition of many frequencies. Ultrashort (sub-picosecond) pulses are very narrow in time, and consequently extend over an extremely wide frequency band. Creation of such pulses often employ mode-locked lasers, in which the pulses form from a superposition of a wide spectrum of in-phase cavity modes. All pulses in this project are approximated as Gaussian, and consequently have an intensity profile such that their scalar complex wave function can be written on the form [20]:

$$E(t) = A(t)e^{j\omega_0 t} = E_0 e^{-t^2/\tau^2} e^{j\varphi(t)} e^{j\omega_0 t} \tag{1}$$

In equation 1, the first two factors contain information of the shape of the pulse envelope, and the last two describe the pulse center frequency and how the rapidly oscillating carrier frequency varies across the pulse duration. The phase function, $\varphi(t)$, will be an important concept for the project, since it describes more specifically *how* the carrier frequency varies. An arbitrary, nonlinear phase function $\varphi(t)$ can be expanded in a series [20]:

$$\varphi(t) \quad = \quad \varphi_0 \; + \; \frac{\partial\varphi}{\partial t}t \; + \; \frac{1}{2}\frac{\partial^2\varphi}{\partial t^2}t^2 \; + \; \frac{1}{6}\frac{\partial^3\varphi}{\partial t^3}t^3 \; + \; ... \quad \approx \quad \varphi_0 \; + \; \omega_0 t \; + \; \frac{1}{2}\alpha t^2 \tag{2}$$

where orders higher than the second are neglected in the expression. The first term in equation 2 describes the phase offset of the carrier wave relative the pulse envelope and the second term contains the center angular frequency, ω_0, of the pulse. α is the second order derivative, and conventions for describing it can differ. In this report, α is denoted as the *chirp rate*[2], defined through $\alpha = \frac{\partial^2\varphi}{\partial t^2}$.

The phase function of a pulse is given by the frequency of its oscillating electric field. The phase function describes the phase offset between carrier wave and envelope. The first derivative in the Taylor series expansion describes how the phase offset of the electric field vary in time. If the phase offset varies linearly, this corresponds to a constantly oscillating electric field. We call this frequency the carrier frequency, or the center frequency, and denote it by ω_0. The second-order derivative describes a quadratic dependence of the phase-offset with respect to time, which must correspond to a frequency that varies across the pulse envelope. A pulse with varying frequency is said to be *chirped* [20].

[2]Other common terminology is the *sweep rate* or the *frequency sweep*. In Saleh and Teich's *Fundamentals of photonics*, an alternate descriptor called the *chirp coefficient* is introduced, and defined as: $a = \frac{1}{2}\varphi''\tau^2$.

The frequency of electric field is related to the phase function through [20]:

$$\omega_i = \omega_0 + \frac{\partial \varphi}{\partial t} \tag{3}$$

This can be understood from the following observation: at a certain time, t, the total phase is given by $\varphi_0 = \omega_0 t + \varphi(t)$. One period later, the total phase is $\varphi_1 = \varphi_0 + 2\pi = \omega_0(t+T) + \varphi(t+T)$. The total phase difference between the two times is given by $\varphi_1 - \varphi_0 = 2\pi = \omega_0 T - (\varphi(t+T) - \varphi(t))$. Dividing by the period T, the left-hand side is recognized as an angular frequency, which we denote the instantaneous (angular) frequency. For small T, which is the case for a rapidly oscillating electric field, the last term on the right-hand side approaches the definition of a derivative, so that:

$$\omega_i = \frac{2\pi}{T} = \omega_0 + \lim_{T \to 0} \frac{\varphi(t+T) - \varphi(t)}{T} = \omega_0 + \frac{\partial \varphi}{\partial t} \tag{4}$$

In the project only phase function nonlinearities up to the second order are considered, i.e. $\varphi''' \approx \varphi^{(4)} \approx ... \approx 0$. Then, the instantaneous frequency is a linear function of time, with a slope that is proportional to the chirp rate, α:

$$\nu_i = \nu_0 + \frac{\alpha t}{2\pi} \tag{5}$$

Un-chirped pulses have the minimum time-bandwidth product, which for a Gaussian pulse is $\tau \Delta \nu = 0.44$. Temporally chirped pulses have frequencies that are displaced in time, from which it can be understood intuitively that an un-chirped and a chirped pulse with the same spectra must result in the chirped pulse having a longer duration in time, since its spectral content is spread over a wider temporal range. A chirped and an un-chirped pulse are illustrated in figure 2.

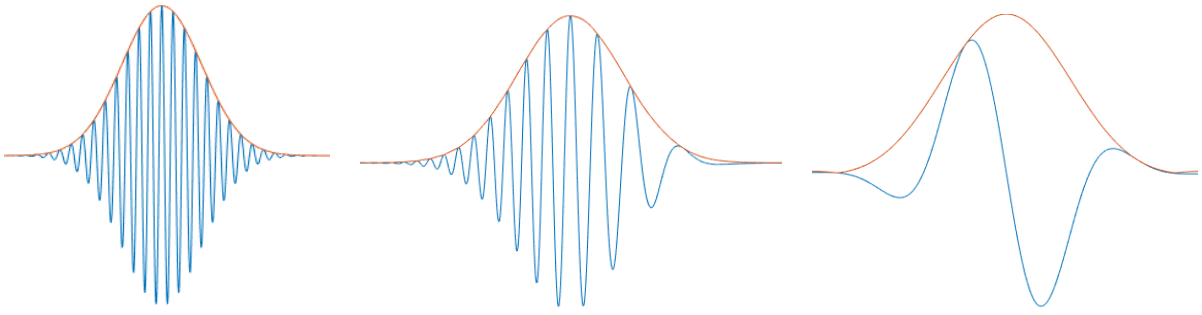

(a) (b) (c)

Figure 2: Illustration of relevant pulse types, where the blue function is the complex wave function, and the red is the complex envelope. (a) un-chirped pulse, (b) chirped pulse, (c) single-cycle pulse.

Another concept which will be of interest when discussing terahertz generation is single-, few- and multi-cycle pulses. A single-cycle pulse has an electric field that only completes one oscillation across the pulse envelope. Few- and multi-cycle pulses are analogously pulses whose electric field completes a few or multiple oscillations across the pulse envelope. A single-cycle pulse is illustrated in figure 2c.

2.1.1 Transmission grating chirp filters

Pulses become naturally chirped when propagating through media with a refractive index n≠1 due to a frequency-dependent modulation of the spectral phase of the pulse. The chirp from propagating through a material is in general small, and is as such seldom the conventional approach when actively introducing large amounts of chirp to a pulse. A more common approach is using angular dispersion chirp filters with diffraction gratings or prisms.

An output pulse from a chirp filter is described through a temporal convolution of the input pulse and the impulse response of the chirp filter. A convolution in temporal domain represents a multiplication in spectral domain, and it is therefore often more convenient to carry out the calculations of a pulse propagating through a dispersive material in the spectral domain. Going back and forth between temporal and spectral domain with the Fourier transform and the inverse Fourier transform, the temporal representation of the output pulse is given by [11, 20]:

$$E_{out}(t) = \mathcal{F}^{-1}\left\{\mathcal{F}\left\{E_0 e^{-\frac{t^2}{\tau^2}} e^{i\varphi(t)}\right\} e^{i\Psi(\omega)}\right\} \tag{6}$$

for a pure phase-filter and an initially un-chirped pulse. From equation 6 it is clear that when a pulse propagates through a phase filter, it acquires an additional spectral phase, Ψ, which is added to the spectral phase of the incident pulse. The spectral phase of the chirp filter can be expanded in a Taylor series around the center angular frequency, ω_0, of the propagating pulse. Omitting orders higher than two results in an expression [20, 25]:

$$\begin{aligned}\Psi(\omega) = \Psi(\omega_0) + \frac{\partial\Psi}{\partial\omega}(\omega-\omega_0) + \frac{1}{2}\frac{\partial^2\Psi}{\partial\omega^2}(\omega-\omega_0)^2 + \frac{1}{6}\frac{\partial^3\Psi}{\partial\omega^3}(\omega-\omega_0)^3 + ... \approx \\ \approx \Psi_0 + \tau_0(\omega-\omega_0) + \frac{1}{2\mu}(\omega-\omega_0)^2\end{aligned} \tag{7}$$

The first term in the series expansion adds a phase offset, and does not affect the shape of the pulse. The first order derivative corresponds to a temporal shift of the entire pulse packet after passing through the filter, and is called the group delay, τ_0 [20]. The higher orders account for the frequency-dependence of the spectral phase added by the chirp filter. The second-order derivative of the spectral phase is called the group delay dispersion (GDD). As the name suggests, it describes that different frequencies experience different "group" delays, due to the frequency-dependent spectral phase acquired, resulting in pulse broadening.

There are many ways of defining parameters to describe the group-delay dispersion of a chirp filter. In this report, the GDD is defined as[3]: $\Psi'' = \frac{1}{\mu}$. Assuming an initially un-chirped pulse of duration τ_0, and a large group delay dispersion ($1/\mu \gg \tau_0^2$), the temporal phase of the pulse leaving the chirp filter can be approximated to be related to the group delay dispersion, $1/\mu$, introduced by the chirp filter as [25]:

[3]Other common notations for the group delay dispersion are for example: $\Psi'' = \phi_2$ [27] and $\Psi'' = \frac{2}{\mu}$ [9]. In Saleh and Teich's *Fundamentals of Photonics*, and alternate descriptor called the *chirp coefficient* is introduced, and defined as: $b = \frac{\Psi''}{2\pi^2}$ [20].

$$\varphi(t) = \omega_0 t - \frac{\mu}{2} t^2 \tag{8}$$

so that a pulse propagating through a chirp filter with a spectral phase of negligible orders higher than two results in a linearly chirped pulse with a chirp rate that, for large chirps, equals the inverse of the group delay dispersion introduced by the chirp filter. We remember that these were the kinds of pulses that were of interest to us in the project - the linearly chirped ones. Thus, the chirp filters of interest in the project are those with which we can introduce a controlled amount of group-delay dispersion. The group delay dispersion is determined by the characteristics of the chirp filter, differing, for instance, for materials, gratings and prisms. In this project the pulses are chirped using transmission gratings. These are wavelength-dependent light-deflector, often constructed of a periodically varying refractive index, so that they obtain a wavelength-dependent deflection angle. The relationship between deflection angle, θ_q, angle of incidence, θ_i, grating period, Λ, and wavelength of incident light, λ, is described by the grating equation [20]:

$$\sin(\theta_q) = \sin(\theta_i) + q\frac{\lambda}{\Lambda} \tag{9}$$

where q is the diffraction order. Using four transmission gratings it is possible to construct a temporal pulse stretcher that does not increase the spatial width of the exiting pulse [20]. A schematic of this is shown to the left in figure 3. From this we see that shorter wavelengths (towards λ_{min} in the figure) travel a longer distance between the two gratings, and acquire a larger spectral phase shift than the longer wavelengths. By vertically translating the beam[4] and sending it back with a hollow-roof mirror, the same effect can be achieved with only two transmission gratings. A schematic of the two-grating chirp filter is shown in figure 3b.

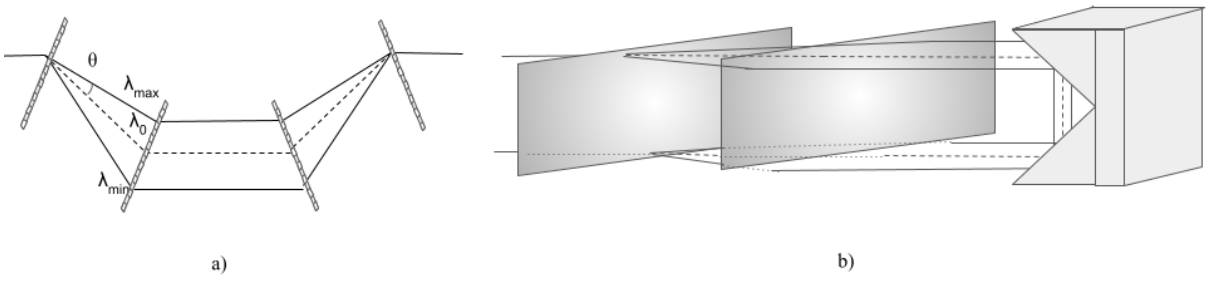

Figure 3: Two different implementations of angular-dispersion chirp filters, (a) with four transmission gratings and (b) with two transmission gratings and a hollow-roof mirror.

With notations: c being the speed of light in vacuum, l_0 the distance between the gratings, Λ the grating period and θ_i the angle of incidence, the group delay dispersion for two parallel transmission gratings can be shown to be [25, 26]:

[4]Note that in order to remove the spatial chirp, the translation has to be perpendicular to the plane of deflection from the gratings. If the beam is reflected back in the same horizontal plane, the wavelengths will invert relative the center wavelength on their second passage through the gratings, and the spatial chirp will be increased instead of canceled for the exiting pulse.

$$\frac{1}{\mu} = -\frac{4\pi c l_0}{\omega_0^3 \Lambda^2}\left[1 - \left(\left(\frac{2\pi c}{\omega\Lambda} - \sin(\theta_i)\right)^2\right)\right]^{-3/2} \tag{10}$$

The chirped-pulse duration, τ, after a chirp filter with group delay dispersion $1/\mu$, for an initially un-chirped pulse of duration τ_0 is given by [11]:

$$\tau = \tau_0\sqrt{1 + \frac{4}{\mu^2(\tau_0\sqrt{log(2)})^4}} \tag{11}$$

2.2 Terahertz generation through optical rectification

The overview of terahertz generation provided in the introduction showed that there are many approaches to generating terahertz pulses. Since optical rectification is the generation method used in this project, this will be the one considered more carefully.

2.2.1 Optical rectification

An electromagnetic wave propagating in linear, homogeneous, non-dispersive media induces a time dependent polarization density in the material, that for weak electric fields is linearly related to the incident electric field. For strong electric fields the linear model of the polarization density breaks. Assuming incident electric fields that are small compared to inter-atomic forces, the polarization density can be expanded in a Taylor series around $\vec{E} = 0$ [20]:

$$\vec{P}(t) = \varepsilon_0\chi\vec{E}(t) + \varepsilon_0\chi^{(2)}\vec{E}(t)^2 + \varepsilon_0\chi^{(3)}\vec{E}(t)^3 + ... \tag{12}$$

This report will only consider second-order nonlinear effects, i.e. nonlinear polarization densities dependent on the square of the electric field, since these are the only ones contributing to the terahertz generation. The nonlinear polarization density results in a multitude of phenomena, one of which is called frequency mixing and is the additional output at sum- and difference-frequencies of the spectral content of the incident electric field. The concept can be illustrated mathematically by considering two monochromatic light sources $\vec{E}_1$ and $\vec{E}_2$ incident on a second-order nonlinear material. This results in an expression for the polarization density:

$$\begin{aligned} P_{NL} = \varepsilon_0\chi^{(2)}\left(E(\omega_1)\exp[j\omega_1 t] + E(\omega_2)\exp[j\omega_2 t]\right)^2 = \\ \frac{\varepsilon_0\chi^{(2)}}{2}\left(|E(\omega_1)|^2 + |E(\omega_2)|^2 + \right. \\ E^2(\omega_1)\exp[j2\omega_1 t] + c.c. + E^2(\omega_2)\exp[j2\omega_2 t] + c.c. \\ E(\omega_1)E(\omega_2)\exp(j[\omega_1+\omega_2)t] + c.c. \\ \left. E(\omega_1)E^*(\omega_2)\exp(j[\omega_1-\omega_2)t] + c.c.\right) \end{aligned} \tag{13}$$

where

$$E(t) = \Re\left(E(\omega)\exp[i\omega t]\right) = \frac{1}{2}\left(E(\omega)\exp[i\omega t] + E^*(\omega)\exp[-i\omega t]\right) \tag{14}$$

The frequencies at which the polarization density oscillate appear in the exponents in equation 13. These are the possible frequencies originating from the mixing process. It is apparent that the two fundamental cases of frequency mixing are sum and difference frequency generation, and that these processes further branch into two special cases when the two mixed frequencies are the same, called second harmonic generation (sum-frequency mixing) and optical rectification (difference-frequency mixing) respectively [20].

If the nonlinear process takes place in a medium in which the pump field and the generated field propagate with different velocities, this can cause the new frequencies created at each point in the material to superpose destructively at the exit. This imposes phase matching conditions on the process, in which the phase-mismatch between the pump and the generated frequencies needs to be small enough to generate a strong-field output of the mixed frequencies. Phase-matching is described more thoroughly in section 2.4.

2.2.2 Terahertz generation

Ultrashort pulses comprise many frequencies. For un-chirped pulses, all frequencies overlap in time and can mix in a nonlinear material, for sufficiently high pulse intensities. This concept is illustrated in figure 4. Figure 4a shows the spectrum of the optical pulse, and two frequencies are noted at different locations in the spectrum. Figure 4b shows the instantaneous frequency as a function of time for the spectrum in 4a, and the difference frequencies Ω_{ln} that can originate from the parametric interaction process. When all frequencies arrive at the same time, the instantaneous frequency is a vertical line (infinite chirp rate). Since many frequencies overlap in time, producing many difference-frequencies, this results in a broadband output pulse. For sub-picosecond pulses, having bandwidths in the terahertz range, the difference-frequencies will lie in the terahertz band. Since the terahertz pulses have considerably lower frequency ($\sim 10^{12}$ compared to $\sim 10^{14}$) the process is often called optical rectification, even though the generated frequencies are not strictly DC [20].

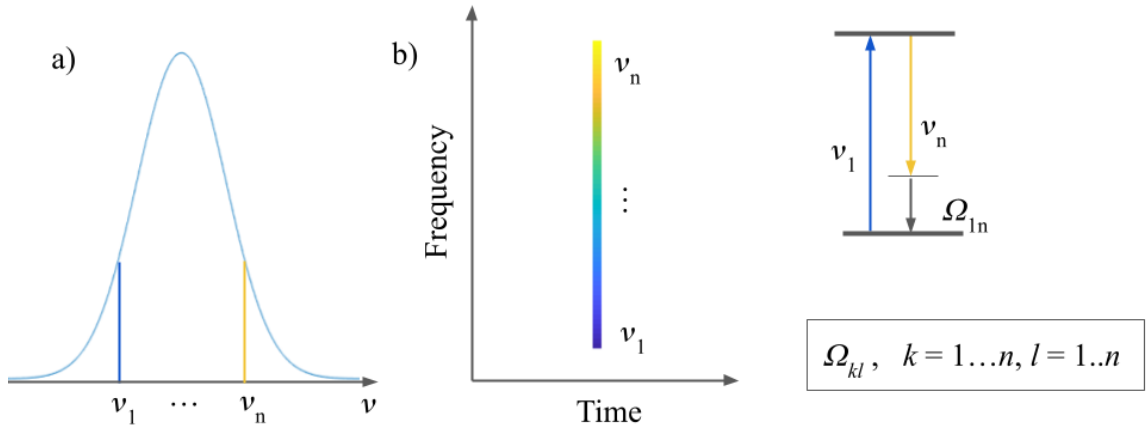

Figure 4: A broadband, near-transform limited pulse contains a multitude of frequencies overlapping in time, which can mix to produce difference-frequencies.

Figure 4 has illustrated how the spectral content and its relative displacement in time affects the generated terahertz pulse spectrum. Considering the temporal shape

of the terahertz pulse, we look to the electric field of the incident pump pulse for the rectification process. To determine the shape of the electric field of the terahertz pulse, the nonlinear wave-equation of the optical rectification process can be solved, as is done in [5, 7, 8]. This results in an expression of the generated terahertz electric field which is proportional to the second-order polarization density induced in the material by the pump pulse, when neglecting absorption and phase-mismatch. The polarization density follows from the intensity envelope of the pump pulse through $P_{NL} = \varepsilon_0 \chi^{(2)} E^2 = \varepsilon_0 \chi^{(2)} I$. Since the electric field of the terahertz radiation follows from the nonlinear polarization density, it ultimately follows from the shape of the intensity envelope of the pump pulse. Thus, the resulting shape of the terahertz electric field from a Gaussian intensity envelope generates a Gaussian, half-cycle terahertz pulse [5, 7, 8].

How quickly an electro-magnetic wave reaches the far-field region depends on its wavelength. Longer wavelengths diverge more, and reach the far-field faster than smaller wavelengths [20]. The source of the terahertz radiation (the nonlinear polarization density in the crystal) can be considered as an aperture with a diameter equal to the beam diameter of the pump laser. A measure for when an electro-magnetic wave emerging from an aperture reaches the far-field region is the Fresnel number, N_F [20]:

$$N_F = \frac{a^2}{\lambda d} \tag{15}$$

where a is the radius of the aperture, λ is the wavelength and d is the distance traveled. Small («1) Fresnel numbers imply that the electro-magnetic wave is in the far-field. For an aperture of size 1 mm and a wavelength of 0.3 mm (corresponding to 1 THz), the Fresnel number is 0.03 after 10 cm propagation; already in the far-field. If the wavelength was instead 800 nm (375 THz), the wave would have to travel 40 m before reaching the same Fresnel number.

Since terahertz radiation has a (relatively) long wavelength, it reaches the far-field after shorter propagation distances than optical wavelengths. As a consequence, terahertz radiation is often considered in the far-field. In the far-field, the shape of the electric field is related to the nonlinear polarization density (and thus the pump pulse intensity envelope) through a temporal derivative [5]. It thus follows that in the far-field, the electric field of the terahertz pulse generated from optical rectification makes a single cycle (two half-cycles), as illustrated in figure 5.

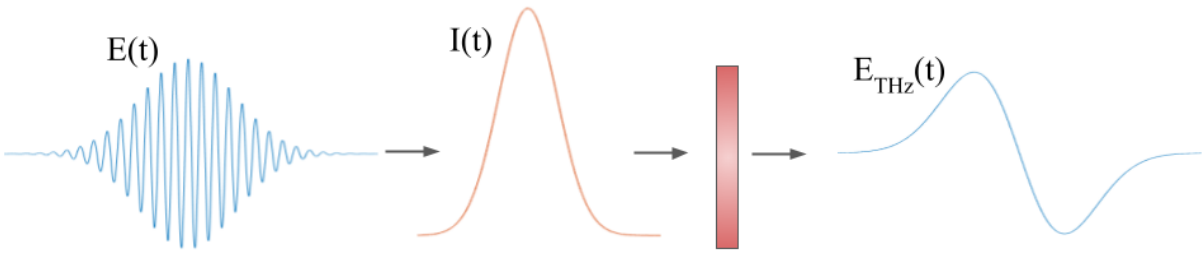

Figure 5: The shape of the electric field of a terahertz pulse originating from an optical rectification process follows the temporal derivative of the intensity envelope of the pump pulse.

When phase-mismatch is considered, this results in spectral narrowing of the terahertz

pulse, due to a larger accumulated phase-mismatch for frequencies further away from the center frequency (for which phase-matching is presumably optimized). This results in a distortion of the temporal electric field, by more cycles being added to the temporal pulse shape and increasing the pulse duration [7, 8]. This short discussion can be considered a precursor to the following scheme for narrowband terahertz generation.

2.2.3 Narrowband terahertz generation through chirped-pulse beating

As alluded to in the last paragraph, adding more cycles to the temporal terahertz pulse so that the pulse duration increases narrows the pulse spectrum. In the spectral domain, this can be described as imposing constraints on what frequency-mixing processes are efficient, or even possible. These ideas are the building blocks of the scheme for narrowband terahertz generation through chirped-pulse-beating.

Weling et. al. [11] proposed the chirp-and-delay scheme for generating narrowband terahertz pulses from broadband laser pulses in 1996 (1993 [12]), where they introduced linear chirp to a broadband pulse, split it into two pulse copies, and recombined the two copies with a relative delay between them. We start by considering how this changes the spectral representation of frequency mixing in the above section. When a pulse is linearly chirped, the spectrum in figure 4a remains the same, but the instantaneous frequency changes, since different frequencies will arrive at different times. A second, time-delayed, pulse copy, with the same chirp rate can be seen to the right in figure 6. Only frequencies that overlap in time can mix, and will generate a new photon at the difference frequency Ω_{beat}. Due to the pulses being linearly chirped, the frequency-difference between temporally overlapping frequencies will be constant. This way, a constraint on the frequency-mixing process has been introduced, so that the generated difference-frequencies are centered within a narrower band around Ω_{beat}.

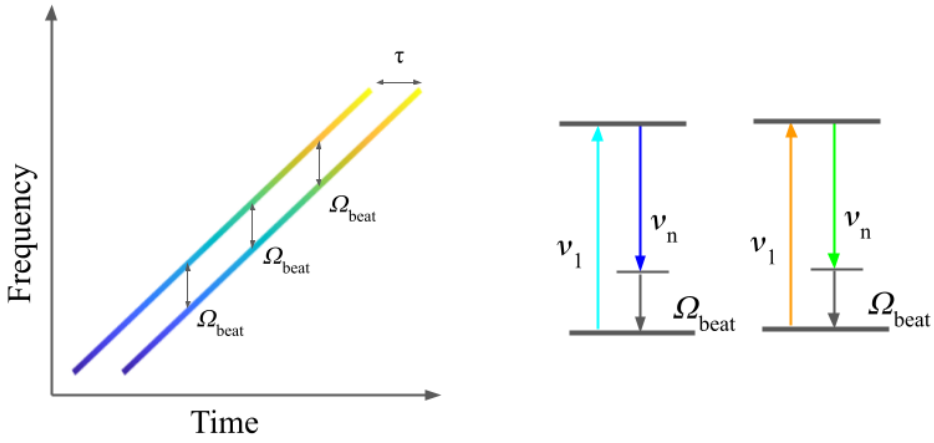

Figure 6: Schematic of the chirped-pulse beating scheme to generate narrowband terahertz pulses. Two interfering linearly chirped pulses result in a superposition pulse of a single beating frequency, Ω_{beat}.

Following the structure of the previous section, we now consider the temporal shape of the terahertz electric field from the intensity envelope of the pump pulse. When two pulses overlap, with a relative time delay, the frequencies in the pulses will beat,

resulting in a modulation of the total intensity envelope of the interfering pulses. The modulation will be of a single frequency, as will be derived shortly, corresponding to the beat frequency in the mixing process. This will consequently introduce a modulation to the electric field of the terahertz pulse, since it follows from the induced nonlinear polarization density in the material, and thus consequently from the shape of the intensity envelope of the pump pulse for the rectification process. This is illustrated in figure 7. The fringe pattern in the intensity envelope results in a multi-cycle terahertz pulse, where the fringe-spacing determines the frequency of the electric field. In the temporal domain, chirped-pulse beating can thus be interpreted as a pulse-shaping scheme, where the shape of the terahertz pulse is controlled by the modulation of the pump pulse.

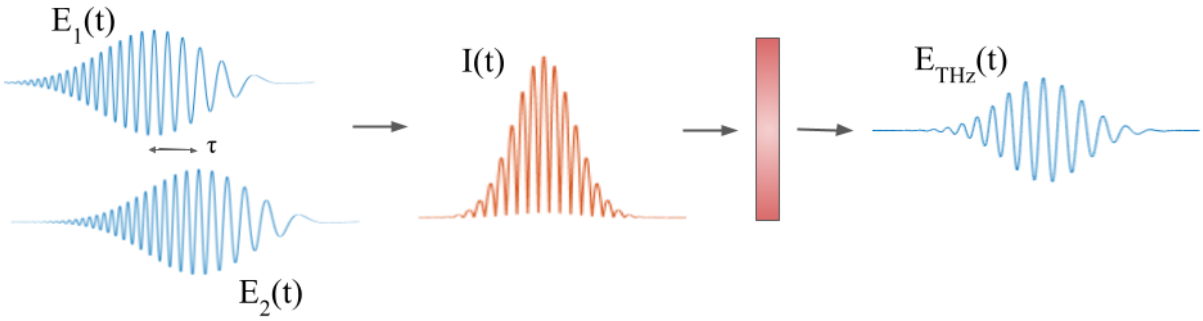

Figure 7: The shape of the electric field of a terahertz pulse originating from an optical rectification process follows the temporal derivative of the intensity envelope of the pump pulse.

To formally derive the expression for the intensity modulation, consider a linearly chirped pulse with amplitude E_0, pulse duration at full-width at half max τ, center angular frequency $\omega_0 = 2\pi\nu_0$ and chirp rate μ:

$$E(t) = E_0 e^{-t^2/\tau^2} e^{j(\omega_0 t - \frac{\mu}{2}t^2)} \tag{16}$$

interfering with a copy of itself, delayed a time $\Delta\tau$. The total electric field can be written as $|E(t)+E(t-\Delta\tau)|^2$ or equivalently as $|E(t-\Delta\tau/2)+E(t+\Delta\tau/2)|^2$. Choosing the second way of expressing this results in more terms canceling when calculating the interference so that the total interference can be written as:

$$\begin{aligned} I(t) = \left|E\left(t-\frac{\Delta\tau}{2}\right)+E\left(t+\frac{\Delta\tau}{2}\right)\right|^2 = |E_-|^2+|E_+|^2+E_-E_+^*+E_-^*E_+ = \\ I_0\left(\exp\left[\frac{-2(t-\Delta t/2)^2}{\tau^2}\right]+\exp\left[\frac{-2(t+\Delta t/2)^2}{\tau^2}\right]\right. \\ \left.+\exp\left[-\frac{2t^2}{\tau^2}\right]\exp\left[-\frac{\Delta\tau^2}{2\tau^2}\right]\left(\exp\left[-i\left(\omega_0\Delta\tau+\mu\Delta\tau t\right)\right]+\exp\left[i\left(\omega_0\Delta\tau+\mu\Delta\tau t\right)\right]\right)\right) = \\ I_0\left(\exp\left[\frac{-2(t-\Delta t/2)^2}{\tau^2}\right]+\exp\left[\frac{-2(t+\Delta t/2)^2}{\tau^2}\right]+\exp\left[-\frac{2t^2}{\tau^2}\right]\exp\left[-\frac{\Delta\tau^2}{2\tau^2}\right]cos(\omega_0\Delta\tau+\mu\Delta\tau t)\right) \end{aligned} \tag{17}$$

where Euler's formula $\cos(x) = \left(e^{ix}+e^{-ix}\right)/2$ is used in the last step. The second term in the cosine corresponds to the beat angular frequency. Thus, the beat frequency

of the chirped pulses is directly proportional to the chirp rate, μ, and the relative delay, $\Delta\tau$, between the pulses:

$$\nu_{beat} = \frac{\omega_{beat}}{2\pi} = \frac{\mu\Delta\tau}{2\pi} \tag{18}$$

The fringes in the intensity envelope are mathematically represented by the cosine in equation 17, where the fringes per second in the interferogram correspond to the beat frequency [20].

The bandwidth of the terahertz pulse is given by the Fourier transform of its electric field [11, 12], and can related to the bandwidth of the optical pump pulse through:

$$\Delta\nu = \sqrt{2}\Delta\nu_{laser}\left(\frac{\tau_0}{\tau}\right) \tag{19}$$

where τ_0 is the initially, un-chirped pulse duration, τ is the chirped-pulse duration of the beating pulses and $\Delta\nu_{laser}$ is the bandwidth of the pump pulse.

2.3 Electro-optic sampling

A difficulty in measuring ultrashort pulses is that even the fastest photodiodes, having rise times of a few picoseconds, can not accurately characterize the intensity envelopes of the much shorter sub-picosecond pulses. A common approach when characterizing short pulses is using other, much shorter light pulses as gating pulses to scan the intensity envelope of the pulse of interest. Electro-optic sampling is one such scheme exceptionally well-suited for terahertz characterization, in which a pump and probe pulse are incident on an electro-optic crystal. The electric field of the pump terahertz pulse induces a birefringence that can be probed by a short gating pulse [28]. In order to understand the process, some knowledge of how light propagates through anisotropic media, as well as what the linear electro-optic effect is is necessary. The basic concepts of these areas are presented in the first two sections, before electro-optic sampling is explained in more detail.

2.3.1 Modelling anisotropic media

Media can be macroscopically categorized as isotropic or anisotropic, where the average polarization density induced by an electromagnetic wave is either independent or dependent on the direction of its electric flux density vector. An isotropic material has an electric permitivitty, and thus refractive index, that does not depend on the relative orientation of an incident $\vec{D}$-field. When an electromagnetic wave propagates through an isotropic material with refractive index n, it undergoes a phase shift:

$$\varphi = \frac{2\pi}{\lambda}nd \tag{20}$$

independent of its direction of propagation, where d is the distance traveled through the material. In an anisotropic material, the average induced polarization density depends on the direction of the $\vec{D}$-field, so that it is related to the electric field vector through a tensor relation, which can be represented geometrically as an ellipsoid. In a diagonal system, all off-axis tensor elements vanish, and the geometrical representation is

called the index ellipsoid. This system is called the principal coordinate system and has three refractive indices along each axis, called principal refractive indices. The principle refractive indices are half-axes in the index ellipsoid. The index ellipsoid of an optically isotropic material is a sphere, i.e. an ellipsoid with equal half-axes [20].

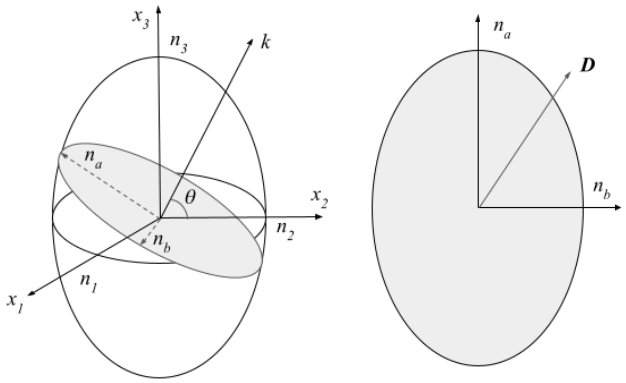

(a) (b)

Figure 8: Index ellipsoid (a), a geometrical representation of the impermeability tensor, and the ellipse traced out by the plane in which the electric-field vector lie (b).

In the principle coordinate system, an anisotropic material is modeled by a three-dimensional cartesian system, with three distinct refractive indices. The principle axis system, together with the index ellipsoid is drawn in figure 8a. Consider a case in which an electromagnetic wave propagates along the direction k in an anisotropic material. The electric flux density vector will lie in a plane perpendicular to the direction of propagation. The plane cuts an ellipse out of the index ellipsoid, for which the half-axes n_a and n_b can be determined from the index ellipsoid and the angle that the plane cuts the ellipse at [20]. The ellipse cut out by the plane of the electric flux density vector is shown in figure 8b.

The figure illustrates a case which will be of importance for understanding the principle of electro-optic sampling: when the electric-field vector is linearly polarized and oriented so that it is not parallel with any of the half-axes of the ellipse. The phase-shift of such an electro-magnetic wave can be determined by projecting the flux density vector onto each axis, to two electric-flux components D_a and D_b. Each electric-field component is then linearly polarized so that it sees one distinct refractive index, and will undergo a phase-shift given by equation 20. The total phase-shift of the electro-magnetic wave after propagating a distance d, is described by the difference between the phase-shifts experienced by the two electric-field components, according to [20]:

$$\varphi = \frac{2\pi}{\lambda}(n_a - n_b)d \tag{21}$$

Since the polarization of an electromagnetic wave is determined by the relative phase and amplitudes between its electric-field components, an anisotropic material can be used to change the polarization of light. This phenomenon constitutes the foundation for electro-optic sampling.

2.3.2 The electro-optic effect

An externally applied steady-state electric field can change the refractive index of a material. Since this change is in general small, the refractive index as a function of the applied electric field can be expanded in a Taylor series [20]:

$$n(E) \approx n + a_1 E + \frac{1}{2} a_2 E^2 + ... = n - \frac{1}{2} r n^3 E - \frac{1}{2} s n^3 E^2 + ... \tag{22}$$

where the first-order term is called the *Pockels effect*, and is the one used in electro-optic sampling. It is also called the linear electro-optic effect, since it is linearly dependent on the applied electric field. Media exhibiting the linear electro-optic effect are called Pockels cells and r is called the *Pockels coefficient*.

As discussed in the previous section, media sometimes have more than one refractive index, which will cause different changes to the refractive indices depending on the direction of the applied static field. The optical properties of a material are described by the index ellipsoid, and their alteration under an external DC electric field can thus be represented as a modification of the index ellipsoid by rotating and/or deforming it by re-scaling the principal refractive indices. Alterations of these properties can, for instance, cause a uniaxial crystal to behave biaxially under the influence of an electric field; or, as is the case of interest in this thesis, it can induce a biaxial behavior in an originally isotropic crystal. This case is illustrated in figure 9. How the index ellipsoid is modified depends on the direction along which the electric field is applied relative the crystal structure. The deformation of the index ellipsoid as a result of the Pockel's effect can be described mathematically by [20]:

$$\eta_{ij}(\vec{E}) = \eta_{ij}(0) + \sum_k r_{ijk} E_k \tag{23}$$

where r_{ijk} are elements in the *Pockels tensor*, $\vec{r}$, which changes for different crystal groups [20]. The electro-optic crystals used in the project, Zink Telluride (ZnTe) and gallium phosphide (GaP), are isotropic crystals that belong to the cubic $43\bar{m}$ crystal group, for which the Pockel's tensor has only one independent entry, r_{41}.

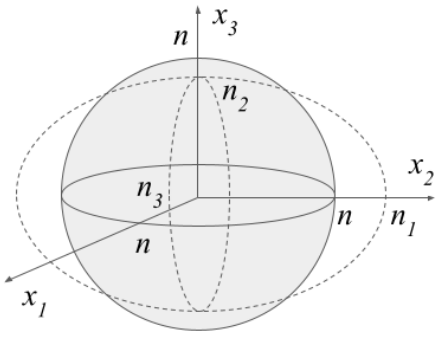

Figure 9: The gray sphere represents an isotropic material, and the dashed ellipsoid is the modification of the sphere when an external electric field is applied, inducing a biaxial behaviour of the index ellipsoid by rescaling the principal axes.

2.3.3 Electro-optic sampling

Electro-optic sampling utilizes how the Pockels effect changes the optical properties of a material. When a terahertz field is incident on a Pockels cell it rotates and deforms the index ellipsoid of the material, which impacts the relative phase between electric field components of the probe pulse. Since the first-order Pockels effect is used, the change is directly proportional to the electric field of the terahertz pulse. This way, the induced phase-retardation of the probe beam can be used in order to map the intensity envelope of the terahertz pulse by temporally overlapping the probe pulse with different points along the pump pulse [28].

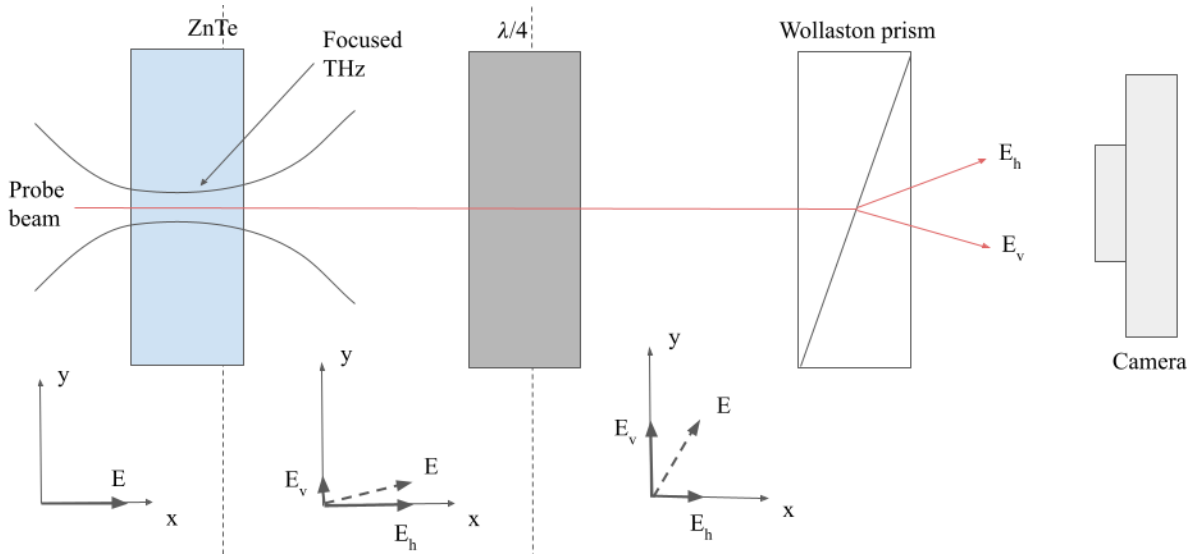

Figure 10: Principle of electro-optic sampling using a quarter-wave plate. Terahertz radiation is focused onto an electro-optic crystal where it induces an elliptical polarization in an originally linearly polarized probe pulse by distorting the index ellipsoid of the crystal. The signal is enhanced by a quarter-wave plate and the polarization components are separated using a polarizing beam-splitter.

GaP and ZnTe are common crystals used for electro-optic sampling. The largest polarization rotation is obtained when the cubic crystals are cut in the 110-plane. The change in polarization can be measured by blocking one of the components with a polarizer and looking at the intensity that comes through from when the crystal rotates the light. Another way is a balanced detection scheme in which a quarter-wave plate is rotated 45° with respect to the optic axis of the crystal, making the pump pulse circularly polarized. By measuring the difference in spot intensity, the terahertz electric field can be characterized, since one of the spots will gain a higher intensity and the other a lower when the crystal rotates the polarization [28]. The balanced detectin scheme is shown in figure 10.

2.3.4 Crystal orientation for electro-optic crystals cut in the 110-plane

When considering how the electro-optic crystal axes should be oriented relative the electric fields of pump and probe pulse, it is necessary to keep track of a two different coordinate systems: the crystal axes of the Pockels cell and the axes of the index ellipsoid

describing the optical properties of the crystal. Both ZnTe and GaP have cubic symmetry and belongs to the $43\bar{m}$ group, for which the crystallographic axes are conveniently defined by a cartesian coordinate system with axes 100, 010 and 001, shown in figures 11ab. When cut along the 110-direction, a beam at perpendicular incidence to the crystal surface propagates parallel to the 110-vector, so that the 001 crystal axis lies in the crystal plane. The interested reader is referred to [28] for derivations and more extensive discussions on electro-optic sampling. This thesis limits its scope to mainly presenting the results and their impact on electro-optic sampling considerations. Introduce a coordinate system XY in the crystal plane, where Y = [0 0 1] and X = [-1 1 0] and consider a beam propagating parallel to the 110-axis. The electric field of the electro-magnetic wave will lie in the crystal plane, and is defined relative the X-axis (-110 crystal axis) through an angle α, shown in figure 11c.

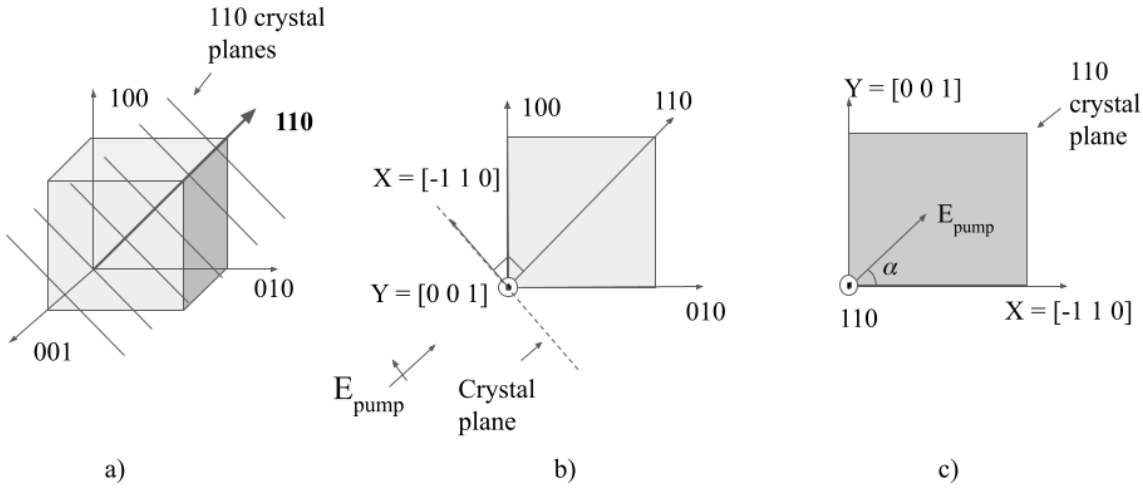

Figure 11: Geometry of ZnTe and GaP. The crystallographic axes can be defined by a conventional cartesian symmetry as shown in (a) and (b). A crystal cut in the 110-plane and light passing parallel to this has the crystal axis 001 and electric field in the crystal plane. The distortion of the index elliposid depends on the relative orientation of the electric field to the 001-axis. This direction is defined by the angle α that the electric field vector makes with the -110-axis. This is shown in figure (c).

Since the crystals are isotropic, their index ellipsoid is originally a sphere. Upon application of an external electric field, the sphere is rotated and the axes re-scaled, so that the optical properties are instead described by an ellipsoid. In what way the ellipse is distorted depends on the direction in which the electric field is applied relative the crystal axes, i.e. what the angle α is. This means that the orientation of the electric field vectors of pump and probe pulses relative the crystallographic axes are very important in electro-optic sampling. The new principal system vectors can be expressed in the XY-coordinate system as [28]:

$$U_1 \propto \begin{pmatrix} -1 \\ 1 \\ \frac{2\sqrt{2}cos(\alpha)}{\sqrt{1+3cos^2(\alpha)+sin(\alpha)}} \end{pmatrix}, U_2 \propto \begin{pmatrix} 1 \\ -1 \\ \frac{2\sqrt{2}cos(\alpha)}{\sqrt{1+3cos^2(\alpha)+sin(\alpha)}} \end{pmatrix} \text{ and } U_3 \propto \begin{pmatrix} -1 \\ -1 \\ 0 \end{pmatrix} \tag{24}$$

From this we see that U_3 is parallel to the 110-axis, which must mean that U_1 and U_2 lie in the 110-crystal plane. This is shown in figure 12. Depending on the angle α that the electric field vector of the pump beam makes with the X-axis, the principal axes U_1 and U_2 are rotated so that U_1 makes an angle Ψ with the X-axis. The phase retardation experienced by the probe beam while propagating along U_3 (i.e. parallel to the pump beam) depends on the refractive indices n_1 and n_2 and their relative orientation to the electric field vector of the probe beam. The orientation of the principal refractive indices in turn depends on the orientation of the electric field vector of the pump beam relative to the X-axis of the 110-plane. The corresponding principal refractive indices (assuming $r_{41}E_{THz} << \frac{1}{n_o^2}$) can be derived to [28]:

$$\begin{aligned} n_1 &= n_0 + \frac{n_0^3 r_{41} E_{THz}}{4}\left(sin(\alpha) + \sqrt{1+3cos^2(\alpha)}\right) \\ n_2 &= n_0 + \frac{n_0^3 r_{41} E_{THz}}{4}\left(sin(\alpha) + \sqrt{1-3cos^2(\alpha)}\right) \\ n_3 &= n_0 - \frac{n_0^3 r_{41} E_{THz}}{4}\left(sin(\alpha)\right) \end{aligned} \tag{25}$$

An expression for the phase retardation can be derived using expressions for n_1 and n_2 in equation 25, together with equation 21:

$$\Gamma(\alpha) = \frac{2\pi}{\lambda_0} d(n_1 - n_2) = \frac{\pi d n_0^3 E_{THz}}{\lambda}\left(\sqrt{1+3cos^2(\alpha)}\right) \tag{26}$$

The phase retardation is thus dependent on the orientation of the electric field vectors of pump and probe field relative the crystallographic axes, and scales linearly with the magnitude of the pump electric field. Since $-1 \leq cos(\alpha) \leq 1$, maximum phase retardation is achieved for $\alpha = 0$, i.e. when the electric field of the terahertz pulse is parallel to the X-axis. The maximum phase retardation can thus be expressed as:

$$\Gamma_{max} = \frac{n_0^3 r_{41} \pi d}{\lambda} E_{THz} \tag{27}$$

The angle Ψ is related to α through [28]:

$$cos(2\Psi) = \frac{sin(\alpha)}{\sqrt{1+3cos^2(\alpha)}} \tag{28}$$

from which it is clear that when $\alpha = 0$, U_1 makes an angle 45° with the X-axis. In order for the probe pulse to see a maximum phase retardation, it should be oriented so that it has an equal projection on both U_1 and U_2, i.e. it should be parallel to the 001-axis. This situation is illustrated in figure 12b.

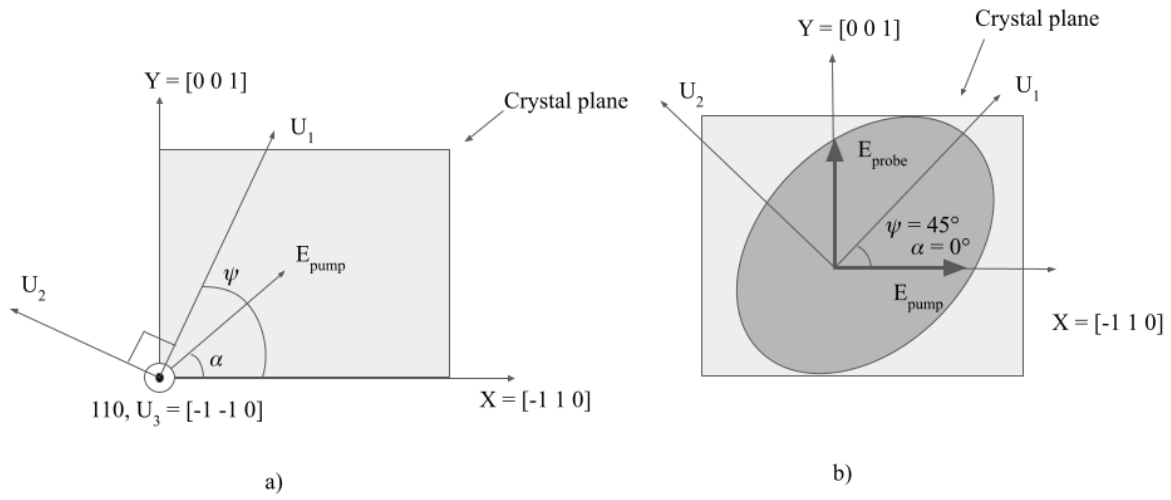

Figure 12: The relative orientation of the principle and crystallographic axes (a) are described by the angle, Ψ, that one of the axes makes with the -110-axis. (b) shows the relative orientation of crystallographic axes, principle axes and electric field of the pump and probe beam are shown. When the electric field vector of the pump beam is perpendicular to the 001-axis and the probe beam parallel to it, the phase of the probe beam undergoes a maximum retardation.

2.3.5 Balanced electro-optic detection

A final note on electro-optic sampling is what scheme to use in order to translate the phase-shift of the probe pulse to an electric field. In the project the balanced detection scheme is used, which utilizes a quarter-wave plate at 45° relative the optic axis of the electro-optic crystal, resulting in a circularly polarized probe pulse. The relative phase shift between the electric field components is measured by separating them using a polarizing beamsplitter, in this case a Wollaston prism, and their relative intensities are recorded with a camera. Assuming that terahertz and probe beams are oriented for maximum phase retardation, corresponding to the geometry in figure 12b, the intensity difference in the balanced terahertz detection scheme is given by [28]:

$$I_{det,h} - I_{det,v} = I_{laser}\sin(\Gamma_{max}) \tag{29}$$

where I_h and I_v are the intensities of the horizontally and vertically polarized electric fields, respectively. Combining equations 27 and 29 the electric field amplitude of the terahertz pulse can be expressed as a function of the normalized recorded intensity difference of the two spots as:

$$E_{THz} = \frac{\Gamma_{max}\lambda_{laser}}{n_0^3 r_{41}\pi d} = \frac{\lambda_{laser}}{n_0^3 r_{41}\pi d}\arcsin\left(\frac{I_{det,h} - I_{det,v}}{I_{laser}}\right) \tag{30}$$

The balanced detection scheme gives a stronger signal response than the crossed-polarizer scheme. The balanced detection signal is linearly dependent on the electric field of the terahertz pulse, as can be seen from equation 30, while the crossed-polarizer setup can instead be shown [28] to depend on the square of the terahertz electric field. Using a quarter-wave plate also means that the effect of inherent anisotropy in the electro-

optic crystal (e.g. arising from mechanical stress or impurities), as well as imperfect polarization of the probe pulse can be reduced with the waveplate [28].

2.4 Pulses co-propagating in media

One last important issue left to address is phase matching, which has an impact on both terahertz generation and electro-optic sampling. When two electromagnetic waves, oscillating at different frequencies, propagate through the same material, they do so at different speeds due to the frequency dependence of the refractive index; a phenomenon known as dispersion. Since both terahertz generation and electro-optic sampling are cases of pulses with significantly differing frequencies, phase-matching of the two needs to be taken into consideration in order to generate strong output signals. A concept which is important in phase matching is group and phase velocity, which is discussed subsequently and following this, phase matching conditions for optical rectification and electro-optic sampling.

2.4.1 Phase and group velocity

As described in section 1.1, a pulsed electric field can be described by a slowly varying envelope, enclosing the rapidly oscillating carrier frequency. The wavepacket propagates with a velocity called the group velocity. Since the pulse is enclosed by its envelope, the group velocity can be seen as the velocity with which a point on the envelope propagates. The carrier wave also propagates with a certain velocity within the envelope. The forwards projection of the carrier-frequency velocity is called the phase-velocity. This can be seen as the velocity with which ha certain point on the carrier-frequency moves forwards [20]. The two velocities are illustrated in figure 13a.

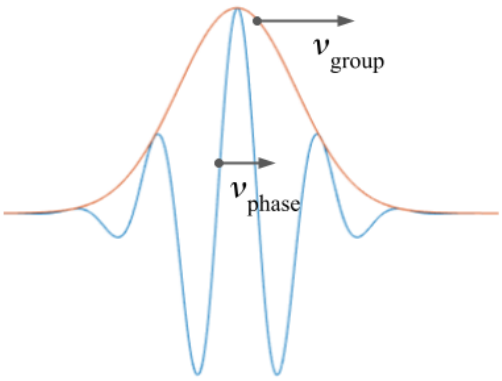

Figure 13: Conceptual illustration of phase and group velocity.

2.4.2 Phase matching for optical rectification

In frequency mixing processes, the generated fields at each point needs to interfere constructively at the crystal exit in order to generate a strong signal. This happens when the seed pulse and the generated pulse are phase matched, where the phase matching

condition can be formulated as a relation conserving the momentum of the three photons involved in the frequency mixing process. In order for momentum to be conserved, the wave vectors must match so that: $\vec{k}(\omega_1) - \vec{k}(\omega_2) = \vec{k}(\omega_3)$. For a pulsed field, all frequencies can not be simultaneously phase matched with the sum- and difference frequencies that they generate, which will result in an inevitable phase mismatch.

In order to derive phase matching conditions for optical rectification, consider two frequencies, ω_1 and ω_2 in a broadband laser pulse which mix to produce a difference frequency Ω_{THz}. The frequencies can be expressed as $\omega_1 = \omega$ and $\omega_2 = \omega + \Omega_{THz}$, and the phase-matching condition as [20]:

$$\vec{k}(\omega + \Omega_{THz}) - \vec{k}(\omega) = \vec{k}(\Omega_{THz}) \Longleftrightarrow \Omega_{THz} \left(\frac{\vec{k}(\omega + \Omega_{THz}) - \vec{k}(\omega)}{\Omega_{THz}} \right) = \vec{k}(\Omega_{THz}) \quad (31)$$

The left-hand side resembles the expression for the derivative of a function $\vec{k}(\omega)$ at a point Ω_{THz}, for small Ω_{THz}:

$$\lim_{\Omega_{THz} \to 0} \frac{\vec{k}(\omega + \Omega_{THz}) - \vec{k}(\omega)}{\Omega_{THz}} = \frac{d\vec{k}}{d\omega} \quad (32)$$

Since $\Omega_{THz} << \omega$ for the case of optical rectification, this approximation is valid, and together with the definition of the group velocity $v_g = \left(\frac{dk}{d\omega}\right)^{-1}$ and $k = \frac{\Omega_{THz}}{v_{phase}}$, where v_{phase} is the phase velocity of the terahertz pulse, this results in a phase matching condition for optical rectification [20]:

$$\frac{\Omega_{THz}}{v_g} = \frac{\Omega_{THz}}{v_{phase}} \Longleftrightarrow v_g = v_{phase} \Longleftrightarrow N_g = n \quad (33)$$

where N_g and n are the group refractive index and refractive index of the pump pulse and the generated terahertz pulse, respectively. From this, we see that the phase matching condition for optical rectification is that the generated terahertz electric field needs to propagate with a phase velocity matching the group velocity of the seed pulse, which is equivalent to the group refractive index of the seed pulse matching the refractive index of the terahertz pulse [20].

A concept which is often used to estimate the interaction range over which a frequency-mixing is efficient is the coherence length, L_c, which is related to the wavevector mismatch of the frequencies involved in the mixing process through $L_c = \pi/|\Delta k|$ [20]. A certain mismatch is tolerated, as long as the interaction region is adjusted accordingly. The coherence length is largely dependent on the wavelength of the generated electromagnetic wave, and since terahertz wavelengths exceed optical by two orders of magnitude, this results in a very long coherence length for the optical rectification process. However, when describing terahertz generation through optical rectification, the coherence length is not the best parameters, due to the relatively high absorption of terahertz in most materials. Instead, a related concept called the *efficient* generation lengths, L_e, can be introduced, that accounts for both phase-matching and absorption effects during propagation through the generation crystal. The effective generation length is derived by Schneider et. al. in [31], where it is introduced as a scaling factor of the electric field spectrum of the terahertz pulse [21]:

$$|E(\omega)| = \frac{\mu_0 \chi^{(2)} \omega I_0(\omega)}{n[n(\omega) + N_g]} L_e(\omega, z) \tag{34}$$

where

$$L_e(\omega, z) = \left(\frac{1 + \exp[-\alpha(\omega)z] + exp[-2\alpha_0 z] - 2\exp\left[-\left(\frac{\alpha(\omega)}{2} + \alpha_0\right) z\right] cos\left(\frac{\omega}{c}[n(\omega) - N_g]z\right)}{\left[\frac{\alpha(\omega)}{2} - \alpha_0\right]^2 + \left(\frac{\omega}{c}\right)^2 [n(\omega) - N_g]^2} \right)^{1/2} \tag{35}$$

$\alpha(\omega)$ is the absorption for the terahertz wavelength ω, α_0 is the absorption for the pump wavelength, z is the length of the crystal and $n(\omega)$ and N_g are the refractive and group refractive indices of the terahertz and pump pulse, respectively.

2.4.3 Phase matching in electro-optic sampling

Electro-optic sampling is another process ultimately limited by dispersive effects between pump and probe beam. The interaction between the two pulses is equivalent to a three-wave mixing process between three photons with angular frequencies ω_1, ω_2 and Ω_{THz} [29]. The phase-matching condition for the process can be derived from the momentum conservation between the photons involved in the mixing process, similarly to the case for optical rectification. For $\omega_2 = \omega_1 + \Omega_{THz}$, where a terahertz photon and a probe pulse photon are summed, producing a third photon with a different polarization from ω_1. Denoting the probe pulse frequencies by $\omega = \omega_2$ and $\omega_1 = \omega + \Omega_{THz}$, the phase-matching condition arising from the momentum conservation can be written:

$$\vec{k}(\omega + \Omega_{THz}) - \vec{k}(\omega) = \vec{k}(\Omega_{THz}) \Longleftrightarrow \Omega_{THz} \left(\frac{\vec{k}(\omega + \Omega_{THz}) - \vec{k}(\omega)}{\Omega_{THz}} \right) = \vec{k}(\Omega_{THz}) \tag{36}$$

which is in every way analogous to the derivation of optical rectification. Again, the left-hand side equals that of the definition of the derivative, since the terahertz frequency is significantly smaller than the probe pulse frequency, and identical calculations to before results in the same condition for phase-matching for electro-optic sampling as for optical rectification. Thus, a strong output signal from the electro-optic sampling process is obtained when the group velocity of the probe pulse matches the phase velocity of the pump pulse.

Phase mismatch is clearly undesirable both when signal strength and temporal resolution are concerned. The quality of the scan is often a trade-off between signal strength and signal distortion from dispersive effects in the sampling process. Thicker crystals give a stronger signal due to an increased interaction length between pump and probe pulse, but propagation over a longer range also increases the effect of phase-mismatch. Dispersion effects in electro-optic sampling determines what crystals are suitable for sampling certain frequency ranges. Since terahertz radiation has energies matching vibrational modes in media, large phase-mismatch occurs when approaching phonon resonances in the electro-optic crystal so that terahertz frequencies that are sampled need to be far away from phonon resonances in the sampling material [28]. Both ZnTe and GaP have phonon resonances in the lower terahertz range and is discussed in the subsequent section.

3 Theoretical calculations and models

The purpose of this section is giving an intuition for parameters more specific to the experimental setup, which was the main focus of the project. In the first section, a few important chirp filter parameters are plotted, giving an idea of the required grating separation to introduce desired stretching of the pulses, and what magnitudes of the group-delay dispersion and chirp rate this would correspond to. The following section is devoted to the optical properties of the crystals used for terahertz generation (DSTMS) and detection (ZnTe, GaP), which largely impacts what the generated terahertz pulses look like. The final section gives an insight into how modifying chirp rate and relative temporal delay between pulse copies affects the generated terahertz pulses, from the simple no-absorption and perfect phase-matching model, in which the terahertz electric field in the far-field follows directly from the temporal derivative of the pump pulse intensity envelope.

3.1 Transmission grating chirp filter

An original pulse duration of 60 fs is used for the pump pulse in all calculations. This was the assumed output pulse duration from the optical parametric amplifier used in the project. The chirp filter is designed to stretch the pulses to 0.5-3 ps durations. Two transmission gratings with 711.24 grooves/mm and (according to specifications) >95% transmission at 35° incidence for light centered around 1550 nm were used. The groove spacing determines the angular dispersion introduced to a pulse, and determines the spacing between the transmission gratings that is needed in order to obtain a certain chirped pulse duration. The chirped pulse duration is related to the duration of the incident pulse and the chirp rate through equation 11 and plotted as a function of grating spacing in figure 14.

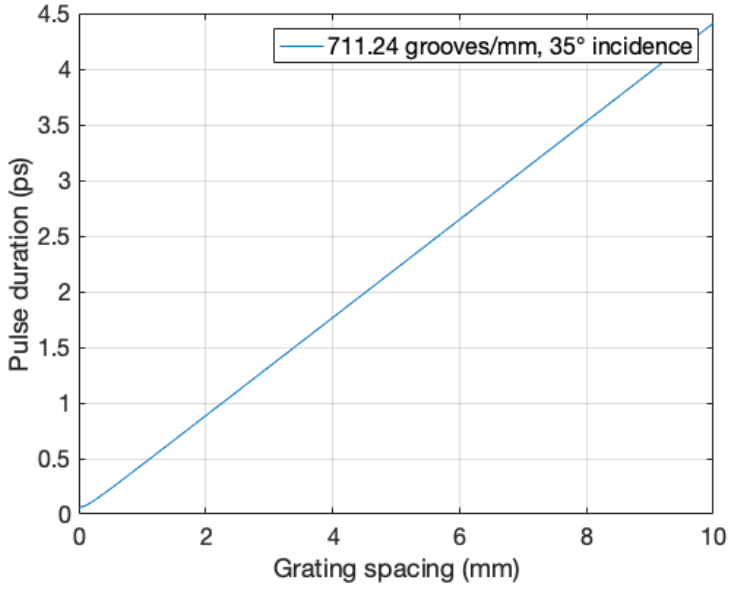

Figure 14: Pulse duration as function of grating spacing for a transmission grating chirp filter with 711.24 grooves/mm and 35° incidence.

The gratings used in the project have a large angular dispersion, and we see that they need to be placed very close to each other, between 1-7 mm in order to stretch an incident pulse of 60 fs duration to a chirped pulse duration between 0.5-3 ps. The gratings in the experimental setup are shown in a close-up image in the "Methods"-section.

The group delay dispersion and chirp rates associated with the relevant grating separations are shown in figures 15a and 15b. From figure 15, we see that for the relevant pulse range in the setup, group delay dispersions on the order of a few thousand fs^2 and chirp rates of tens of THz/ps are relevant.

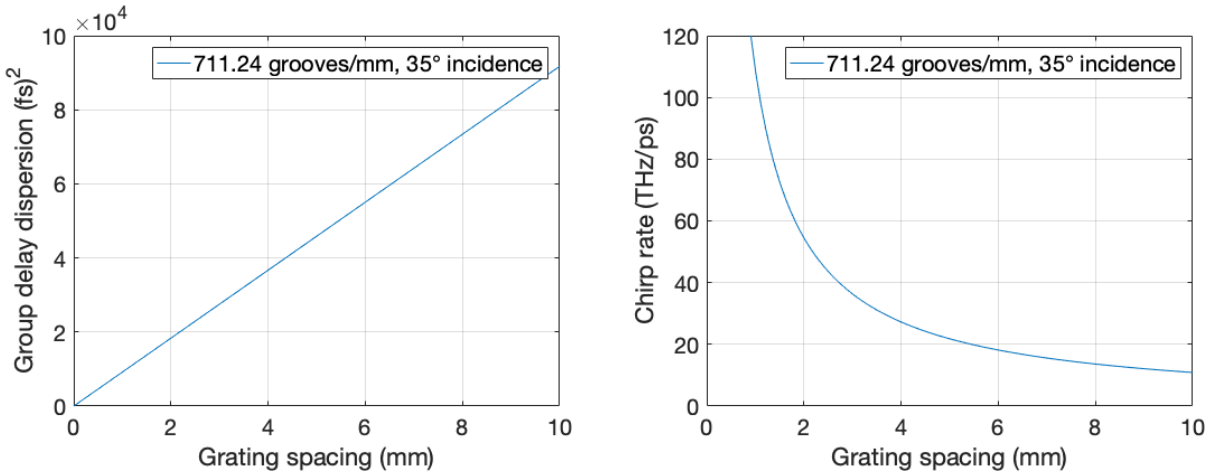

(a) (b)

Figure 15: Group delay dispersion (a) and chirp rate (b) for a transmission grating chirp filter with 711.24 grooves/mm and 35° incidence.

3.2 Terahertz generation with DSTMS

As discussed in the background theory, the efficiency of terahertz generation through optical rectification is dependent on phase-matching between the pump pulse and the generated terahertz pulse. The derived phase-matching condition was that the group velocity of the IR-pulse should match the phase-velocity of the terahertz pulse, which was equivalent to the group index of the pump pulse matching the refractive index of the terahertz pulse. Another limiting factor was the absorption of the different frequencies, which is also frequency dependent. DSTMS is almost transparent to IR wavelengths, but have resonances in the terahertz range. This impacts the phase-matching, where the refractive index is altered close to the absorption peaks, resulting in larger phase-mismatch for certain terahertz frequencies.

Electromagnetic waves in the optical and terahertz regime differ in frequency by two orders of magnitude, resulting in them interacting in very different ways with media, and so their refractive index needs to be modeled differently. In the optical regime, the refractive index is modeled by the Sellmeier equations. The Sellmeier equation for DSTMS is derived by Mutter et. al. in [24], and is used to calculate the group refractive index of the 1500 nm pump pulse. This is plotted as a dashed red line in figure 16a. In the terahertz range, the refractive index is instead modeled as a damped Lorentz oscillator,

summing contributions from resonance peaks that occur in the wavelength range. An equation for the refractive index in the range 0-3.5 THz is derived and experimentally verified by Stillhart et. al. in [21], and is plotted as blue circles in figure 16a. The refractive index up to 11 THz was measured by Montemezzani et. al. [22], but no parameters to reproduce the plot were provided. An estimation of the plotted curve in [22] for 3.5-11 THz is done by manual reconstruction of data points using the free online application provided by PlotDigitizer [23]. The estimated data points are plotted as red circles in figure 16a and an interpolation curve for the data values provided by Stillhart et. al. and Montemezzani et. al. is plotted as a black line.

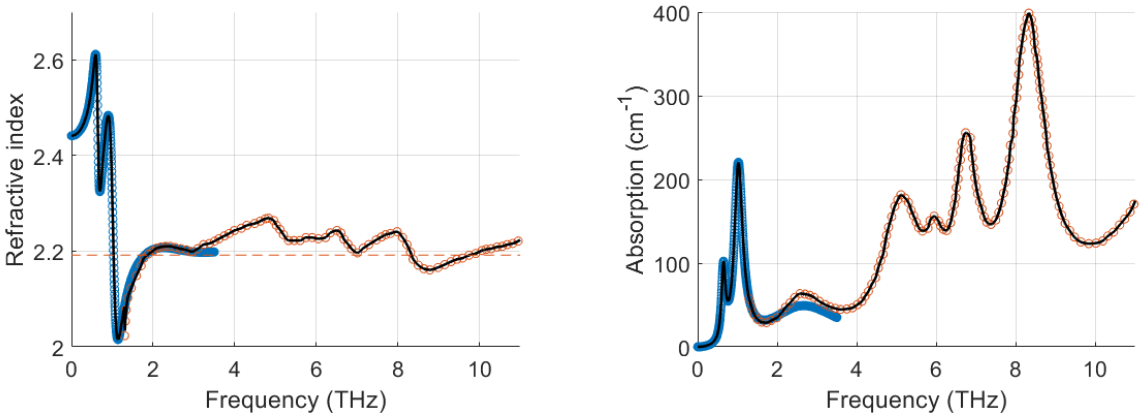

(a) (b)

Figure 16: Refractive index (a, blue curve) and absorption (b) of terahertz frequencies between 0.1-3.5 THz [21] and 3.5-11 THz [22] in DSTMS. The dashed line in (a) is the group index for 1500 nm light. Sellmeier equation and parameters for IR wavelengths in DSTMS are taken from [24].

The absorption as a function of wavelength in the range 600-2200 nm is calculated and plotted by Mutter et. al. [24], but since no data to replicate the plot was provided, the reader is referred to the source for a plot. With the exception of weak absorption bands around 1.15, 1.4 and 1.7μm, the absorption coefficient is below 0.7 cm^{-1} between 1.2 and 1.6 μm, so that the pump pulse absorption is essentially negligible. The absorption in the terahertz range is significantly higher, and is plotted in figure 16b with the equation and parameters given by Stilhart et. al. [21]. The absorption properties for the range 3.5-11 THz estimated by Montemezzani et. al. [22] and is recontructed using PlotDigitizer and interpolation, as explained above. The absorption increases after 4 THz to a level around 150 cm^{-1}, with large fluctuations due to peaks approximated around 5.2 THz (200 cm^{-1}), 6 THz (175 cm^{-1}), 6.75 THz (275 cm^{-1}) and 8.5 THz (400 cm^{-1}).

3.3 Electro-optic sampling with ZnTe and GaP

Both ZnTe and GaP have phonon resonances in the terahertz frequency range, which puts limitations on what frequency ranges can be detected. ZnTe has a phonon resonance around 5.3 THz, which can be seen from figure 17b. The refractive index is increasing for frequencies approaching the phonon resonance, as shown in figure 17a, resulting in larger dispersive effects closer to the resonance. Thus, ZnTe is best suited for sampling

lower terahertz frequencies, between 0.1-4 THz [28], where the phase-matching is good. The group index for 750 nm light in ZnTe is shown by the dashed line in figure 17a, and corresponds relatively well to the refractive index for terahertz frequencies in the range 0.1-4 THz.

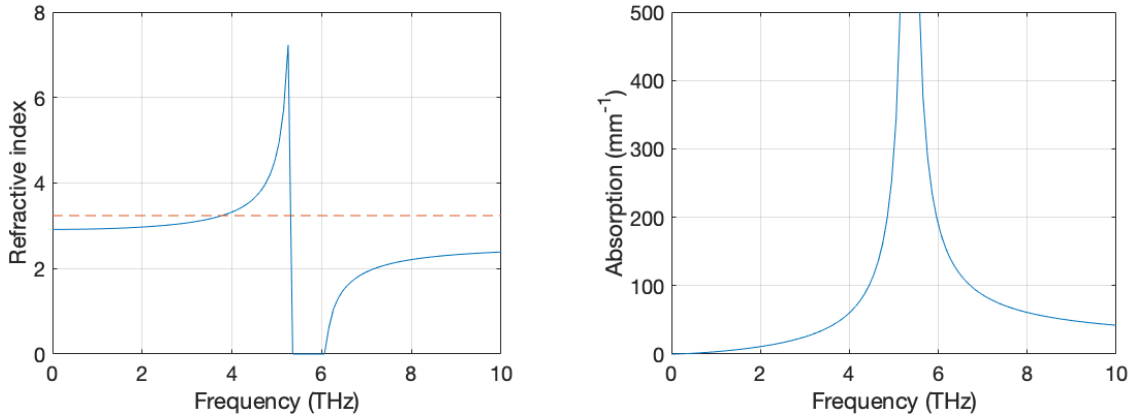

(a) (b)

Figure 17: Refractive index (a, blue curve) and absorption (b) of terahertz frequencies between 0.1-10 THz in ZnTe. The dashed line in (a) is the group index for 750 nm light. Equations and parameters for refractive index and absorption are taken from [28].

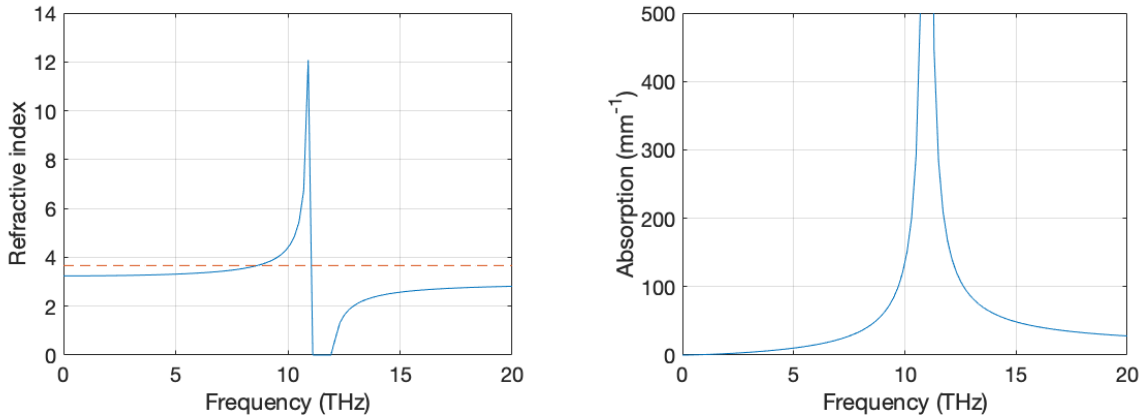

(a) (b)

Figure 18: Refractive index (a, blue curve) and absorption (b) of terahertz frequencies between 0.1-20 THz in GaP. The dashed line in (a) is the group index for 750 nm light. Equations and parameters for refractive index and absorption are taken from [28]

GaP has its first phonon resonance at the significantly higher frequency 11 THz, as seen in figure 18b, and has relatively good phase-matching between 750 nm and terahertz frequencies ranging 0.1-7 THz, making GaP a more suitable choice for sampling frequencies above 4 THz, compared to ZnTe. GaP is well phase-matched for lower frequencies as well, but the electro-optic coefficient for GaP (1 pm/V) is significantly lower than for ZnTe (3.9 pm/V), which results in a weaker detected signal. ZnTe is thus more suitable for the wavelength range 0.1-4 THz and GaP for 4-7 THz [28].

3.4 Narrowband terahertz generation

The terahertz radiation is considered to be in the far-field in the simulations, and so its shape follows from the temporal derivative of the pump pulse intensity envelope if perfect phase-matching is assumed and absorption effects are neglected. To simulate the intensity envelope, two pulses on the form given in equation 16 are overlapped numerically, and the parameters (chirp rate and relative pulse delay) are varied. The code is included in Appendix A.

Initially we consider optical rectification from a single, un-chirped pump pulse. The electric field of the terahertz radiation is given by the derivative of the intensity envelope and is plotted in figure 19b, and the intensity envelope is plotted in figure 19a. The spectral representation of the terahertz electric field is given by the Fourier transform and is plotted in figure 19c.

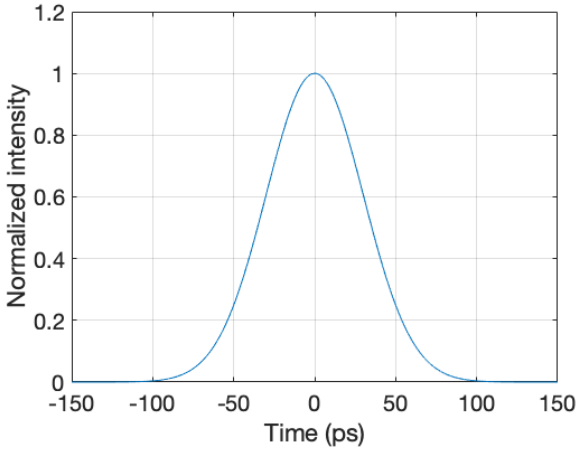

(a)

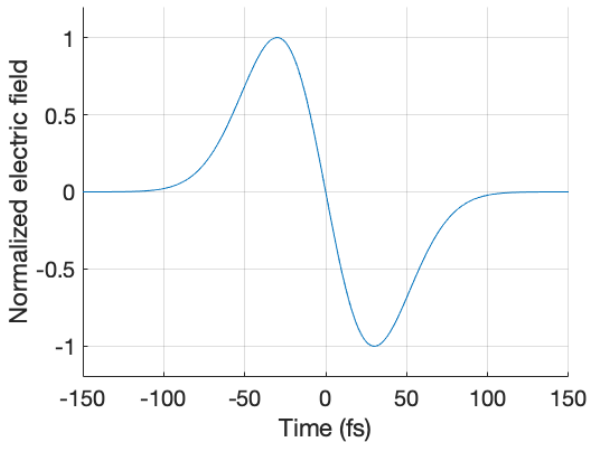

(b)

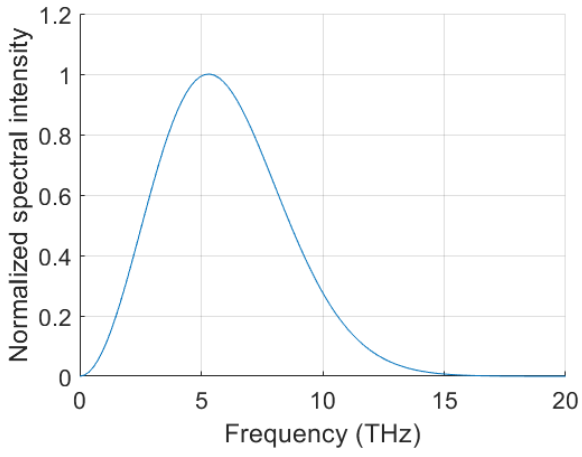

(c)

Figure 19: Terahertz electric field (a) and spectrum (b) from optical rectification of a pump pulse with intensity envelope in figure 19a with no phase-matching or absorption.

Instead, consider the temporal intensity of two beating pulse copies, resulting in a fringe pattern in the temporal envelope. This is plotted for a chirped pulse duration of

1.5 ps and a relative pulse delay of 1.137 ps in figure 20, and results in a beat frequency of 5.8 THz (compare to graph in figure 23) and a bandwidth around 360 GHz (compare to graph in figure 24).

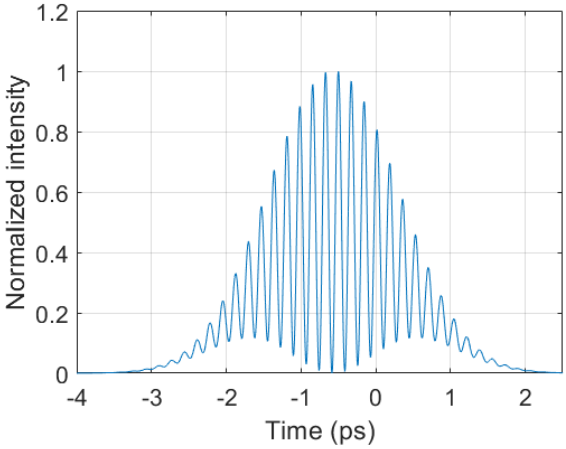

(a)

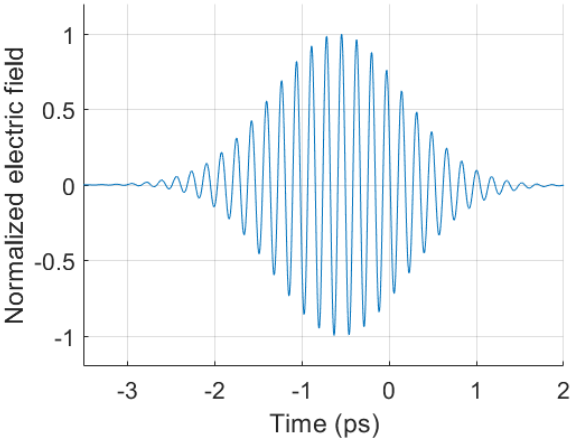

(b)

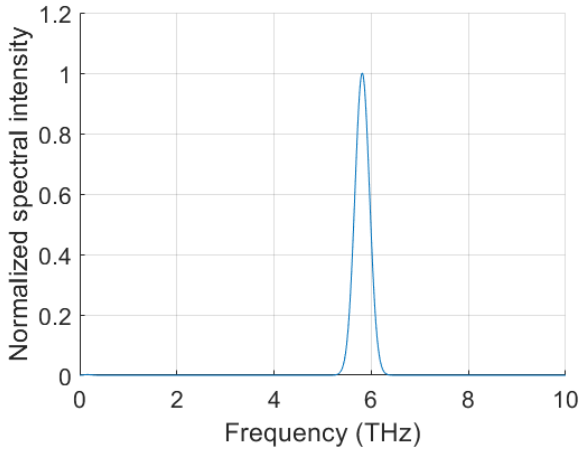

(c)

Figure 20: Temporal intensity (a) of two 1.5 ps long, identically chirped pulses, delayed 1.137 ps relative each other in time. The resulting electric terahertz field in the far-field (b) and the spectral intensity of the electric field (c). For the simple model used in the simulation, these parameters result in a terahertz pulse centered around 5.8 THz with spectral width ≈360 GHz.

Consider two linearly chirped pulses, stretched from 60 fs to 3 ps, overlapped with a relative temporal delay. According to equation 18 the beat frequency increases with increasing delay between the pulse copies. A few terahertz electric fields are plotted together with their respective spectra for pulse delays between 0.5 and 2.5 ps in figure 21. From the figure we see that more cycles are added within the fixed pulse duration as the temporal delay is increased, which corresponds to a higher beat frequency with a constant bandwidth. Thus, for a fixed pulse duration, the pulse is a superposition of a constant amount of frequencies.

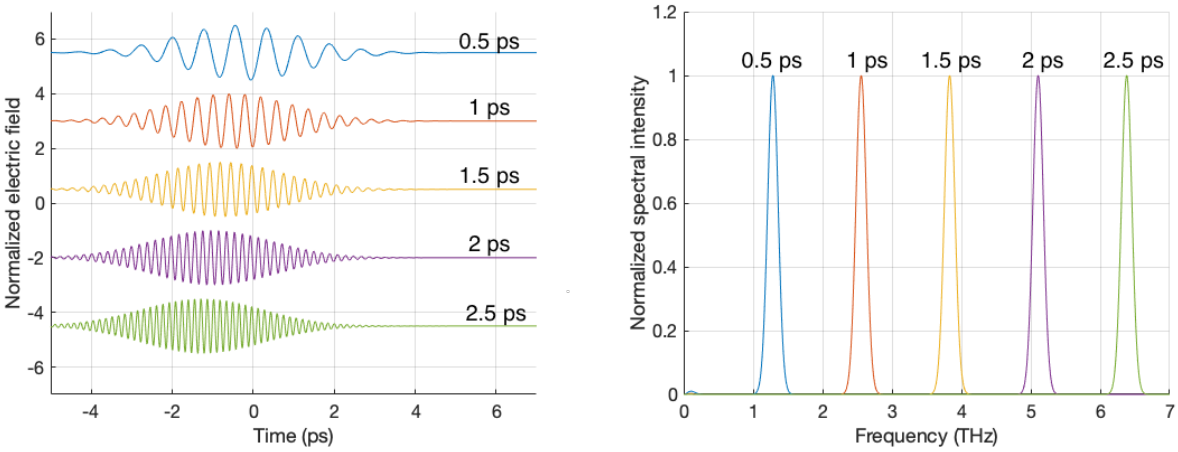

(a) (b)

Figure 21: Terahertz electric field (a) and spectrum (b) from optical rectification a beating pair of pulse copies of chirped pulse duration 3 ps for five different delays between 0.5 and 2.5 ps.

Instead of varying the delay between pulses as above, the chirped-pulse duration is varied between 0.5 and 2.5 ps for a fixed relative pulse delay of 0.4 ps. Electric fields (a) and spectra (b) are plotted in figure 22. From equation 19 we know that the bandwidth of the terahertz pulse decreases with increasing chirped-pulse duration and equation 18 tells us that the beat frequency increases with increasing chirped-pulse duration, so that is must decrease with decreasing chirp rate.

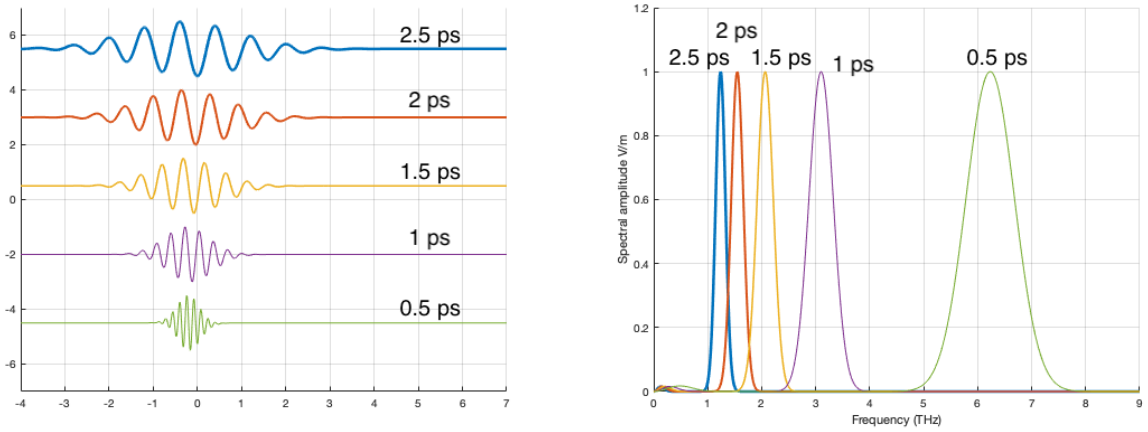

(a) (b)

Figure 22: Terahertz electric field (a) and spectrum (b) from optical rectification a beating pair of pulse copies with a constant relative delay of 0.4 ps for five different chirped pulse durations between 0.5 and 2.5 ps.

The beat frequency as a function of the relative delay between two pulse copies is shown in figure 23a for six different chirped pulse durations: 0.5 ps, 1 ps, 1.5 ps, 2 ps, 2.5

ps and 3 ps. The beat frequency is linearly dependent on the relative time delay, as is clear by equation 18, with a steeper slope for higher chirp rates (longer stretched pulses) and vice versa. The dependence on chirp rate and grating spacing is shown in figure 23b for five different fixed pulse relative delays: 0.5 ps, 1 ps, 1.5 ps, 2 ps and 2.5 ps.

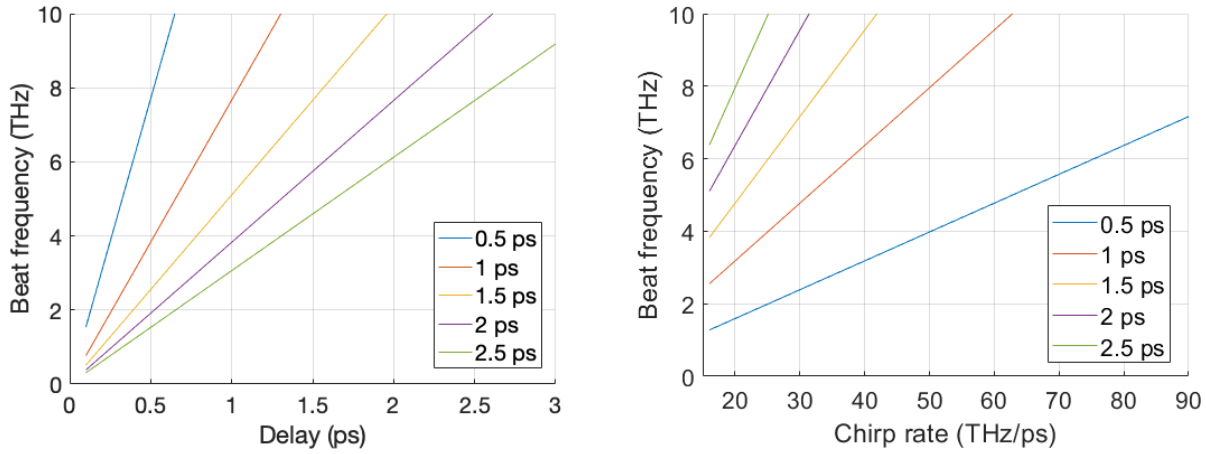

(a) (b)

Figure 23: Beat frequency as function of relative delay (a) and chirp rate (b) for a few different chirped-pulse duration and relative pulse delays.

The dependence on the bandwidth on the chirped pulse duration is given by equation 19 and plotted in figure 24 for a pulse stretched from an original duration of 60 fs.

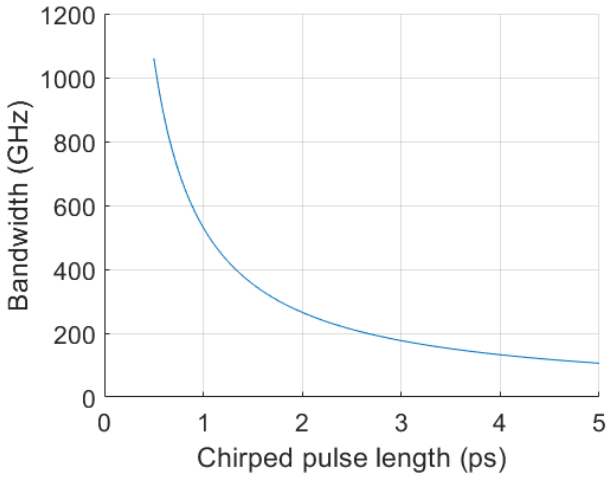

Figure 24: Terahertz electric field (a) and spectrum (b) from optical rectification a beating pair of pulse copies of 3 ps for five different delays between 0.5 and 2.5 ps.

4 Method and experimental setup

Building the setup for the narrowband terahertz generation was the focus of the project, and can be divided into three distinct stages. The first stage was generating terahertz through optical rectification and detecting a signal. Following this, the setup for the electro-optic sampling was built; the main steps being to program a motorized stage, imaging the probe pulse in the electro-optic crystal plane onto the camera chip and finding spatial and temporal overlap of probe and pump pulse. The final stage of generating narrowband terahertz pulses consisted of implementing an angular-dispersion chirp filter and a Michelson interferometer to add chirp-and-delay to the pump pulses of the terahertz generation process, and re-doing spatial and temporal overlap. Due to the electro-optic sampling taking a long time to complete, signal with the narrowband terahertz pulses was not detected with the electro-optic sampling setup within the time frame of the project. However, temporal and spatial overlap was redone for the setup with the divided and recombined pulse copies without stretching the pulses, and a few beat spectra were acquired for the chirped-and-delayed pulses.

4.1 Laser source

The laser source used was an amplified Ti:Sapphire laser producing ≈40 fs long pulses of center frequency 780 nm at a repetition rate of 3 kHz and pulse energy 2.8 mJ. The pulses were up-converted to 1500 nm by an optical parametric amplifier (OPA). The output power from the OPA fluctuated between 1.7 and 2 W for the output signal containing both signal and idler (pulse energies between 567 and 667 μJ) with a beam diameter of approximately 600 μm.

4.2 Filtering the OPA signal and initial terahertz generation

The horizontally polarized idler was separated from the vertically polarized signal using two Thorlabs Brewster's angle polarizers with 95% reflection efficiency for vertically polarized 1550 nm light, and additional green light was filtered out using a high-pass color filter with cut-on frequency at 695 nm. Few-cycle terahertz pulses were generated through optical rectification using an organic DSTMS crystal (Rainbow Photonics) and the residual far-IR pump light was blocked using two 18 THz low-pass filters (Swiss Terahertz).

A flip-mirror was used to guide the THz to the powermeter (Swiss Terahertz), and a TPX lens was used to focus the terahertz onto the sensitive area of the powermeter. The initial beam path from the OPA to the diagnostics station is shown in figure 25, where BP1 and BP2 are the Brewster's-angle polarizers, mirror M1 angles the light onto the DSTMS crystal, LPF1 and LPF2 are the low-pass filter and FM is the flip mirror. The terahertz powermeter used was a pyroelectric detector, translating the intensity into a voltage, which could be converted to a power via a conversion factor 85000 V/W. In order for the powermeter to interpret the terahertz, the signal needed to be modulated, which was done using a chopper operating at a frequency of 10 Hz.

Both the DSTMS crystal and one of the filters were burned when the laser beam was not sufficiently attenuated, shown in figure 26. The burn mark in the filter was covered

with silver paint to keep radiation from getting through the damaged part.

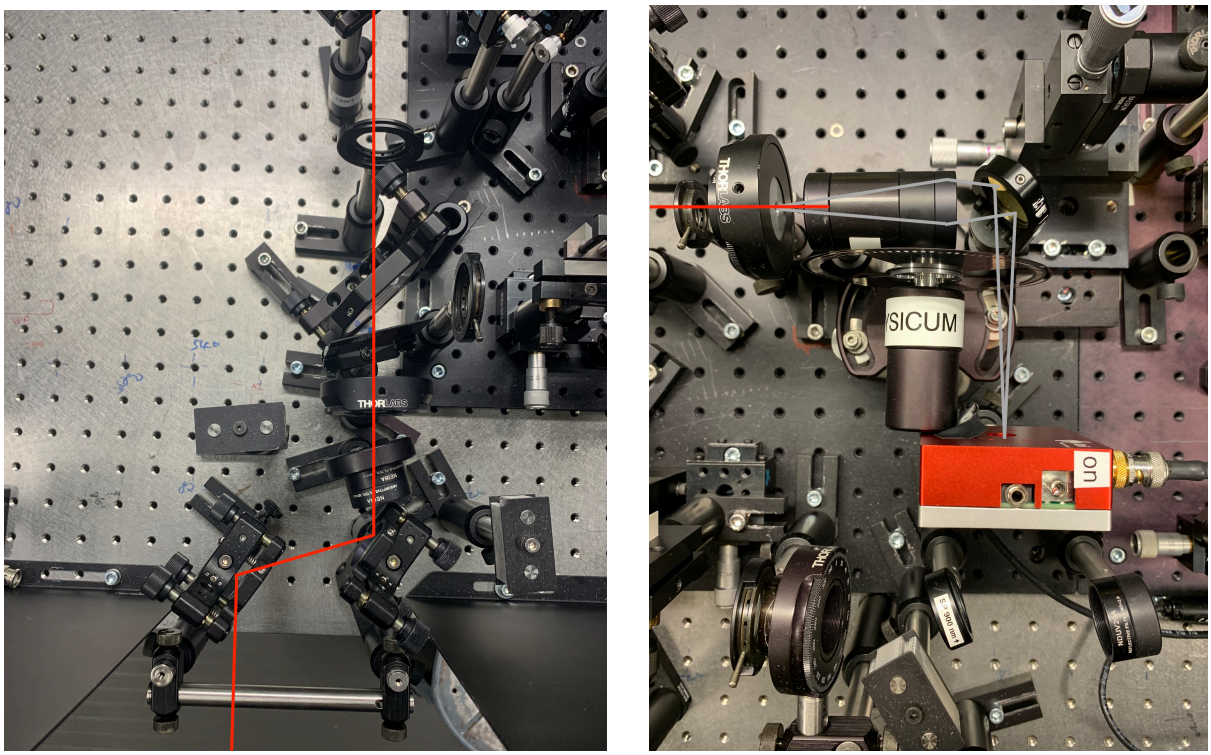

(a) (b)

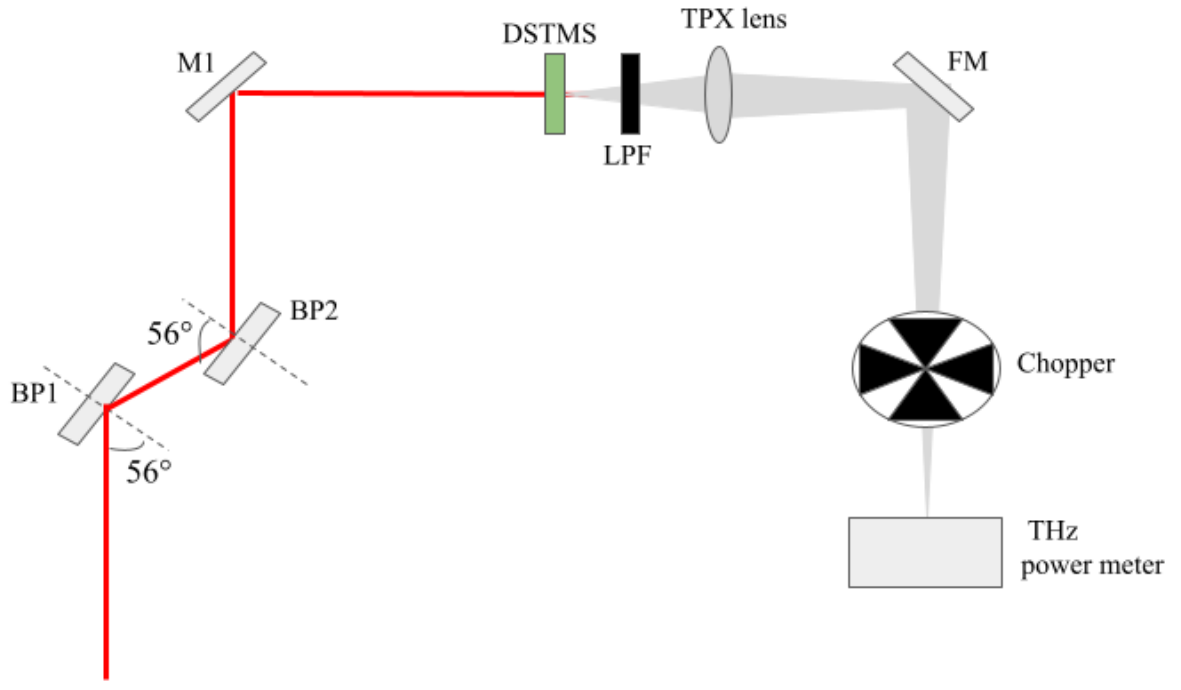

(c)

Figure 25: The initial setup (a,b) and a schematic (c) for terahertz generation with a DSTMS crystal, and detection with a terahertz powermeter.

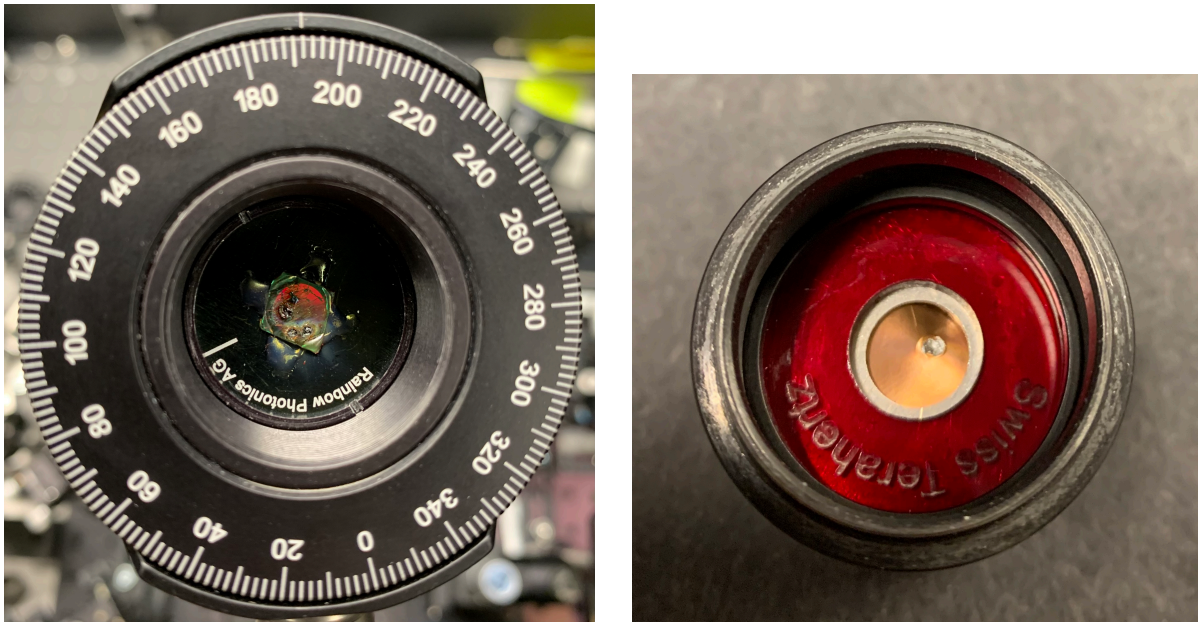

(a) (b)

Figure 26: DSTMS crystal (a) used for terahertz generation and terahertz filter (b) used to filter out the 1500 nm light. There are multiple clearly visible burn marks in the crystal due to exposing the crystal to too high fluence levels. The damage in the filter is covered with silver paint.

4.3 Electro-optic sampling

The main steps of building the electro-optic sampling setup was programming a step motor to move in a sequence with a set step length and transmitting a trigger signal after each move, imaging the crystal plane onto a camera chip and to overlap the pulses in space and time. A schematic of the complete setup for terahertz generation and electro-optic sampling is shown in figure 27.

4.3.1 Step and camera

The translation of the probe pulse was implemented by placing a hollow-roof mirror on a motorized translation stage. The stage was driven by a Thorlabs T-Cube DC motor, which was programmed in LabVIEW for moving the step in a sequence, pausing and sending a digital trigger signal. The code is included in Appendix A. The intensity of the probe beam after passage through the zinc telluride crystal was recorded using a FLIR USB 3 camera, which was controlled by the program BeamProfiler, developed by Dr. Anders Persson at the Atomic Physics institution. Upon receiving an external trigger signal the camera recorded an image.

4.3.2 Generating the probe pulse

The probe pulse was generated by dividing the signal from the OPA into two using a 99%/1% beam sampler for horizontally polarized 1500 nm light. The vertically polarized OPA signal was rotated 90° by a 1500 nm half-wave plate to be properly divided by the

beam sampler. A second-harmonic at 750 nm was generated from the 1%-OPA signal using a 2 mm thick Type-I KDP crystal for vertically polarized 800 nm light and the other 99% was used as pump for terahertz generation. The doubling crystal was rotated in order to fulfill the phase-matching condition for second-harmonic generation for 1500 nm light. The residual OPA signal was filtered from the second-harmonic using a short-pass filter with cutoff wavelength 900 nm.

4.3.3 The setup

The terahertz radiation generated by the organic crystal was focused by a holey parabolic gold mirror with a reflected focal length of 50.8 mm. The attenuated 750 nm-light was reflected by a hollow-roof silver mirror, placed on the Thorlabs motorized stage, and aligned to pass through the holey mirror onto the zinc telluride crystal. The ZnTe crystal was placed at the focal length of the parabolic mirror, and followed by a quarter-wave plate, converting the linearly polarized light to circularly polarized light. The two components of the electric field were separated by a 1° Wollaston prism, sending them at different angles onto the chip of the camera. The optical setup as further developed from the initial terahertz generation is shown in figure 27.

4.3.4 Imaging the crystal plane

Due to the probe beam being much larger than the focused terahertz, good imaging of the crystal plane was necessary in order to see the intensity changes in parts of the probe pulse. A lens of focal length 2.5 cm was used to image the crystal plane. The lens was placed relative the camera chip so that the crystal surface appeared sharp on the camera, when the Wollaston prism and quarter-wave plate were removed. The camera was then moved back to account for the change in optical path length difference when adding the prism and waveplate.

4.3.5 Spatial overlap

The main difficulty in constructing the electro-optic sampling was achieving spatial and temporal overlap of pump and probe pulse. A difficulty in overlapping pulses in the terahertz regime with ones in the optical lies in the two not being simultaneously visible. Additionally, the orientation of the 001-axis of the crystal was not known, increasing the number of unknowns when looking for overlap.

Spatial overlap of the pulses was approximated by first locating the focus of the terahertz beam from the parabolic mirror with a terahertz camera. A wire grid polarizer was placed in front of the parabolic mirror in order to obtain an unsaturated signal, so that the focal plane of the parabolic mirror could be approximated. The terahertz camera was moved out of focus and a 500 μm aperture was used to find the location of the terahertz focus, which was approximated to be around 250 μm. However theoretically possible to place the aperture so that the focused terahertz radiation passed through it, it proved difficult to find the exact location of it in practice, and instead the aperture was used to find an approximate location of the terahertz focus. The probe beam was then moved so that it also passed through the closed aperture.

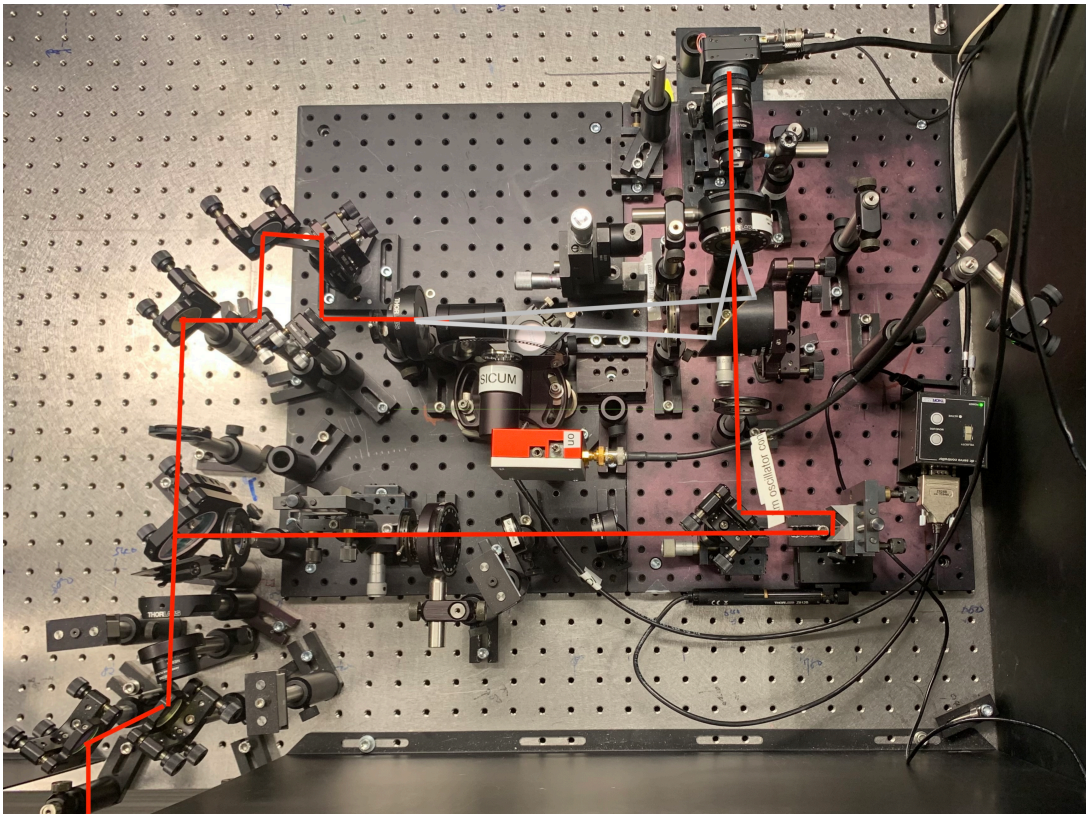

(a)

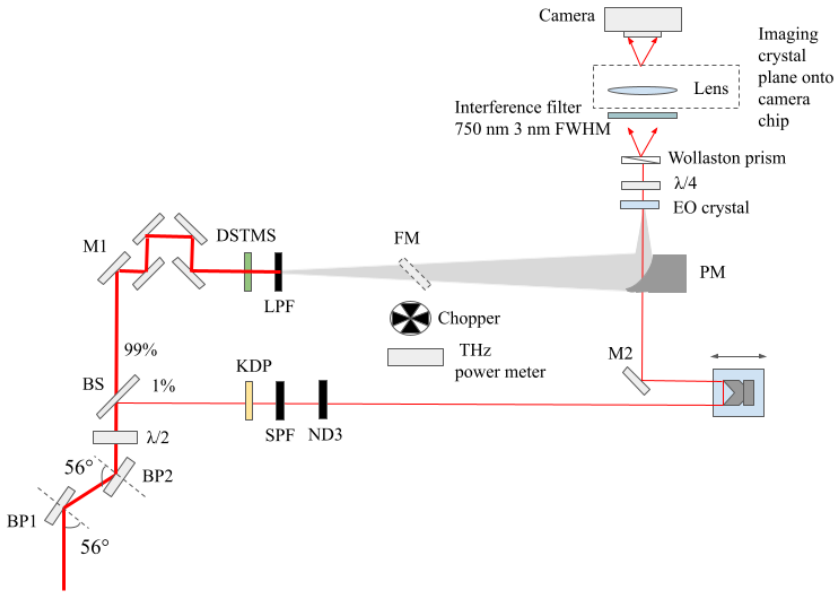

(b)

Figure 27: The setup for electro-optic sampling for terahertz pulses from optical rectification of transform limited pulses.

It was not a trivial problem to place the very thin (1mm, 0.5 mm and 100 μm) crystals in the exact same plane as the aperture opening. It was done by using a USB microscope (Dino-Lite AM7515MT8A) with a small depth of field (between 0.01 and 0.008 mm according to specifications), placing the microscope so that the aperture was in focus. After

this, the aperture was removed and the crystal was moved into focus of the microscope. The short depth-of-field of the microscope provided a good approximate placement of the crystal relative the aperture. This way, the two beams were approximately spatially overlapped in the terahertz focus, and the crystal coincided with the overlap. The setup when focusing on the aperture with the USB microscope is shown in figure 28, with focused images of the aperture and the crystal.

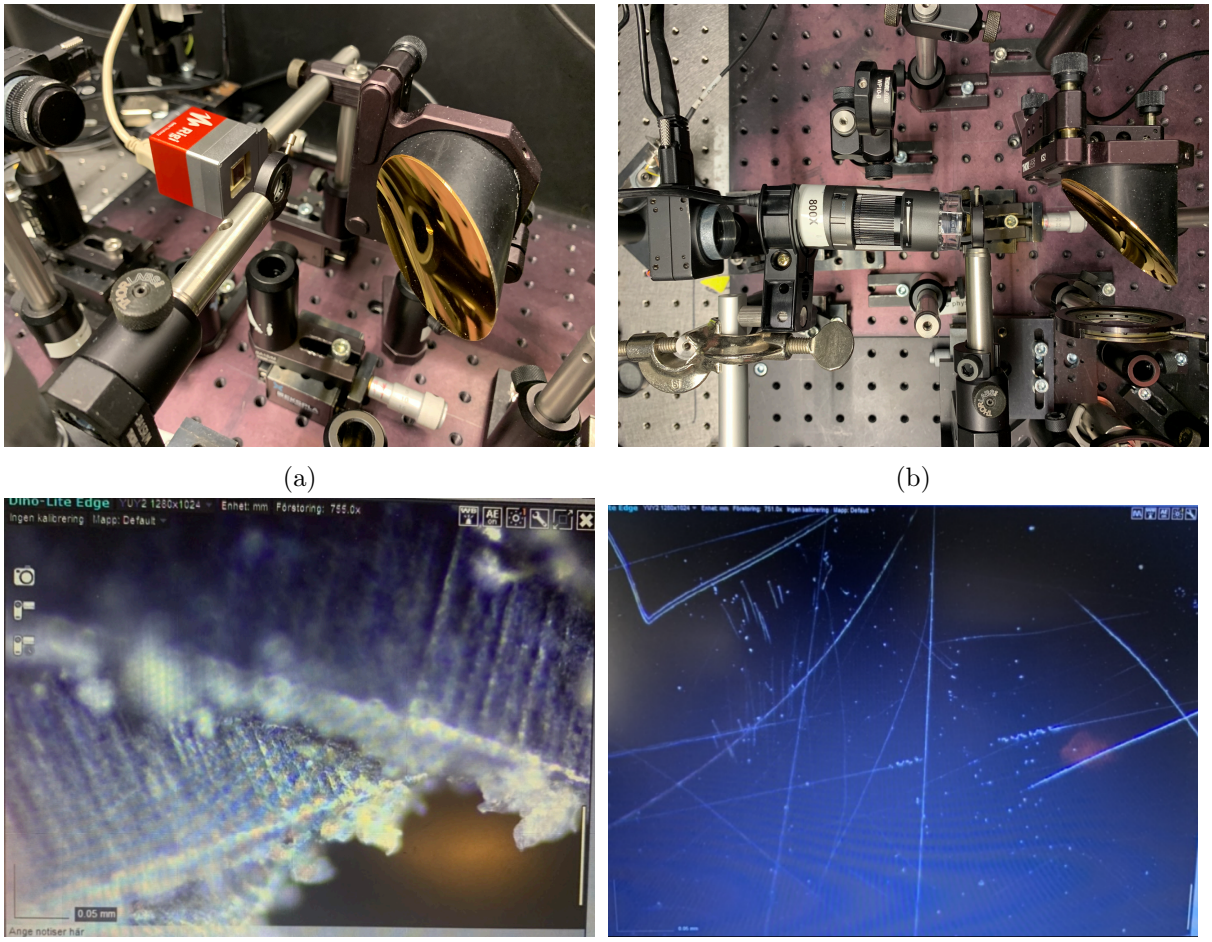

(a) (b)

(c) (d)

Figure 28: Setup and images from USB microscope when placing the electro-optic crystal in the correct plane as determined using the aperture. a) aperture placed in front of terahertz camera to approximate the terahertz focus, b) USB microscope with aperture in focus, c) image of the aperture opening when in focus of the USB microscope. The depth of field is short enough for different parts of the aperture shutter blades to not be simultaneously sharp. The parts of the blade closest to the opening are the ones in focus, d) The crystal surface seen through the USB microscope when placed in focus.

4.3.6 Temporal overlap

Initially temporal overlap was approximated by measuring the path length with a ruler. Temporal overlap within the range of the motorized stage was ensured more carefully using two photodiodes with 30 ps rise time connected to a 5 GHz oscilloscope, in order to get as accurate estimations as possible. The organic crystal was replaced with a doubling

crystal so that the pulses from both arms could be detected by a diode placed after the parabolic mirror as shown in figure 29. The detected pulses were triggered using another identical photodiode, measuring pulses from the Ti:Sapphire laser (see figure 29b), to reduce the jitter in the signal and get a more accurate approximation of the temporal overlap. The step was moved the entire range, and it was verified that the probe pulse moved across the pump pulse when moving the hollow roof mirror from start position to end position.

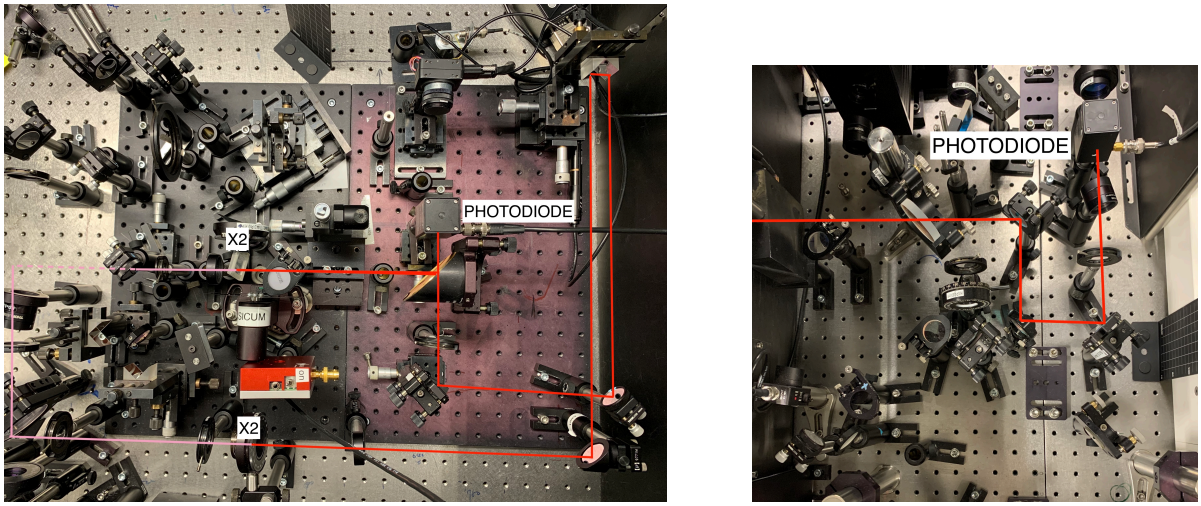

(a) (b)

Figure 29: Temporal overlap with the diodes. (a) shows the photodiode placed in front of the parabolic mirror and the doubling crystals to create light in the detectable range of the photodidoe. (b) shows the photodiode used to trigger on.

Careful alignment of the hollow-roof mirror ensured that the probe spot did not drift during the scan. The scan time over the entire range was very long, and in order to decrease the range that needed to be scanned when looking for overlap, temporal overlap was further narrowed down using two-photon fluorescence of the 780 nm seed pulse to the OPA. Taking part of the seed pulse and sending it into the terahertz generation setup after exchanging the beam sampler to a 50%/50% 800 nm beam splitter, two-photon fluorescence of the 780 nm light was observed on a green paper in the focus of the parabolic mirror. 800 nm light fluoresced on the green paper, and the two beams were strong enough to be seen individually so that they could be spatially overlapped. The nonlinearity of the flurescence process resulted in a significant increase in fluorescence when the two pulses overlapped temporally. The organic crystal and the 1500 nm 99%/1% beam sampler were put back, and the difference in path length traveled by the 1500 nm light was calculated and compensated for. This way the scan range considered when looking for signal could be decreased significantly.

The final overlap between the terahertz and 750 nm probe pulses was found by removing the quarter-wave plate, and manually pushing the translation stage while observing when the intensity in the blacked-out spot changed. The probe beam was moved in small steps around the approximate spatial overlap in the crystal plane, and the crystal was moved in steps of 250 μm (half of the crystal thickness) along the direction of beam propagation. This was all done for different orientations of the electro-optic crystal, since

the orientation of the 001-axis was not known. Due to the electric field of the terahertz being strong in the focus, a visible change in intensity in parts of the blacked-out spot could be seen when the pulses overlapped (see figure 36 in the results).

4.3.7 Electro-optic crystals used

The electro-optic sampling was evaluated for three different crystals: a 1 mm thick ZnTe crystal, a 0.5 mm ZnTe crystal and a 100 μm GaP crystal. Initially the 1 mm thick ZnTe crystal was used to search for overlap since it should according to theory give the strongest response. Due to it being the most damaged, in the end it was exchanged for the 0.5 mm thick ZnTe crystal, for which the temporal overlap was finally found. The three crystals are shown in figure 30.

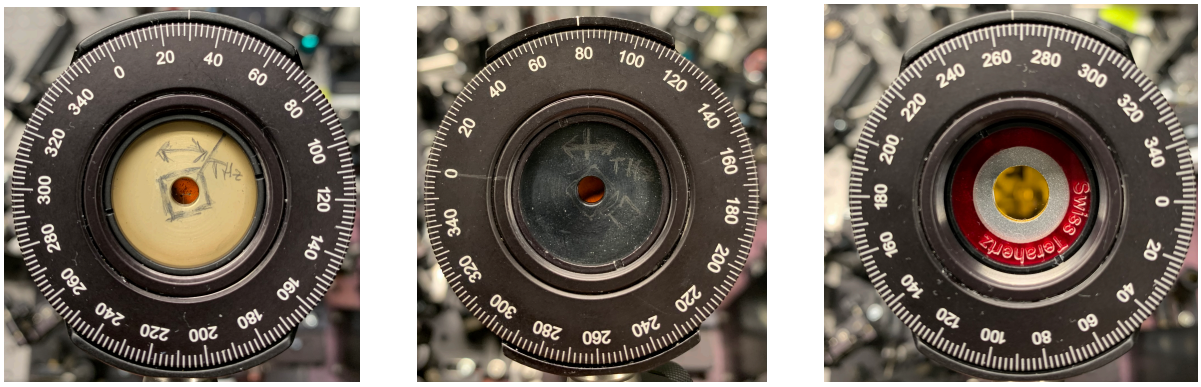

(a) (b) (c)

Figure 30: Electro-optic crystals used for characterizing the generated terahertz pulses. (a) 1 mm thick ZnTe crystal, (b) 0.5 mm thick ZnTe crystal and (c) 100 μm thick GaP crystal. All were cut in the 110-plane. Arrows show the orientation of the terahertz electric field for maximum rotation of the probe beam.

4.4 Towards a setup for narrowband terahertz generation

Due to the crystal and terahertz filters being damaged from the laser beam, the beam was magnified after having a working electro-optic sampling. Chirp-and-delay was added for the 99%-beam after the beam sampler and the path length of the probe beam was increased to match that of the pump beam. The main steps of extending the setup consisted of constructing the Michelson interferometer, so that the pulse copies overlapped in time and space and traveled co-linearly through the organic crystal, to measure the spectrum of the recombined pulses and to do spatial and temporal overlap of pump and probe pulse again. The narrowband setup was not finished, but the steps completed are described in subsequent sections.

4.4.1 The setup

Mirror M1 from the previous setup was moved further away from the beam sampler, sending the beam onto the pulse stretcher. The pulse stretcher was constructed using two 95% transmission gratings (Edmund Optics) for 1500 nm light, G1 and G2 and

a hollow-roof mirror that vertically translated the signal and sent it back through the gratings. G1 angularly disperses the beam, adding temporal and spatial chirp, and the beam is parallellized by G2. The beam is reflected back onto G2 by the hollow-roof mirror, where the spatial chirp is removed, while the temporal chirp is doubled. The chirped pulse is divided into two copies in a Michelson interferometer, and recombined with a variable delay. M3 directs the recombined pulse copies onto the organic crystal used for terahertz generation. The electro-optic sampling setup was not changed, apart from an additional path length added for the probe beam in order for the pulses to overlap in time. The setup is shown in figure 31.

4.4.2 Aligning the interferometer

Upon recombination after the beamsplitter the two pulses must be spatially and temporal overlapped, as well as propagate somewhat co-linearly until having propagated through the crystal. Spatial and temporal overlap as well as co-linear propagation was achieved using a pinhole together with a camera. The pinhole was placed after M6 and the camera before the parabolic mirror. A doubling crystal was placed in front of the camera, and angled for phase-matching for second-harmonic generation of 1500 nm light, so that the beam was visible on the camera. The setup to find the overlap can be seen in figure 32a. Verifying that the beam from both arms passed through the pinhole and were overlapped on the camera when increasing one of the arms lengths, collinearity and spatial overlap was done. Temporal overlap could be found by seeing when the frequency-doubled light was increased. Due to the nonlinearity in the frequency-mixing process, the doubled light increases significantly when the two pulses propagate through the crystal at the same time. The setup together with the difference in signal when the pulses are temporally overlapped and when they are not is shown in figure 32.

4.4.3 Terahertz detection and pulse overlap of the extended setup

Initially, an attempt was made to detect narrowband terahertz pulses with the terahertz powermeter. When this was not possible, the gratings were removed from the setup and the terahertz generation verified with the powermeter when the un-chirped pulses were split and recombined after the interferometer. Spatial and temporal overlap in the electro-optic sampling was done for the setup without gratings.

Spatial overlap was again done using an aperture to give an approximate location of the terahertz focus, sending the probe beam through the same pinhole and placing the crystal in the same plane using the USB microscope. A rough estimation of the temporal overlap was done similarly to before, first measuring with a ruler and then verifying that the overlap was within the range of the stage by detecting the pulses with a photodiode. Previous sections describe these procedures more carefully, and as they are the same for the extended setup, the reader is referred to these for more detailed descriptions.

The more careful temporal overlap was this time done using frequency mixing, similarly to the overlap for the interferometer, instead of two-photon fluroescence like the previous time. Removing the organic crystal from the pump arm and the doubling crystal from the probe arm, a doubling crystal was placed in the focal plane of the parabolic mirror, and a camera with an interference filter around 750 nm was used to record the

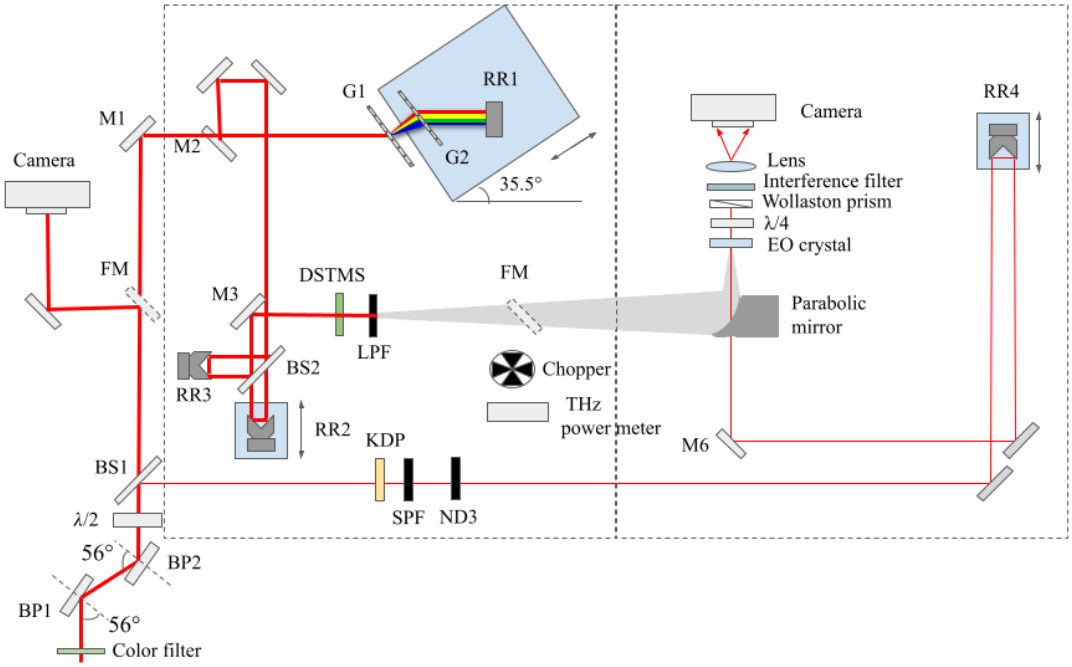

(a)

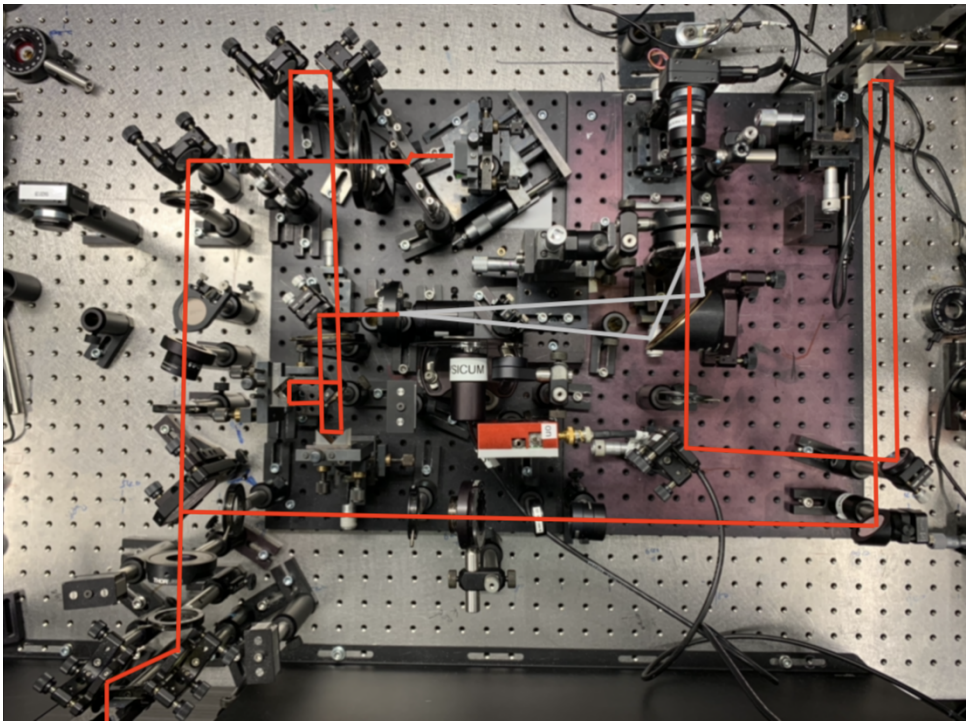

(b)

Figure 31: Schematic (a) and picture (b) of the finished narrowband terahertz generation setup.

doubled light. The setup is shown in figure 33.

The path length difference could be calculated and compensated for by the translation stage when adding the removed optics from each arm. Similarly to the previous setup, the final overlap between terahertz and probe pulse was found by moving the stage around

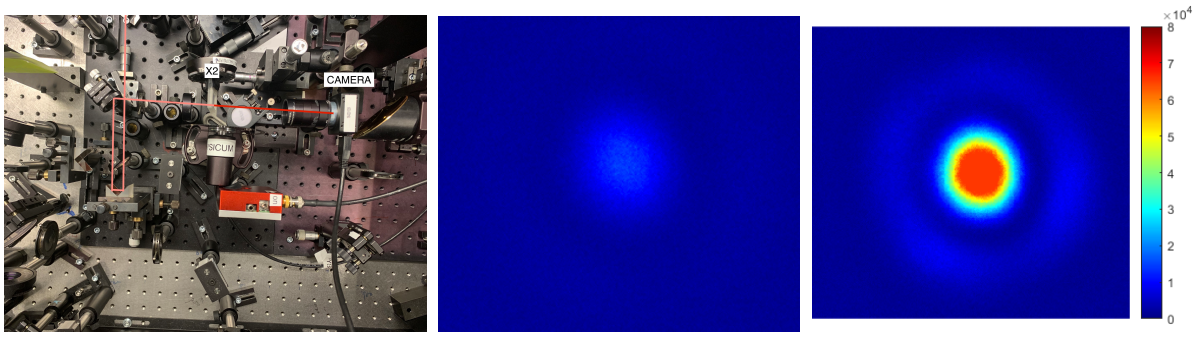

(a) (b) (c)

Figure 32: In (a) the setup when using frequency-doubling to temporally and spatially overlap the pulses after the interferometer is shown. The doubled 750 nm light detected with the camera without (b) and with (c) temporal overlap of the pulses increases drastically due to the nonlinearity in the process.

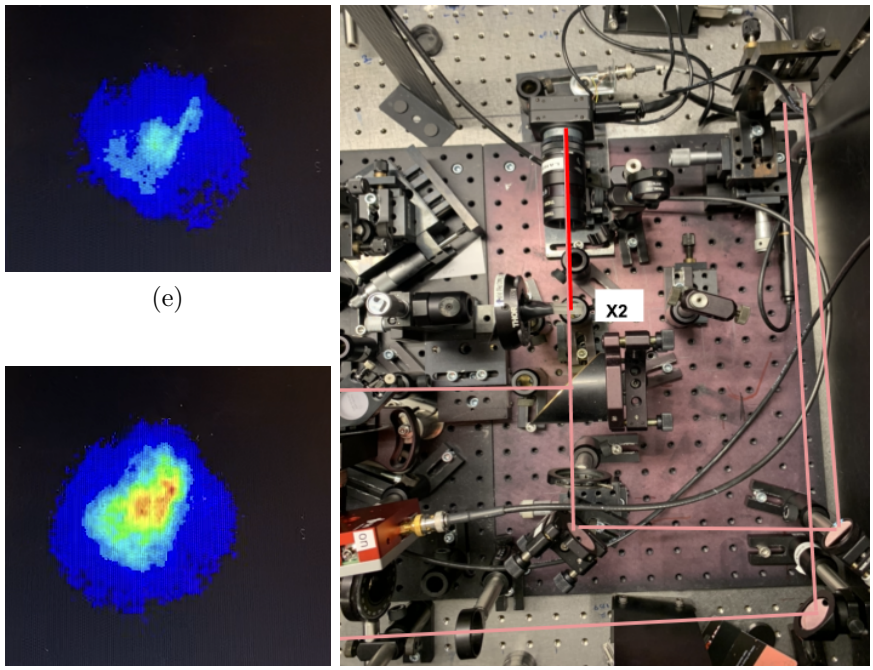

(e) (f) (d)

Figure 33: In (d) the setup when using frequency-doubling to temporally and spatially overlap pump and probe pulse for 1500 nm. The doubled 750 nm light detected with the camera without (e) and with (f) temporal overlap of the pulses increases drastically due to the nonlinearity in the process.

the overlap region mapped out by the frequency mixing process, and moving the probe beam and crystal around until a rotation of the probe spot could be seen. This time, the terahertz rotation was much more difficult to see initially, than it was for the previous setup.

4.4.4 Measuring the beat frequency spectrum

Having optimized the optical setup and found signal with the electro-optic sampling for the un-stretched pulses, the gratings were added to do the same for the stretched pulses. When pulses are overlapped, with a relative delay, the theory extensively discussed that this resulted in fringes in the temporal intensity envelope. The spectrum of the interfering pulses also obtain a fringe pattern, since the relative temporal delay of the two pulses results in a difference in their spectral phases which scales with the relative time delay. As a first step to verify the overlap of the pulses and that their relative delay was modified by changing the path length between arms, the spectra of the beating pulses before the organic crystal were measured for varying delays. This was done by aiming an IR-spectrometer towards a paper placed in front of the organic crystal, and changing the relative delay between the pulses to vary the beat frequency. A few of the acquired spectra are shown in the last section of the results.

This was the last laboratory work that was completed within the time-frame of the Master thesis. The steps remaining are to measure the narrowband terahertz pulses with the terahertz powermeter, and to find signal with the electro-optic sampling setup.

5 Experimental results

This section presents the experimental results obtained during the project. It also contains some explanations of how the data analysis was conducted. Most discussion of the results are deferred to the following discussion-section.

5.1 The filtered OPA signal

Figure 34 shows the spectrum after filtering the idler using two Brewster polarizers.

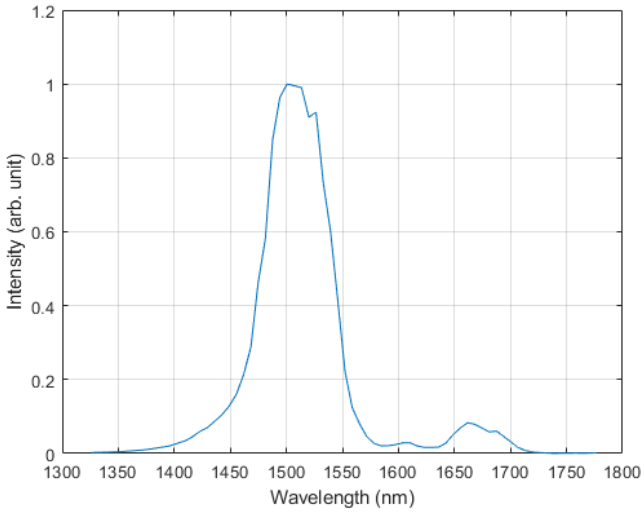

Figure 34: Background subtracted spectrum of signal from OPA after Brewster polarizers.

The OPA signal is centered around 1500 nm and has a full-width at half-maximum of approzimately 60 nm. Some of the idler is left, centered around 1650 nm, but as is clear from the spectrum, most of the idler is filtered out.

5.2 Terahertz generation from un-chirped IR-pulses

This section presents results associated with the terahertz generation setup from the un-chirped pulses, characterized with electro-optic sampling with the 0.5 mm thick ZnTe crystal and the 100 μm GaP crystal. The setup for terahertz generation exists in two versions; one in which the signal from the optical parametric amplifier was used directly to generate terahertz pulses (shown in figure 27), denoted setup I, and one in which the pulse was first split into two and recombined in the Michelson interferometer (shown in figure 31, but without gratings), denoted setup II.

5.2.1 Terahertz power and spot size

In setup I, the fluence level of the OPA beam was higher than the damage threshold of the organic crystal and the terahertz filters, so that the pump beam had to be attenuated. Initially it was attenuated a factor $10^{-1.3}$, which was later lowered to 10^{-1}. The terahertz powermeter saturated for voltages higher than 2.5 V. An unsaturated terahertz

trace sampled with the powermeter is shown in figure 35a, when the pump beam was attenuated. The signal was modulated by the chopper operating at 10 Hz (see methods section), and the terahertz power is given by the peak-to-peak voltage of the trace. The voltage can be converted to power with the conversion factor 85 000 V/W. The average power and the pulse energy of the trace in the figure would thus be given by:

$$P_{avg} = \frac{0.91\text{V}}{85000\text{V/W}} = 10.7\mu\text{W}$$
$$E_{pulse} = \frac{P_{avg}}{f} = \frac{10.7\mu\text{W}}{3000k\text{Hz}} = 3.57\text{nJ}$$

For an incident pulse energy of 13 μJ, this would correspond to a conversion efficiency of 0.0275%. This is very low, when at least 0.5-1% was expected. The highest detected pulse energy was 20 nJ, with a conversion efficiency around 0.1%, which was achieved when the beam was magnified with the telescope. This had to be measured with another powermeter, since the one used before saturated. The other powermeter had a larger sensitive area and was placed closer to the generation crystal, so the terahertz was not focused.

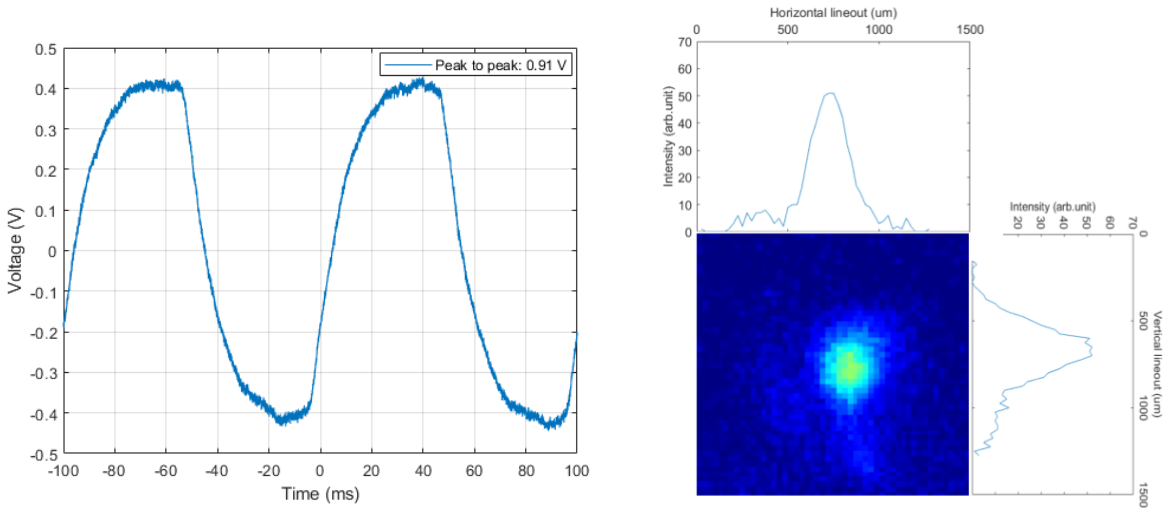

(a) (b)

Figure 35: Oscilloscope trace (a) of generated terahertz radiation measured with the Swiss Terahertz powermeter (shown in figures of experimental setup). Spot size of terahertz after focused with the parabolic mirror.

A smoothed image of the terahertz spot focused with the parabolic mirror is shown in figure 35b, acquired with the terahertz camera. Along each side are horizontal and vertical lineouts of the spot size. The full-width at half-maximum were estimated to 250 μm for the horizontal and 325 μm for the vertical.

5.2.2 Probe beam and effect of terahertz rotation

Figure 36 shows the effect when the terahertz pulse rotates the polarization of the probe spot when the wave-plate is removed after the electro-optic crystal. That the rotation

of the probe beam could be clearly seen on the camera proved useful when finding the overlap, as described in the methods section, instead of scanning the step and analyzing intensity differences. It was also convenient to scan the overlap without the waveplate and plot the intensity difference of the left spot, since this could give a clear indication of what step position corresponded to temporal overlap between pulses.

The images in figure 36a are sum images from a scan, where 36a is the sum of 200 images outiside of the overlap region, and 36b is a sum of 200 images when the pulses are overlapped. When the pulses are not overlapped, the probe pulse propagates unaffected through the electro-optic crystal, and the linearly polarized beam results in only one spot on the camera. When the terahertz pulse coincides with the probe pulse, it induces and elliptical polarization of the probe pulse, so that the other electric-field component becomes larger, and the intensity in the second spot increases.

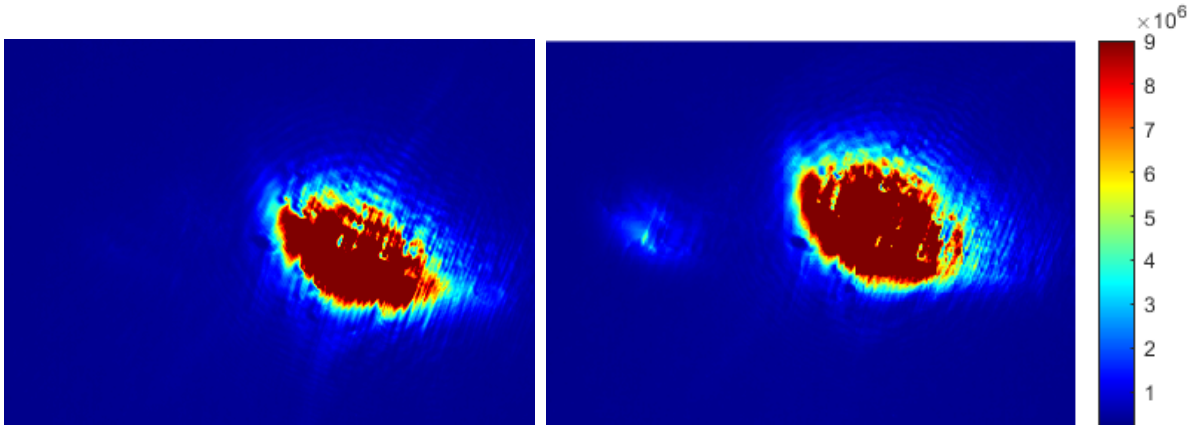

(a) (b)

Figure 36: Effect of terahertz on probe spot. The quarter-wave plate is not used, so that the probe beam is linearly polarized. (a): the sum of 200 images acquired over a scan range with no temporal overlap between probe and pump spot. (b): the sum of 200 images acquired over the scan range of the temporal overlap region.

5.2.3 Sampled terahertz pulses

When the quarter-wave plate is rotated 45° relative the optical axis of the electro-optic crystal, the linearly polarized probe beam becomes circularly polarized, and the detection scheme becomes balanced, as described in the theoretical background. The two spots are shown in figure 37, together with the area corresponding to the spatial overlap between terahertz and probe pulse.

The script for analyzing the acquired images is included in Appendix A, where the spatial overlap is looked for in the spots by calculating a center of gravity in each spot. Regions close to the center of gravity are then divided into blocks, and the intensity difference for the sum of each block pair is plotted, in order to find the region with spatial overlap. The normalized intensity difference is directly proportional to the electric field strength of the terahertz spot through equation 30.

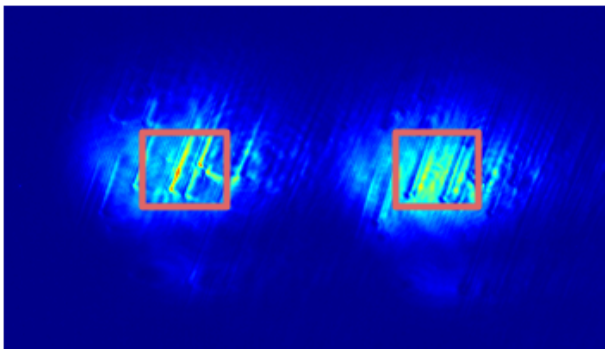

Figure 37: Region in which the intensity difference is evaluated. The sum of all pixel values in each block is taken.

	ZnTe	GaP
EO-coefficient (r_{41})	3.9 pm/V	1 pm/V
Refractive index (n)	2.88	3.22
Thickness	0.5 mm	100 μm

Table 1: Values to compute the electric field of the terahertz pulses with ZnTe and GaP.

Pulses sampled with the 0.5 mm thick ZnTe crystal and the 100 μm GaP crystal are shown in figures 38 and 39, together with their normalized intensity differences. Polynomial curves of suitable degree were fitted to the data and subtracted to remove intensity drifts during the scan. Values used to compute the electric field of the sampled pulses can be found in table 1 for ZnTe and GaP, and the equation is given in the theoretical background by equation 30. The probe pulse wavelength used is 750 nm.

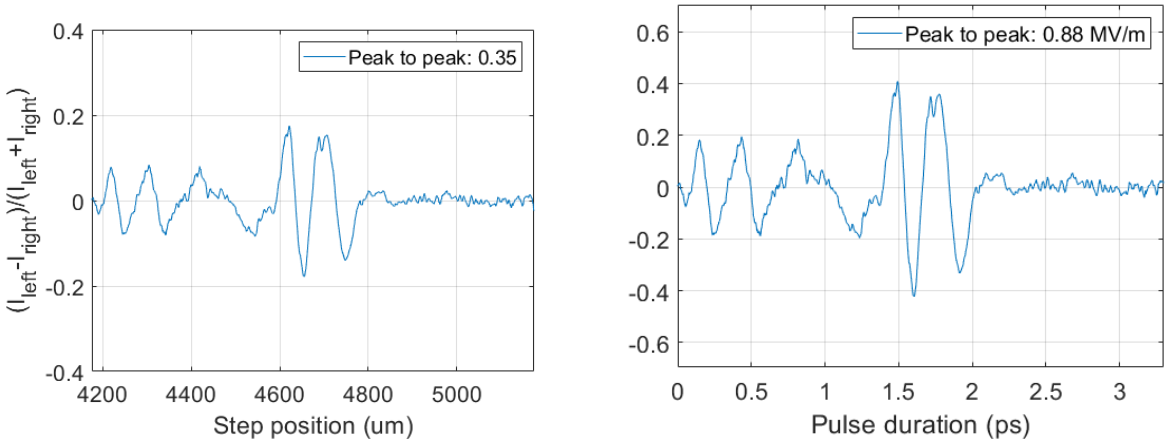

(a) (b)

Figure 38: Normalized intensity difference (a) between two blocks as illustrated in figure 37 and the corresponding electric field calculated from this (b) for the 0.5 mm thick ZnTe crystal. Both curves are low-pass filtered to remove noise.

Figures 38a and 39a show the smaller expected rotation of the probe pulse polarization of the GaP crystal, but differ in their translation to electric-field strengths. Possible

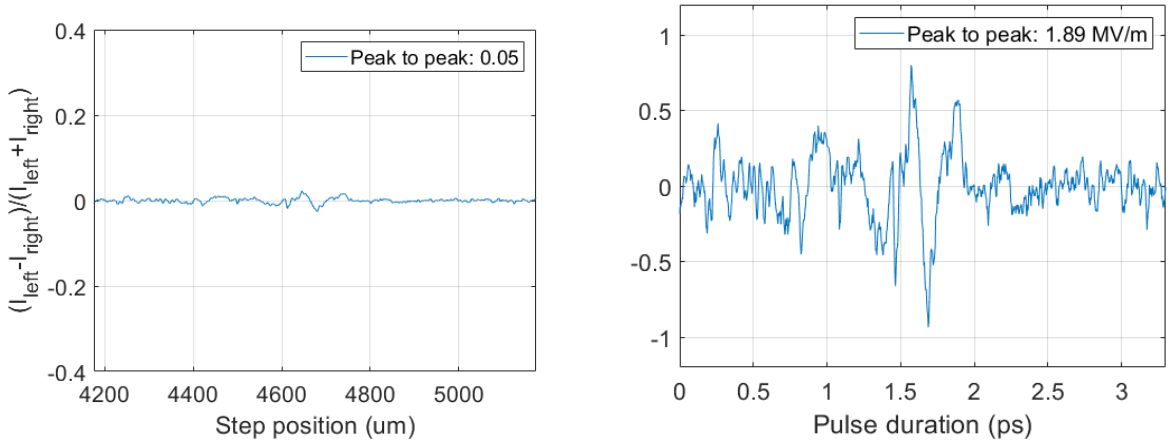

(a) (b)

Figure 39: Electric field trace (a) of a broadband terahertz pulse sampled with the 100 μm thick GaP crystal and its corresponding spectrum in (b).

explanations are the thickness of the crystal relative the Rayleigh range of the focused beams, or different placements of the crystals relative the focal plane of the parabolic mirror, as discussed further in the discussion section.

The corresponding pulse energies can be calculated from the peak electric fields through:

$$E_{pulse} = \frac{E_{field}^2 n A \tau_{pulse}}{2\eta_0}$$

which gives pulse energies of 0.4 nJ (ZnTe: $n = 2.88$, E_{field}=0.88 MV/m) and 2.12 nJ (GaP: $n = 3.22$, E_{field}=1.9 MV/m). The other parameters used are $\tau_{pulse} \approx 0.7$ ps (estimated from the EO-trace), $A \approx (250\ \mu\text{m})^2\pi$ and $\eta_0 = 377\ \Omega$.

5.2.4 Pulse spectra

When computing Fourier transforms of sampled signals, drifts in intensity can cause uneven endpoints of the intensity levels, which can introduce noise to the spectrum when computing the discrete Fourier transform. Preferably, the signal should be padded with zeros at the ends of the vector end points, and multiplied to an even multiple n of 2^n. Higher resolution can sometimes be obtained by increasing the number of multiples of 2^n.

The electric field in figure 38b is used as an example to show how the data was modified in order to minimize noise in the Fourier transform. Drifts in intensity over the duration of a scan can be compensated by fitting a polynomial curve of suitable degree to the data and subtracting it. Such a fitted curve and its resulting graph are shown in figure 40, where the drift is approximated with a second degree curve.

When the intensity levels of the scan are non-zero at the end points, this can be compensated for by multiplication of apodization curves. The apodization curve should be such that the relevant signal is contained within the high-amplitude part of the curve,

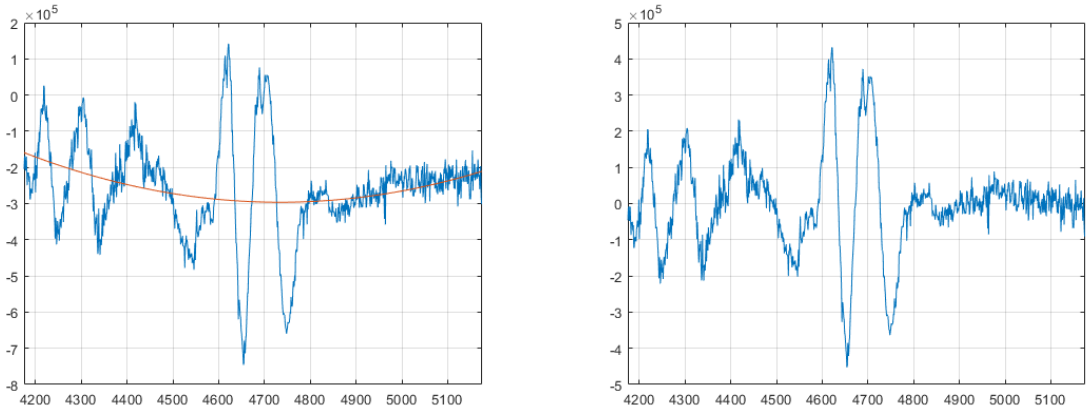

(a) (b)

Figure 40: Removing drift in intensity during the scan by subtracting the data with a fitted polynomial curve.

and the curve should approach zero towards the edges. Normally, different $\cos^2$-curves are suitable, since they are smooth and have a suitable shape. The approximation of an apodization curve to the plot in figure 40b is shown in figure 41a, and the resulting curve when multiplied with the apodization function is shown in figure 41b.

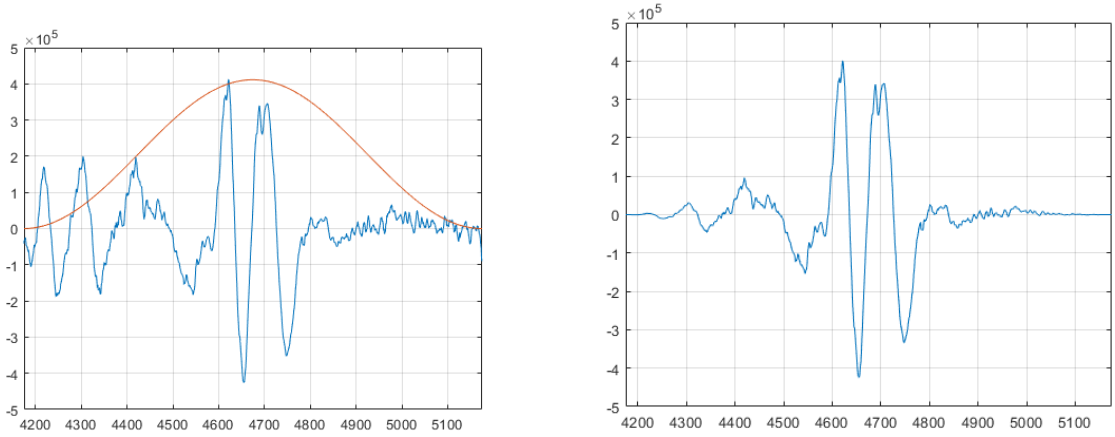

(a) (b)

Figure 41: Apodization to remove effects on the edges of the sample. The apodization curve is shown in (a) and the result of multiplying it with the data in (b).

The apodization curve used above is a Hann window, created with the Tukey function for generating tapered cosine functions in Matlab. The data below has also been lowpass filtered to reduce the noisy appearance of the signal.

The pulse spectra are computed using the DFT after cleaning up the data according to the procedure described above. The sampling frequency for the DFT is given by the temporal resolution in the measurement. The step was moved in approximately 0.96 μm steps, which corresponds to a total path length between each sample of 1.92 μm, and a temporal resolution of 6.4 fs. This gives a sampling frequency of 156 THz when

computing the Fourier transform. Figures 42ab show spectra centered around 1.6 THz, rapidly decreasing when approaching 4 THz for both the ZnTe and GaP crystal.

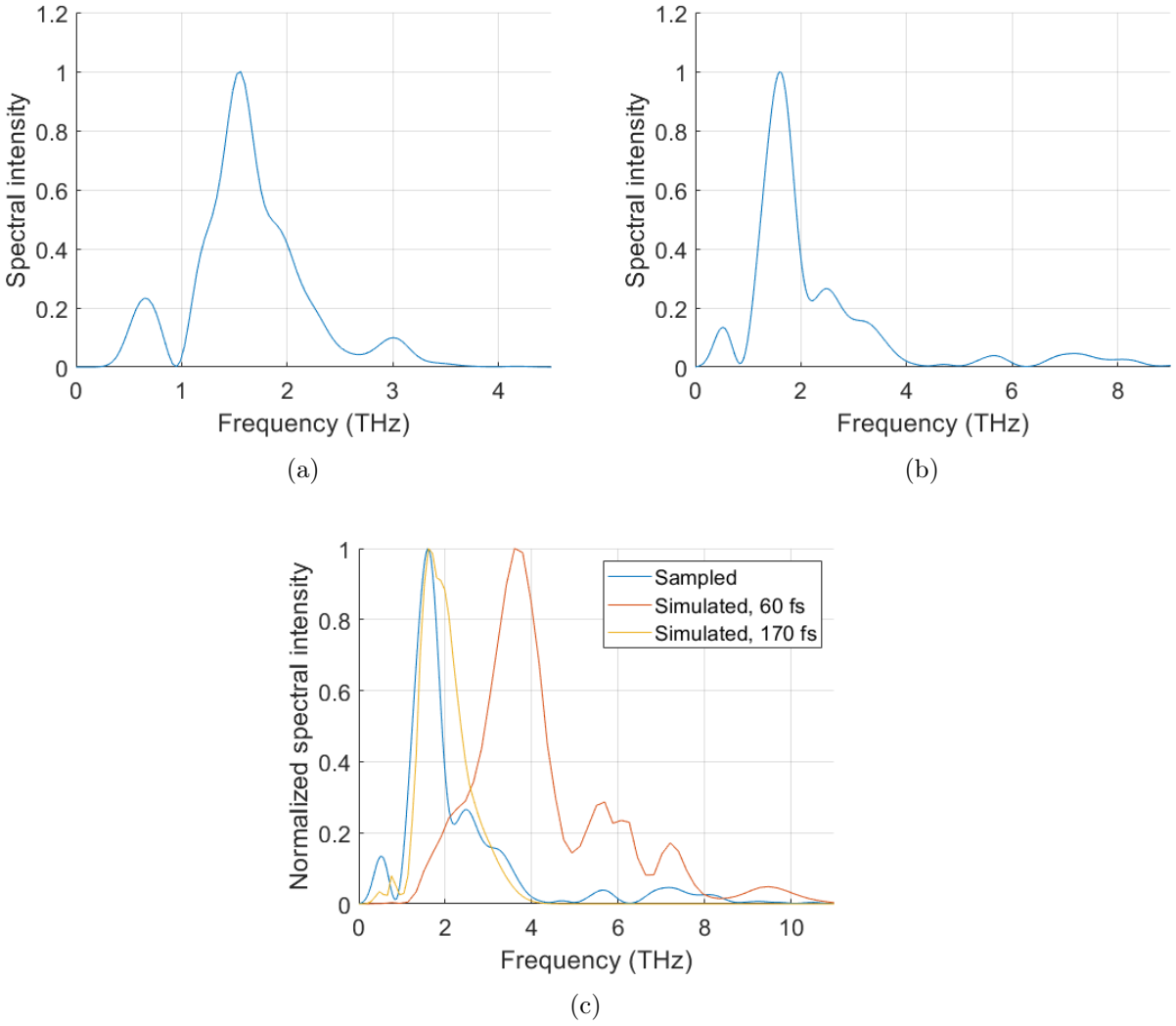

Figure 42: Normalized spectrum of the 0.5 mm thick ZnTe crystal (a) and the 100 μm thick GaP crystal (b) for the pulses sampled in figures 38b and 39b respectively. c) Shows the GaP spectrum compared to a simulated spectrum for two different pump pulse lengths: 60 fs and 179 fs.

In figure 42c, the GaP spectrum is compared to a simulated spectrum of a terahertz pulse generated from an un-chirped pump pulse. Phase-matching and absorption were included through the simple model introduced in section 2.4, where the effective length was used as a scaling factor of the spectrum according to equation 34. The effective length is given by equation 35 and values for refractive indices and absorption coefficients are given in section 3. The absorption of the pump laser was approximated to 70 m^{-1}. The pulses from the optical parametric amplifier were assumed to be around 60 fs long. However, the spectrum of the sampled pulses better match the simulated one for longer pump pulses, around 170 fs. The pulse duration out from the optical parametric amplifier was not measured during the project, and so the correct pulse duration is not known.

5.3 Towards narrowband terahertz generation

The narrowband terahertz setup was not completed during the project, but all components needed to generate the narrowband pulses were added to the setup, and the results from these are presented in this section.

5.3.1 Chirp filter and Michelson interferometer

The power incident on the chirp-filter was measured to 0.392 W, and after four passages, the power was measured to 0.26 W, corresponding to a transmission of 66%. With an expected transmission of 80% through four gratings with 95% transmission, this was considered acceptable.

The Michelson interferometer was extremely sensitive to differences in path length. Keeping the hollow-roof mirrors at constant distances relative each other for unstrecthed pulses (the gratings were removed for this), the generated terahertz radiation measured with the Swiss terahertz powermeter was periodically saturated and de-saturated. A possible explanation is small changes to the refractive index in the air between the two arms, changing the difference in optical path length for the two pulses. This is likely due to the chopper standing close to the interferometer, see figure 31.

5.3.2 Pulse beating spectra

In figure 43, spectra for two different time delays are shown, from which a change in fringe spacing is observed. This can be used to monitor the overlap between the pulses and control how much the pulse separation changes in the future setup.

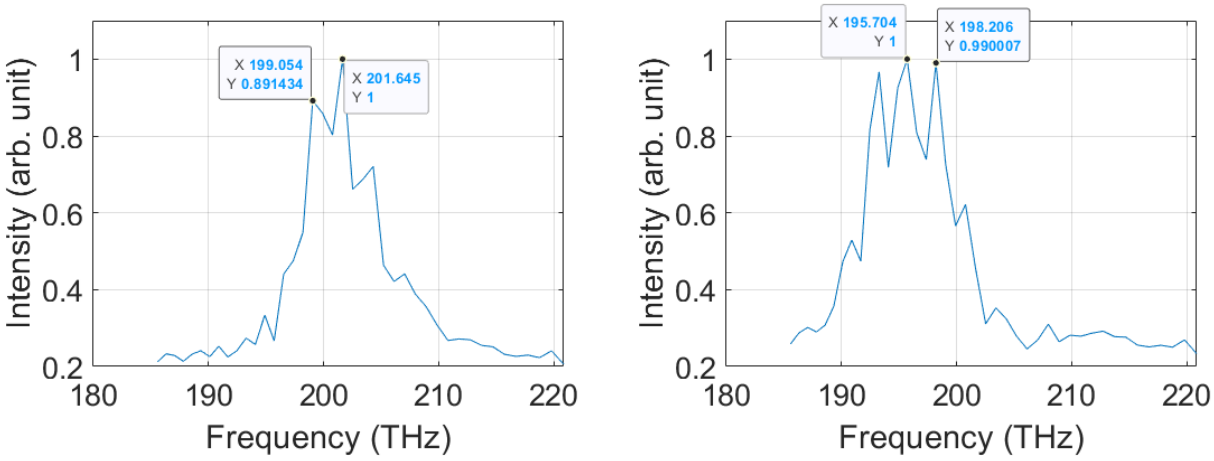

(a) (b)

Figure 43: Frequency spectra of the beating pulses after the Michelson interferometer.

6 Discussion

The DSTMS crystal gave a very low generation efficiency (as most 0.1%) even though the same crystal has previously been used to generate terahertz with a reported generation efficiency of 0.71% [32]. The crystal was burnt on multiple occasions, which is expected to have some effect, however not of the magnitude observed. However, the measurement with the Swiss terahertz powermeter (shown in figures of the experimental setup), corresponded well to the pulse energy estimated from the electro-optic sampling trace. When using the other detector, the terahertz was not focused since the sensitive area was large and the powermeter placed closer to the generation crystal (since the chopper was not needed inbetween crystal and powermeter to modulate the signal). However, the powermeter fluctuated a lot, making it difficult to determine the best position when measuring terahertz, which could have resulted in all of the terahertz not being absorbed by the sensitive area.

The sampled terahertz pulses showed two oscillations of the electric field. According to theory, optical rectification of an un-chirped pump pulse should result in the terahertz electric field making a single cycle in the far-field, where the pulse is likely sampled in this experimental setup. These two oscillations are likely originating from phase-mismatch and absorption of terahertz frequencies, most likely during the terahertz generation. The optimal length for terahertz generation with DSTMS is approximately 0.5 mm for 2 THz, and lower for higher terahertz frequencies [21]. The crystal used in the project was 0.54 mm thick, which likely resulted in phase mismatch during the generation process. When a phase mismatch is present, the phase velocity of the terahertz pulse propagates at a different velocity than the group velocity of the pump pulse, causing additional oscillations and temporal broadening of the terahertz pulse. In the spectral domain, the same phenomenon can be explained by considering that in the presence of a phase mismatch, not all frequencies in the terahertz and pump pulse propagate at the same velocity. Also, high absorption for some of the frequencies affect the spectral amplitude of the different frequencies, causing spectral narrowing by reduced spectral amplitude of frequencies that are more absorbed in the crystal, and that are further away from the fulfilled phase-matching condition.

From figures 16a and 16b, DSTMS can be seen to have perfect phase matching for a 1500 nm pump beam for generation of 1.7 THz, a large absorption peak at 1.025 THz and a smaller one at 0.65 THz. Comparing these properties of DSTMS to the spectra acquired with the 0.5 mm thick ZnTe and 100 μm thick GaP crystals in figures 42a and 42c, both absorption peaks appear slightly below 1 THz, and the spectrum is centered at 1.6 THz. Slight shifts to lower frequencies could possibly be due to heating of the crystal or slightly incorrectly measured step lengths.

From figures 38a and 39a the smaller signal from the GaP crystal is clear, and consistent with what is expected from theory. The significantly smaller electro-optic coefficient for GaP (1 pm/V) compared to that of ZnTe (3.9 pm/V) should result in a significantly weaker signal in the EO-trace, as observed. The electric field strengths calculated differ, however. One possibility is due to incorrect positioning of the electro-optic crystal when switching between different ones, so that the crystals ended up in different depths relative the terahertz focus. This was indicated by observing if a difference in rotation could be seen in the sampled data. The entire probe beam was divided into blocks in the same

way as illustrated by figure 37, and the intensity difference between each pair of blocks was plotted for the GaP and ZnTe crystals. All regions were rotated more or less in the ZnTe crystals, but only a few regions were rotated in the GaP crystal. This could indicate that the GaP crystal was placed closer to the focus than the ZnTe crystals, which would explain a stronger electric field.

Another possibility for the differing electric-field strengths is not accounting for electric-field variations across the crystal depth in equation 27. This would especially affect the thicker ZnTe crystal, since for this case the propagation length of pump and probe pulse exceed the Rayleigh range of the terahertz beam. For terahertz frequencies between 1 and 2 THz, focused to a spot size between 200 and 250 μm, the Rayleigh range can be approximated to be between 100 μm and 330 μm, which is shorter than the thickness of the ZnTe crystal. When calculating the electric field from the intensity difference, it is assumed to be homogeneous over the crystal length. In actuality, the electric field varies in strength across the ZnTe crystal. This results in a weaker estimated electric field strength, since the intensity difference is estimated to come from a longer region than it actually is. GaP is shorter than the Rayleigh range, making the estimation of a constant electric field strength of the terahertz field a better approximation for this crystal. If the electric field measured with the GaP crystal is assumed to be correct, the corresponding effective length of the 0.5 mm thick ZnTe crystal would be approximately 130 μm.

As mentioned in the introduction, the future intended application for the narrowband terahertz setup is generating narrowband terahertz pulses centered around 5.8 THz. For this, the large absorption of DSTMS for higher terahertz frequencies is clearly an undesirably characteristic of the crystal. However it constitutes a (slightly) favorable alternative compared to the absorption coefficient of DAST for polarization along the crystal a-axis. For this polarization, DAST has an approximate absorption of 150 cm^{-1}, compared to DSTMS which is around 140 cm^{-1}. Polarization along the b-axis in DAST could however be investigated, if pump wavelengths between 700-750 nm are available. For this generation configuration, the absorption coefficient is as low as 30-40 cm^{-1} in DAST[5]. However, the nonlinear coefficient is lower for the b-axis ($\approx$166 pm/V) compared to the a-axis ($\approx$212 pm/V), which results in less generated terahertz radiation [31].

As has been previously described, the main limitation to the signal strength of the terahertz is not the phase-matching as much as the absorption. However, phase-matching for 5.8 THz is best for 1400 nm pump light, and the change should not impact the electro-optic sampling significantly. For radiation around 5.8 THz, a thinner DSTMS crystal could potentially give a stronger signal. An approximation provided in [31] of the optimal crystal length, L_o, for terahertz generation is given by the maximum efficient crystal length through $1.6L_{max} \leq L_o \leq 2.2L_{max}$. For a maximum crystal length around 0.12 mm for 5.8 THz in DSTMS, this implies that a DSTMS crystal with a thickness between 190 μm and 260 μm could be suitable for generating pulses centered around 5.8 THz.

Sampling the 5.8 THz pulses is necessarily done with the GaP crystal, due to the

[5]For light polarized along the b-axis, DAST has more absorption peaks (7) than for polarization along the a-axis (5), and for broadband terahertz generation the a-axis is in general favorable. However, the very specific phonon resonance around 5.8 THz could potentially generate a stronger signal for b-axis polarized light in DAST.

phonon resonance around 5.3 THz in ZnTe. The drawback is a significantly reduced signal with the GaP crystal compared to the ZnTe, requiring a stronger signal. The thickness of the GaP crystal (100 μm) should be close to the optimal crystal length for sampling with GaP, as is more extensively discussed in [28].

7 Conclusion and outlook

In the project, a setup for broadband terahertz generation through optical rectification in DSTMS as well as a setup for electro optic sampling were successfully constructed. Few-cycle terahertz pulses were sampled with two ZnTe crystals of thicknesses 0.5 mm and 1 mm and a GaP crystal with thickness 100 μm. The setup was also extended towards generating narrowband terahertz pulses by adding chirp-and-delay of the terahertz pump pulses, but was not completed.

In the continuation, work should be continued on generating narrowband pulses with the extended setup. Suggested steps are:

1. Measuring the narrowband terahertz pulses with the powermeter.
2. Finding signal with the electro-optic sampling setup.
3. Finding the optimum crystal position for ZnTe (0.5 mm) and GaP and optimizing the electro-optic sampling.
4. Optimizing the narrowband terahertz generation.

Further improvements of the setup could be to add pulse compression of the probe pulse in the electro-optic sampling to obtain better temporal resolution of the sampled pulses [20]. The software for controlling the DC-motor could be extended to also control the camera and view the image, in order to create a more user-friendly sampling interface.

Future generation, optimization and electro-optic detection of narrowband terahertz pulses centered around 5.8 THz should be sampled with the GaP crystal used in the project (100 μm thick). The pump wavelength could be tuned to 1400 nm for better phase matching of the generation process, and will likely not have an impact on the electro-optic detection. A thinner DSTMS crystal ($\approx$200-250 μm) could potentially give a stronger signal for pulses centered around 5.8 THz. Another potential setup could be pumping a DAST crystal with $\approx$720 nm light, polarized along the crystal b-axis instead of the a-axis.

References

[1] Kampfrath, T., Tanaka, K. & Nelson, K. *Resonant and nonresonant control over matter and light by intense terahertz transients*. Nature Photon 7, 680–690 (2013). https://doi-org.ludwig.lub.lu.se/10.1038/nphoton.2013.184

[2] P. Salén, M. Basini, S. Bonetti, J. Hebling, M. Krasilnikov, A. Y. Nikitin, G. Shamuilov, Z. Tibai, V. Zhaunerchyk & V. Goryashko. *Matter manipulation with extreme terahertz light: Progress in the enabling THz technology.* Physics Reports, Volume 836, p. 1-74. (2009) https://doi.org/10.1016/j.physrep.2019.09.002.

[3] Daniel. K. Ferry. *Non-equilibrium longitudinal optical phonons and their lifetimes*. Appl. Phys. Rev. 1 June 2021; 8 (2): 021324. https://doi.org/10.1063/5.0044374

[4] Isgandarov, E., Ropagnol, X., Singh, M. et al. *Intense terahertz generation from photoconductive antennas*. Front. Optoelectron. 14, 64–93 (2021). https://doi.org/10.1007/s12200-020-1081-4

[5] Wynne, K. and Carey, J.J. *An integrated description of terahertz generation through optical rectification, charge transfer, and current surge.* Opt. Commun. 256 (4–6) (2005) 400–413. http://dx.doi.org/10.1016/j.optcom.2005.06.065.

[6] Cook, D. J. and Hochstrasser, R. M. *Intense terahertz pulses by four-wave rectification in air*. Optics Letters. 25(16):1210-1212 (2000).

[7] T. Hattori and K. Takeuchi, *Simulation study on cascaded terahertz pulse generation in electro-optic crystals*, Opt. Express 15, 8076-8093 (2007).

[8] Ahn, J., Efimov, A., Averitt, R. & Taylor, A. *Terahertz waveform synthesis via optical rectification of shaped ultrafast laser pulses*. Opt Express. 2003 Oct 6;11(20):2486-96. doi: 10.1364/oe.11.002486. PMID: 19471361.

[9] Vicario, C., Jazbinsek, M. Ovchinnikov, A. V., Chefonov, O. V., Ashitkov,S. I., Agranat, M. B. and Hauri, C. P. *High efficiency THz generation in DSTMS, DAST and OH1 pumped by Cr:forsterite laser*. Opt. Express 23, 4573-4580. (2015).

[10] Bradley, J.D.B. and Pollnau, M. *Erbium-doped integrated waveguide amplifiers and lasers*. Laser & Photon. Rev., 5: 368-403. (2011). https://doi.org/10.1002/lpor.201000015.

[11] Weling, A. S. and Auston, D H. *Novel sources and detectors for coherent tunable narrow-band terahertz radiation in free space*. J. Opt. Soc. Am. B 13, 2783-2792. (1996).

[12] Weling, A. S., Hu, B. B., Froberg, N. M. & Auston, D. H. *Generation of tunable narrow-band THz radiation from large aperture photoconducting antennas*. Appl. Phys. Lett. 10 January 1994; 64 (2): 137–139. https://doi-org.ludwig.lub.lu.se/10.1063/1.111543

[13] Chen, Z., Zhou, X., Werley, C. A. & Nelson, K. A. *Generation of high power tunable multicycle teraherz pulses*. Appl. Phys. Lett. 15 August 2011; 99 (7): 071102. https://doi-org.ludwig.lub.lu.se/10.1063/1.3624919.

[14] Liu, B., Bromberger, H., Cartella, A., Gebert, T., Först, M. & Cavalleri, A. *Generation of narrowband, high-intensity, carrier-envelope phase-stable pulses tunable between 4 and 18 THz*. Opt. Lett. 42, 129-131. (2017). https://doi.org/10.1364/OL.42.000129.

[15] Danielson, J. R., Jameson, A. D., Tomaino, J. L., Hui, H., Wetzel, J. D., Lee, Y-S. & Vodopyanov, K. L. *Intense narrow band terahertz generation via type-II difference-frequency generation in ZnTe using chirped optical pulses*. Journal of Applied Physics 1 August 2008; 104 (3): 033111. https://doi.org/10.1063/1.2959846

[16] Vicario, C., Trisorio, A., Allenspach, S., Rüegg, C. & Giorgianni, F., 2020. *Narrowband and tunable intense terahertz pulses for mode-selective coherent phonon excitation.* Applied Physics Letters, 117(10).

[17] Konstantin L. Vodopyanov. *Optical generation of narrow-band terahertz packets in periodically-inverted electro-optic crystals: conversion efficiency and optimal laser pulse format*. Opt. Express 14, 2263-2276. (2006).

[18] Lee, Y.-S., Meade, T., Perlin, V., Winful, H., Norris, T. B. & Galvanauskas, A. *Generation of narrow-band terahertz radiation via optical rectification of femtosecond pulses in periodically poled lithium niobate*. Appl. Phys. Lett. 1 May 2000; 76 (18): 2505–2507. https://doi-org.ludwig.lub.lu.se/10.1063/1.126390.

[19] Carbajo, S., Schulte, J., Wu, X., Ravi, K., Schimpf, D. N. & Kärtner, F. X. *Efficient narrowband terahertz generation in cryogenically cooled periodically poled lithium niobate*. Opt. Lett. 40, 5762-5765. (2015).

[20] Saleh, B. E. A. and Teich, M. C. *Fundamentals of Photonics*. (2019). John Wiley & Sons Inc. 3rd Edition.

[21] Stillhart, M., Schneider, A. & Gunter, P. *Optical properties of 4-N,N-dimethylamino-4 -N -methyl- stilbazolium 2,4,6-trimethylbenzenesulfonate crystals at terahertz frequencies*. J. Opt. Soc. Am. B 25, 1914-1919 (2008).

[22] Montemezzani, G., Alonzo, M., Coda, V., Jazbinsek, M. and Guenter, P. *Running electric field gratings for detection of coherent radiation*. J. Opt. Soc. Am. B-Opt. Phys. 2015, 32, 1078–1083.

[23] PlotDigitizer. Free online application. https://plotdigitizer.com/.

[24] Mutter, L., Brunner, F.D.,Yang, Z., Jazbinsek, M. & Gunter, P. *Linear and nonlinear optical properties of the organic crystal DSTMS*. J.Opt. Soc. Am. B 24, 2556-2561 (2007).

[25] E. B. Treacy. *Optical pulse compression with diffraction gratings*- IEEE J. Quantum Electron. QE-5, 454 – 458 (1969).

[26] Christov, I. P. and Tomov, I. V. *Large bandwidth compression with diffraction gratings*. Opt. Commun. 58, 338–342 (1986).

[27] Jolly, S. W., Matlis, N. H., Ahr, F. Leroux, V. Eichner, T. Calledron, A. L. Ishizuki, H. Taira, T. Kärter, F. X. & Maier, A. R. Spectral phase control of interfering chirped pulses for high-energy narrowband terahertz generation. Nat Commun 10, 2591 (2019). https://doi-org.ludwig.lub.lu.se/10.1038/s41467-019-10657-4

[28] B. R. Steffen. (2007). *Electro-Optic Methods for Longitudinal Bunch Diagnostics at FLASH.* [Doctoral dissertation, University of Hamburg]. https://inspirehep.net/files/c096f2644c215b4f18ed7d66fa799415.

[29] Bakker, H. J., Cho, G. C., Kurz, H., Wu, Q. & Zhang, X. C. *Distortion of THz pulses in electro-optic sampling*. J. Opt. Soc. Am. B 15, 1795–1801 (1998).

[30] Nahata, A., Weling, A. S.& Heinz, T. F. *A wideband coherent terahertz spectroscopy system using optical rectification and electro-optic sampling*. Appl. Phys. Lett. 14 October 1996; 69 (16): 2321–2323. https://doi.org/10.1063/1.117511

[31] Schneider, A., Neis, M. Stillhart, M. Ruiz, B. Khan, R. U. A. & Günter, P. *Generation of THz pulses through optical rectification in organic DAST crystals: theory and experiment*. J. Opt. Soc. Am. B 23, 1822–1835. (2006).

[32] Bengtsson, Å. *Characterization of Terahertz Radiation Generated in an Organic Crystal*. [Master thesis]. (2016).

A Code

In the project the software developed was written in two programming languages: MATLAB and LabVIEW. LabVIEW is a graphical programming language with a front-end interface that the user interacts with during the program execution, and back-end code that determines the behaviour of the program. The code consists of icons, and the lines connecting them determines the execution order. This is called data flow programming, in which the execution order follows the flow of the lines from left to right.

A LabVIEW program was written for moving the stage in a sequence and sending a digital trigger signal every time the step had moved. For controlling the camera, a program written by Dr. Anders Persson was used, but since it was not developed by myself it is not described further here. The analysis scripts were written in MATLAB, which is a conventional text based programming language. A script was written for analyzing the intensity change in the images captured when the stage was scanned.

A.1 LabVIEW code for motorized stage

The first page in the front-end panel is for general control of the DC-motor. It can be moved to a position (given in μm) by entering the step position in "Move to" and pressing "Move". The current position is shown by "CURRENT POS" and "MOTOR STATE" shows if the motor is moving, idle or homing. When the T-CUBE is initially started it should be "homed", so that zero is reset as zero. More features than were implemented here are available in the software provided by the manufacturer.

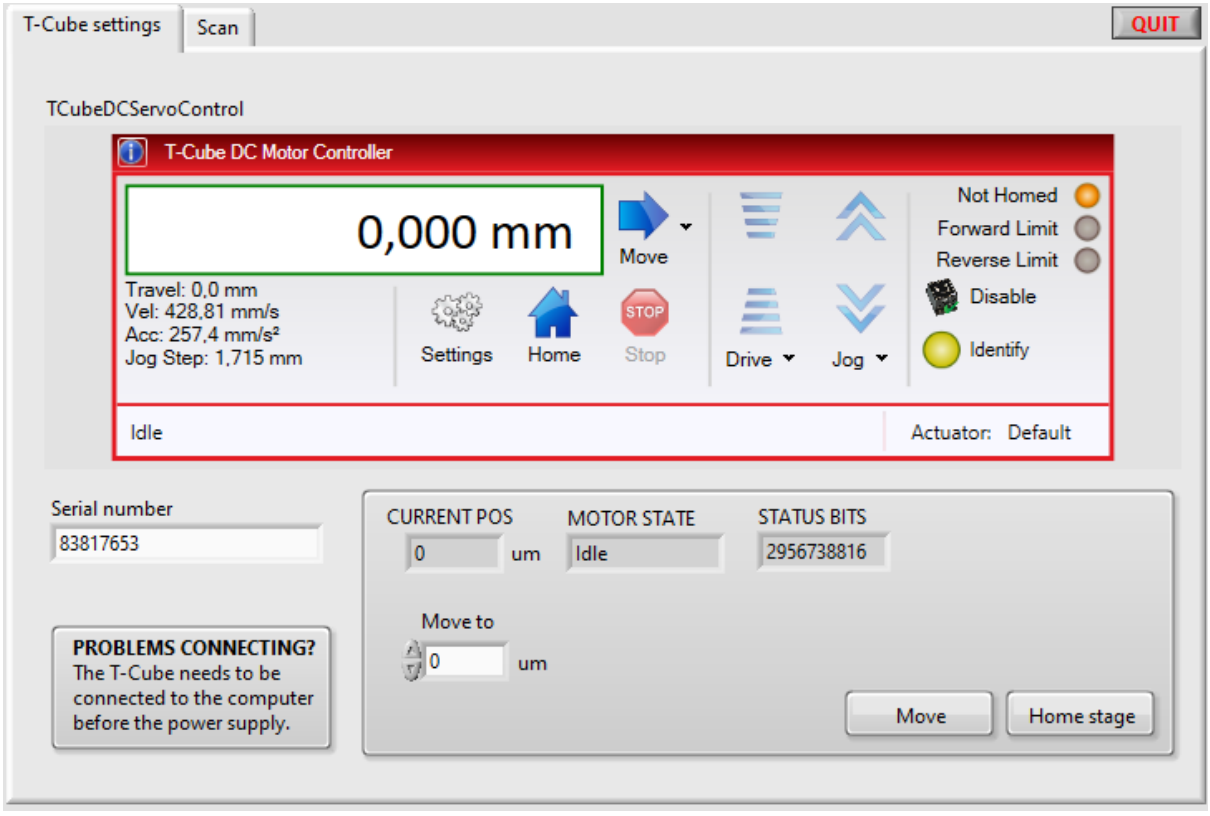

Figure 44: Tab for general control of T-CUBE.

The scanning range and other scan parameters are provided in the ”Scan”-tab. When the DC-motor performs a scan, it moves to the step position input into ”START POSITION”, moves a fix step size given by ”STEP SIZE” until it reaches the step position defined by ”END POSITION”. How long the motor should pause between each step is determined in ”STEP DELAY” where a default value of 500 ms is initially set, but can be changed if needed. If the motor should take very small (less than 1 μm) steps, the time to pause needs to be increased a bit so that the motor has time to ”stabilize” at a certain step position. For scanning 1 μm long steps, 500 ms is a good time to pause between steps. The current position of the T-CUBE is shown in ”T-CUBE CURRENT POSITION”. The scan is started by pressing ”Start scan” after inputting parameters, and the scan can be ended in the middle by pressing ”Stop scan”, but it may be a bit slow to stop. If the step is scanning, this is indicated by the green lamp ”Scanning” being lit.

Each step position that the motor stops at is stored into a text file, determined by the file path in ”Step position file”. Each time the step stops during the scan, it also sends out a digital trigger signal. What port to send the trigger signal on is defined by ”PORT TO TRIGGER ON”, where available choices show up in the roll-down menu.

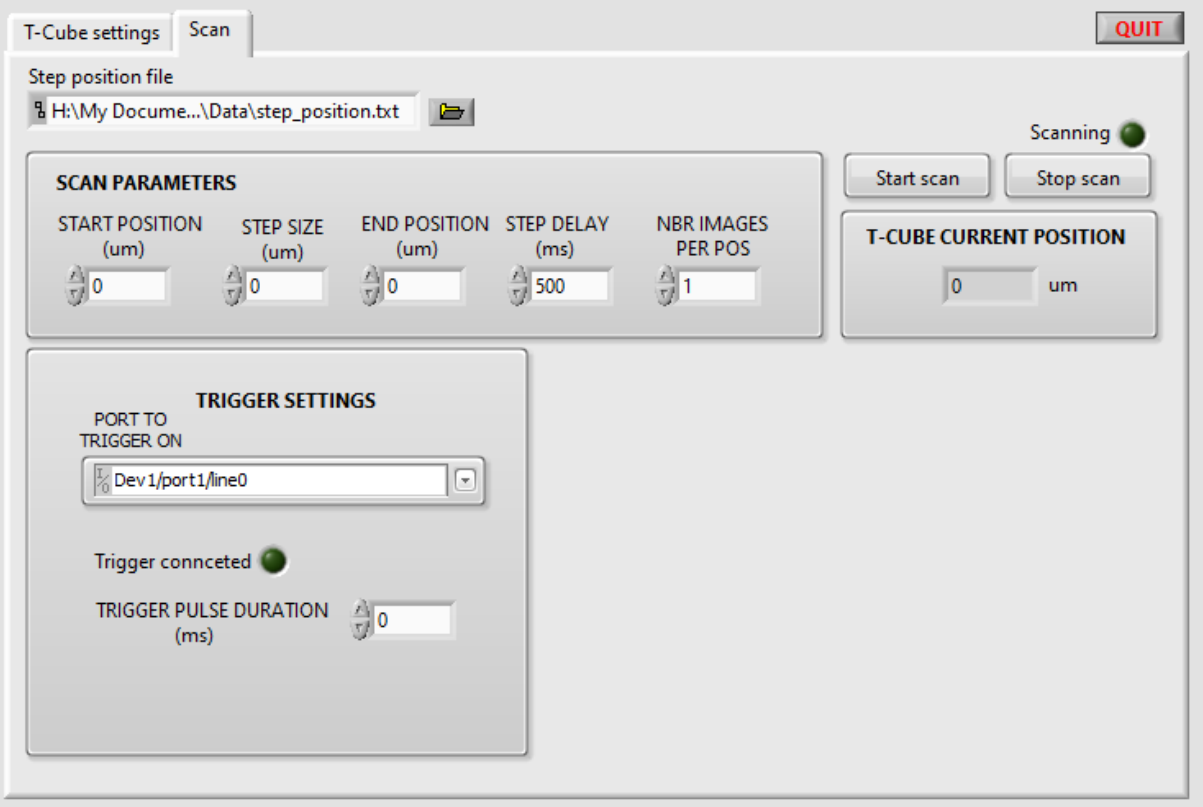

Figure 45: Tab for performing scans.

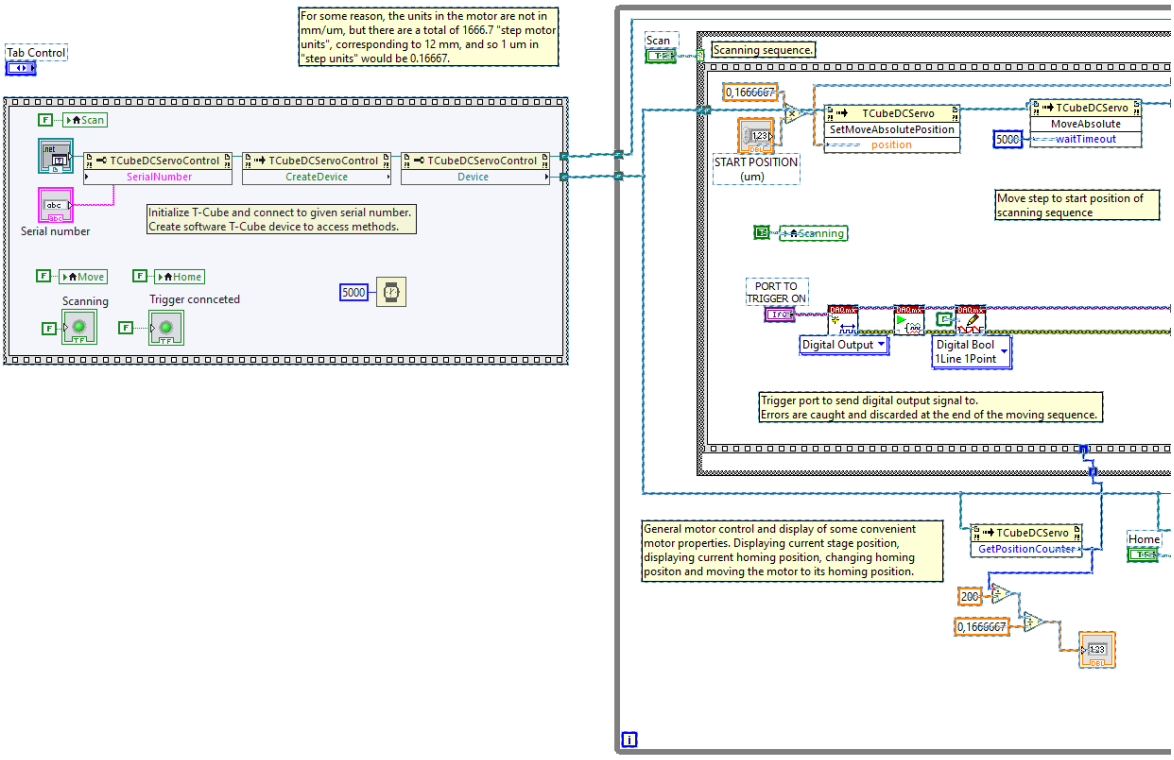

Figure 46: Back-end part 1.

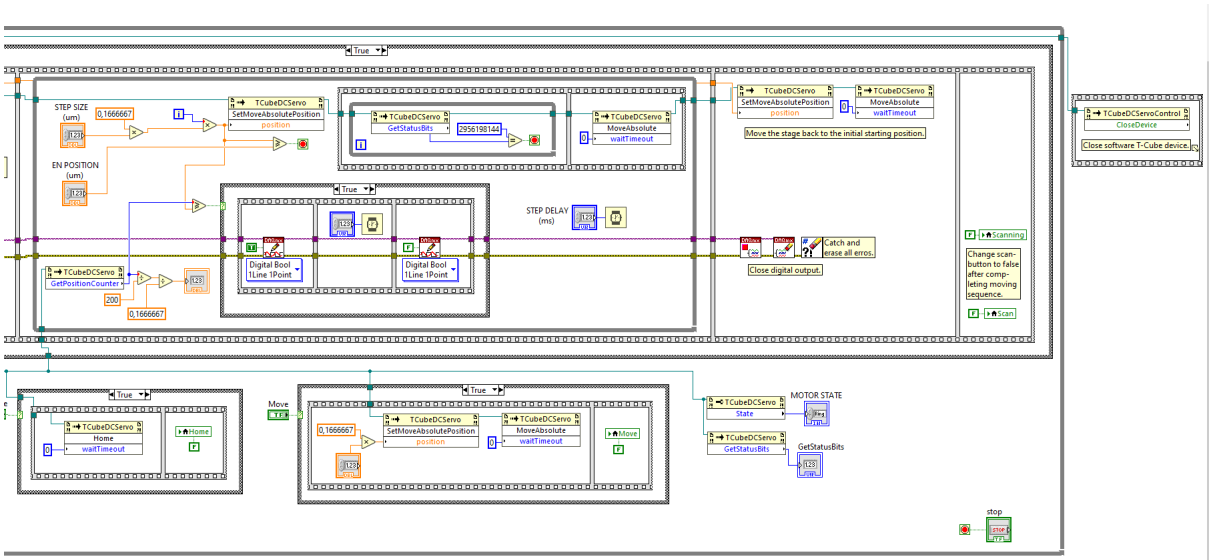

Figure 47: Back-end part 2.

A.2 MATLAB script for evaluation of scan data

```
clc;
clear all;
close all;

warning('off', 'all');

%% Constant parameters
sum_image_contrast = [0 10000000];
single_image_contrast = [0 1000];
box_stretch_factor = [1 1];

%% Read file with probe spot images and text file with step position,
% save to image_array and step_array
directory = ["C:/Scans/OVERLAP/1mm range/gap-scan3"];
step_array = load('C:/Scans/OVERLAP/1mm range/gap-scan3.txt');

files = dir([convertStringsToChars(directory(1)) '/*.png']);
step_array = step_array(1:length(files));
image_array = cell(length(directory), (length(files)));

for k = 1:length(directory)
    files = dir([convertStringsToChars(directory(k)) '/*.png']);

    for i = 1:length(files)
        file_path = [convertStringsToChars(directory(k)) '/' files(i).name];
        image_arrayk,i = imread(file_path);
    end
end

%% Define spot size parameters on camera
pixel_size = 4.8e-6;
magnification = 2/5;

pump_spot_size = 200e-6;
probe_spot_size = 600e-6;
aperture_size = 500e-6;

pump_block_size = pump_spot_size/pixel_size*magnification;
probe_block_size = probe_spot_size/pixel_size*magnification;
aperture_img_size = aperture_size*magnification;

nbr_blocks = 1;%cast((probe_spot_size/pump_spot_size)^2, 'single');
if rem(nbr_blocks, 2) == 0
    nbr_blocks = nbr_blocks+1;
```

```
end

%% Get probe spot sum image
sum_image = cast(image_array1, 1, 'uint32');
for i = 2:length(image_array)-1
    sum_image = sum_image + cast(image_array1, i, 'uint32');
end

%% Define what image to define center of gravity from and its contrast
image_cog = sum_image;
contrast = sum_image_contrast;

%% Define pixel limit to divide between the two spots
limit = 460;

left_right_image = segment_left_right(image_cog, limit);
left_spot = left_right_image1, 1; right_spot = left_right_image1,2;

%% Draw grid to help determine cog mask
figure; draw_grid(left_spot, probe_block_size);
title('Left spot'); clim(contrast);
figure; draw_grid(right_spot, probe_block_size);
title('Right spot'); clim(contrast);

%% View cog mask
left_spot_mask = left_spot(390:550, 300:460);
figure; imshow(left_spot_mask); title('Left spot'); clim(contrast);
right_spot_mask = right_spot(390:550, 10:170);
figure; imshow(right_spot_mask); title('Right spot'); clim(contrast);

%% Calculate and show center of gravity for the two spots
left_mask = [390 520 310 470];
right_mask = [390 520 1 140];

cog_left = get_cog(left_spot, left_mask);
cog_right = get_cog(right_spot, right_mask);

figure; imshow(left_spot); hold on; plot(cog_left(1), cog_left(2), 'bo');
title('Left spot'); clim(contrast); hold off;
figure; imshow(right_spot); hold on; plot(cog_right(1), cog_right(2), 'bo');
title('Right spot'); clim(contrast);

%% Show the blocks that the spots are divided into to search for overlap
left_spot_blocks = segment_image(left_spot,
    pump_block_size, nbr_blocks, cog_left, box_stretch_factor);
```

```
right_spot_blocks = segment_image(right_spot,
    pump_block_size, nbr_blocks, cog_right, box_stretch_factor);

figure; draw_blocks(left_spot_blocks, 3, sum_image_contrast);
figure; draw_blocks(right_spot_blocks, 3, sum_image_contrast);

%% Check background blocks
background_left = get_background(left_spot, cog_left,
    probe_block_size, pump_block_size);
background_right = get_background(right_spot, cog_right,
    probe_block_size, pump_block_size);

figure; imshow(background_left); clim(sum_image_contrast);
figure; imshow(background_right); clim(sum_image_contrast);

%% Determine normalized intensity difference between block in left
% and right spot

difference_matrix = zeros(nbr_blocks, length(image_array), length(directory));

sum_intensity_matrix_left = zeros(nbr_blocks, length(image_array),
    length(directory));
sum_intensity_matrix_right = zeros(nbr_blocks, length(image_array),
    length(directory));

background_intensity_matrix_left = zeros(1, length(image_array),
    length(directory));
background_intensity_matrix_right = zeros(1, length(image_array),
    length(directory));

section_length = length(files);
for i = 1:length(directory)
    start = 1;
    stop = section_length;

    last = false;
    while stop <= length(step_array)

        index = 1;
        for j = start:stop

            image = image_arrayi,j;

            left_right_image = segment_left_right(image, limit);
            left_spot = left_right_image1, 1;
```

```
    right_spot = left_right_image1, 2;

    left_spot_blocks = segment_image(left_spot, pump_block_size,
        nbr_blocks, cog_left, box_stretch_factor);
    right_spot_blocks = segment_image(right_spot, pump_block_size,
        nbr_blocks, cog_right, box_stretch_factor);

    background_left = get_background(left_spot, cog_left,
        probe_block_size, pump_block_size);
    background_right = get_background(right_spot, cog_right,
        probe_block_size, pump_block_size);

    background_intensity_matrix_right(j) = sum(background_right, 'all');
    background_intensity_matrix_left(j) = sum(background_left, 'all');

    for k = 1:nbr_blocks

        left_block = left_spot_blocks1, k;
        right_block = right_spot_blocks1, k;

        sum_left = sum(left_block, 'all');
        sum_right = sum(right_block, 'all');

        sum_left_sub_bg = sum(left_block, 'all')
            - sum(background_left, 'all');
        sum_right_sub_bg = sum(right_block, 'all')
            - sum(background_right, 'all');

        sum_intensity_matrix_left(k,j,i) = sum_left;
        sum_intensity_matrix_right(k,j,i) = sum_right;

        difference_norm = (sum_left_sub_bg-
            sum_right_sub_bg)/(sum_left_sub_bg+sum_right_sub_bg);
        difference_matrix(k,j) = difference_norm;

    end

    index = index + 1;

end

start = stop;
stop = stop + section_length;
if stop > length(step_array) && ~last
    stop = length(step_array);
```

```
            last = true;
        end

    end
end

%% plot spot intensity and background for the scan
figure;
step_array = step_array(1:length(files));
plot(step_array, background_intensity_matrix_left); hold on;

for block_index = 1:nbr_blocks
    plot(step_array, sum_intensity_matrix_left(block_index, :, 1)); hold on;
end
title('Left spot intensity, 1 um Gap - scan 3');

figure;
step_array = step_array(1:length(files));
plot(step_array, background_intensity_matrix_right); hold on;

for block_index = 1:nbr_blocks
    plot(step_array, sum_intensity_matrix_right(block_index, :, 1)); hold on;
end
title('Right spot intensity, 100 um Gap - scan 3');


%% plot change in normalized intensity for the scan
fsize = 16;
degree = 7;
fitted_polynomial = polyfit(step_array, difference_matrix, degree);
curve_from_fit = polyval(fitted_polynomial, step_array);

subtracted = difference_matrix - curve_from_fit';
diff = smooth(subtracted);

figure; plot(step_array, diff);

ylim([-0.4 0.4]); xlim([step_array(1) step_array(length(step_array))]);
xlabel('Step position (um)','FontSize',fsize);
ylabel('(I_left-I_right)/(I_left+I_right)','FontSize',fsize);
legend(sprintf('peak to peak: %.2f', ptp)); grid on;

%% Compute the electric field corresponding to the normalized
%intensity change
```

```
% parameters for ZnTe crystal
lambda = 750e-9; d = 500e-6; n0 = 2.88; r41 = 4.3e-12;

% parameters for Gap crystal
% lambda = 750e-9; d = 100e-6; n0 = 3.22; r41 = 1e-12;

Ethz = asin(difference_matrix).*lambda/(2*pi*d*n0^3*r41);
time = linspace(0, length(step_array), length(step_array)).*10^(-6)./3e8;
time = time*10^(12);

degree = 7;
fitted_polynomial = polyfit(step_array, Ethz, degree);
curve_from_fit = polyval(fitted_polynomial, step_array);

subtracted = Ethz - curve_from_fit';
subtracted = smooth(subtracted);

figure; plot(time, subtracted*10^(-6)); xlabel('pulse duration (ps)');
grid on; legend(sprintf('peak to peak: %.2f MV/m', ptp_thz*10^(-6)));
ylim([-1.2 1.2]); xlim([0 3.3]);
set(gca,'FontSize',fsize);

%% Fit a curve with degree degree and subtract from data
matrix = Ethz;

degree = 7;
fitted_polynomial = polyfit(step_array, matrix, degree);
curve_from_fit = polyval(fitted_polynomial, step_array);

figure; plot(step_array, matrix); hold on;
plot(step_array, curve_from_fit);
xlim([step_array(1) step_array(length(step_array))]);
grid on;

subtracted = matrix - curve_from_fit';
figure; plot(step_array, subtracted);
xlim([step_array(1) step_array(length(step_array))]);
grid on;

%% Low-pass filtering signal

lowpass_filtered = smooth(subtracted);
figure; plot(step_array, lowpass_filtered); grid on;
xlim([step_array(1) step_array(length(step_array))]);
title('Lowpass filtered data');
```

```
%% Apodization

figure; plot(step_array, lowpass_filtered); hold on;
L = length(step_array); window = max(lowpass_filtered)*tukeywin(L,1);
plot(step_array, window);
xlim([step_array(1) step_array(length(step_array))]);
title('Apodization cruve fitted to subtracted curve');
grid on;

figure; multiplied = lowpass_filtered.*window./max(lowpass_filtered);
plot(step_array, multiplied);
xlim([step_array(1) step_array(length(step_array))]);
title('Data points multiplied by apodization curve');
grid on;

%%  Compute the FFT of the terahertz pulse after cleaning up data
% This code follows the FFT MATLAB tutorial closely
% https://se.mathworks.com/help/matlab/ref/fft.html

c0 =3e8;
step_size_resolution = 2*0.963e-6;
temporal_resolution = step_size_resolution/c0;

Fs = 1/temporal_resolution;
T = 1/Fs;
L = length(step_array);

n = 2^nextpow2(L*4);
curve_from_fit = fft(multiplied,n);

f = Fs*(0:(n/2))/n;
P2 = abs(curve_from_fit/L);
P1 = P2(1:n/2+1);
P1(2:end-1) = 2*P1(2:end-1)*2;

P1 = P1.^2;

figure; hold on; plot(f*10^(-12),P1./(max(P1))); xlim([0 11]);
fsize = 16; xlabel('Frequency (THz)','FontSize',fsize);
ylabel('Spectral intensity','FontSize',fsize);
ylim([0 1.2]); xlim([0 9]); grid on;

%% Functions
```

```
function left_right_image = segment_left_right(image, limit)

    left_right_image = cell(1, 2);

    if limit == []
        [nbr_row_iteration_indexs, nbr_col_iteration_index] = size(image);
        middle_col_iteration_index = nbr_col_iteration_index/2;
    else
        middle_col_iteration_index = limit(1);
        [nbr_row_iteration_indexs, nbr_col_iteration_index] = size(image);
    end

    left_spot = image(:, 1:middle_col_iteration_index);
    right_spot = image(:, middle_col_iteration_index+1:nbr_col_iteration_index);

    left_right_image1, 1 = left_spot;
    left_right_image1, 2 = right_spot;

end

function draw_grid(image, block_size)

    [nbr_rows, nbr_cols] = size(image);
    imshow(image); hold on;

    col = block_size;
    while col < nbr_cols+block_size
        xline(col, 'Color', 'r', 'Linewidth', 1);
        col = col + block_size;
    end

    row = block_size;
    while row < nbr_rows+block_size
        yline(row, 'Color', 'r', 'Linewidth', 1);
        row = row + block_size;
    end

end

function cog = get_cog(image, mask)

    row_min = mask(1); row_max = mask(2);
    col_min = mask(3); col_max = mask(4);
    [nbr_rows, nbr_cols] = size(image);
    binary_image = image;
```

```
    for row = 1:nbr_rows
        for col = 1:nbr_cols
            if row >= row_min && row <= row_max
                    && col >= col_min && col <= col_max
                binary_image(row, col) = true;
            else
                binary_image(row, col) = false;
            end
        end
    end

    masked_image = regionprops(binary_image, image, 'WeightedCentroid');
    cog = masked_image(1).WeightedCentroid;

end

function draw_blocks(blocks, dim, image_contrast)

    for k = 1:length(blocks)
        subplot(dim, dim, k); imshow(blocks1, k); clim(image_contrast);
    end

end

function background = get_background(image, cog, probe_block_size,
        pump_block_size)

    cog_row = cog(2); cog_col = cog(1);
    row = cog_row + probe_block_size*5;
    half_block_size = cast(pump_block_size/2-1, 'single');
    background = image(row-half_block_size:row+half_block_size,
        cog_col-half_block_size:cog_col+half_block_size);

end

function blocks = segment_image(image, block_size, nbr_blocks,
        cog, box_stretch_factor)

    sf = box_stretch_factor;

    blocks = cell(1, nbr_blocks);

    half_block_size = cast(block_size/2-1, 'single');
    iteration_index = ceil(sqrt(nbr_blocks)/2);
    roi = sqrt(nbr_blocks);
```

```
row_iteration_index = iteration_index;
col_iteration_index = iteration_index;
row_cog = round(cog(2)); col_cog = round(cog(1));

store_index = ceil(nbr_blocks/2);
store_index_center_block = store_index;

loop_count = 0;
while row_iteration_index <= roi

    store_index = store_index_center_block + roi*loop_count;

    while col_iteration_index <= roi
        try
            blocks1, store_index = image(
                row_cog-half_block_size*sf(1):row_cog+half_block_size*sf(1),
                col_cog-half_block_size*sf(2):col_cog+half_block_size*sf(2));
            store_index = store_index + 1;
        catch
        end
            col_iteration_index = col_iteration_index + 1;
            col_cog = col_cog + block_size*sf(2);
    end

    col_iteration_index = iteration_index;
    col_cog = cog(1);
    store_index = store_index_center_block + roi*loop_count;
    while col_iteration_index > 1
        col_iteration_index = col_iteration_index - 1;
        col_cog = col_cog - block_size*sf(2);
        store_index = store_index - 1;
        try
            blocks1, store_index = image(
                row_cog-half_block_size*sf(1):row_cog+half_block_size*sf(1),
                col_cog-half_block_size*sf(2):col_cog+half_block_size*sf(2));
        catch
        end
    end

    row_iteration_index = row_iteration_index + 1;
    col_iteration_index = iteration_index;

    row_cog = row_cog + block_size*sf(1);
    col_cog = cog(1);
```

```
    loop_count = loop_count + 1;

end

row_iteration_index = iteration_index;
row_cog = cog(2);

loop_count = 1;
while row_iteration_index > 1

    row_iteration_index = row_iteration_index - 1;
    col_iteration_index = iteration_index;

    row_cog = row_cog - block_size*sf(1);
    col_cog = cog(1);

    store_index = store_index_center_block - roi*loop_count;

    while col_iteration_index <= roi
        try
            blocks1, store_index = image(
                row_cog-half_block_size*sf(1):row_cog+half_block_size*sf(1),
                col_cog-half_block_size*sf(2):col_cog+half_block_size*sf(2));
        catch
        end
        store_index = store_index + 1;
        col_iteration_index = col_iteration_index + 1;
        col_cog = col_cog + block_size*sf(2);
    end

    col_iteration_index = iteration_index;
    col_cog = cog(1);
    store_index = store_index_center_block - roi*loop_count;
    while col_iteration_index > 1
        col_iteration_index = col_iteration_index - 1;
        col_cog = col_cog - block_size*sf(2);
        store_index = store_index - 1;
        try
            blocks1, store_index = image(
                row_cog-half_block_size*sf(1):row_cog+half_block_size*sf(1),
                col_cog-half_block_size*sf(2):col_cog+half_block_size*sf(2));
        catch
        end
    end
```

```
        loop_count = loop_count + 1;

    end

end
```

A.3 MATLAB script for simulations and theoretical models

```
clc;
clear all;

% Class where I have gathered the Sellmeier equations I have used
in the project. Returns group delay and refractive index
sellmeier = sellmeier;

c0 = 3e8;
tau0 = 60e-15;
lambda0 = 1500e-9;
grooves_per_mm = 711.24;
lambda = 1/(grooves_per_mm*10^3);
omega0 = 2*pi*c0/lambda0;
theta_i = deg2rad(35);
nu0 = c0/lambda0;

%% Chirp parameter and group delay dispersion
l0 = linspace(0,10e-3);
mu = omega0^3*lambda^2./(2*4*pi^2*c0.*l0)*
    (1-((2*pi*c0/(omega0*lambda))-sin(theta_i))^2)^(3/2);

gdd = 1./mu;

figure;
plot(l0.*10^(3), gdd.*10^(30));
xlabel('Grating spacing (mm)', 'FontSize', 16);
ylabel('Group delay dispersion (fs)^2', 'FontSize', 16);
legend('711.24 grooves/mm, 35° incidence', 'FontSize', 16);
grid on;

figure;
plot(l0.*10^(3), mu.*10^(-24));
xlabel('Grating spacing (mm)', 'FontSize', 16);
ylabel('Chirp rate (THz/ps)', 'FontSize', 16);
legend('711.24 grooves/mm, 35° incidence', 'FontSize', 16);
grid on;
ylim([0 120]);
```

```
%% Pulse length
tau = tau0*sqrt(1 + (4./(mu.^2*(tau0*sqrt(log(2)))^4)));

figure; plot(l0.*10^3, tau.*10^(12));
xlabel('Grating spacing (mm)', 'FontSize', 16);
ylabel('Pulse duration (ps)', 'FontSize', 16);
legend('711.24 grooves/mm, 35° incidence', 'FontSize', 16);
grid on;

figure; plot(mu.*10^(-24), tau.*10^(12));
xlabel('Chirp rate', 'FontSize', 16);
ylabel('Pulse duration (ps)', 'FontSize', 16);
legend('711.24 grooves/mm, 35° incidence', 'FontSize', 16); xlim([0 100]);
grid on;
set(gca,'FontSize',16);

%% Beat frequency as a function of time delay
tau_chirp = linspace(0.5e-12, 3e-12, 6);
tau_delay = linspace(0.1e-12, 3e-12, 10000);

mu_short = 2/log(2)./(tau0^2*sqrt((tau_chirp/tau0).^2-1));

figure; hold on;
for i = 1:length(tau_chirp)

    nu_beat_mu = zeros(1,length(tau_delay));

    for j = 1:length(tau_delay)
            nu_beat_mu(j) = mu_short(i)*tau_delay(j)/2/pi;
    end

    plot(tau_delay*10^(12), nu_beat_mu*10^(-12));

end

xlabel('Delay (ps)','FontSize',16);
ylabel('Beat frequency (THz)','FontSize',16);

xlim([0 3]); ylim([0 8]);
legend('0.5 ps', '1 ps', '1.5 ps', '2 ps', '2.5 ps', '3 ps','FontSize',16);
grid on; set(gca,'FontSize',16);

%% Beat frequency as a function of chirp rate
tau_chirp = linspace(0.5e-12, 3e-12, 100);
```

```
tau_delay = linspace(0.5e-12, 2.5e-12, 5);
x_delay = tau_delay.*c0;

l0 = linspace(0,15e-3);
mu_short = 2/log(2)./(tau0^2*sqrt((tau_chirp/tau0).^2-1));

figure; hold on;
for i = 1:length(tau_delay)

    nu_beat_mu = zeros(1,length(tau_chirp));

    for j = 1:length(tau_chirp)
            nu_beat_mu(j) = mu_short(j)*tau_delay(i)/2/pi;
    end

    plot(mu_short.*10^(-24), nu_beat_mu*10^(-12));

end

xlabel('Chirp rate (THz/ps)','FontSize',16);
ylabel('Beat frequency (THz)','FontSize',16);
ylim([0 10]); xlim([15 90]);
legend('0.5 ps', '1 ps', '1.5 ps', '2 ps', '2.5 ps', '3 ps','FontSize',16);
grid on; set(gca,'FontSize',16);

%% Bandwidth as a function of chirped pulse duration
tau_chirp = linspace(0.5e-12, 5e-12);
tau = 60e-15;

for i = 1:length(tau_chirp)
    bw1(i) = sqrt(2)*sqrt(2*log(2))/(pi*tau_chirp(i));
end

figure; hold on;
plot(tau_chirp*10^(12), bw1*10^(-9));
xlabel('Chirped pulse length (ps)','FontSize',16);
ylabel('Bandwidth (GHz)','FontSize',16);
grid on; set(gca,'FontSize',16);

%% Intensity, THz electric field and spectrum
tau = 1.5e-12;
E0 = 1;
tau_delay = 1e-12;
omega0 = 2*pi*nu0;
tauF = 60e-15;
```

```
mu = 2./(sqrt((tau/tauF).^2-1)*(tauF*sqrt(log(2)))^2);

limit = 6*tau;

t = -limit:1e-17:limit;

E1 = E0*exp(-t.^2./(tau^2)).*exp(1i*omega0.*t).*exp(-1i*mu/2.*t.^2);
E2 = E0*exp(-(t+tau_delay).^2./(tau^2)).*
    exp(1i*omega0.*(t+tau_delay)).*exp(-1i*mu/2.*(t+tau_delay).^2);

E_tot = E1 + E2;
I = E_tot.*conj(E_tot);

% I = abs(E1).^2 + abs(E2).^2 + E1.*conj(E2) + conj(E1).*E2;

% Im = E0^2*exp(-2.*(t-tau_delay/2).^2./(tau^2));
% Ip = E0^2*exp(-2.*(t+tau_delay/2).^2./(tau^2));
% Icross = E0*exp(-(2.*t.^2)./tau^2).*exp(-(tau_delay^2/(2*tau^2))).*
    cos(omega0*tau_delay+mu*tau_delay.*t);
% I = Im + Ip + Icross;

a = mu*tau_delay/2/pi;
b = mu*tau_delay;

figure;
plot(t.*10^(12),I./max(I)); grid on;
xlabel('Time (ps)','FontSize',16);
ylabel('Normalized intensity','FontSize',16);
xlim([8 15]); xlim([-6 6]); ylim([0 1.2]);
set(gca,'FontSize',16);

% Terahertz pulse
Ethz = diff(I);
t_thz = t(1:length(Ethz));
figure; hold on;
Eplot = Ethz./max(Ethz); index = 0;
plot(t_thz.*10^(12),Eplot+index); grid on;
xlim([-15 10]); ylim([-1.2 1.2]);
xlabel('Time (ps)','FontSize',16);
ylabel('Normalized electric field','FontSize',16);
set(gca,'FontSize',16);

% Terahertz spectrum
% This code follows the FFT MATLAB tutorial closely
```

```
% https://se.mathworks.com/help/matlab/ref/fft.html
Fs = 1e17;
L = length(t_thz);

n = 2^nextpow2(L*4);
Y = fft(Ethz,n);

f = Fs*(0:(n/2))/n;
P2 = abs(Y/L);
P1 = P2(1:n/2+1);
P1(2:end-1) = 2*P1(2:end-1)*2;

P1 = P1.*conj(P1);
P1 = P1./max(P1);

i = 1;
while f(i) < 11*10^(12)
    i = i + 1;
end

P1 = P1(1:i);
f = f(1:i);

figure; hold on; plot(f.*10^(-12),P1); xlim([0 11]);
xlabel('Frequency (THz)','FontSize',16);
ylabel('Normalized spectral intensity','FontSize',16);
grid on;  xlim([0 10]);  ylim([0 1.2*max(P1)]);
set(gca,'FontSize',16);

%% Phase-matching and absorption effects for THz generation
cropped_P = P1(1:i); cropped_f = f(1:i);
f_last = cropped_f(i);

figure; plot(cropped_f.*10^(-12), cropped_P);
xlabel('Frequency (THz)','FontSize',16);
ylabel('Normalized spectral amplitude','FontSize',16);
grid on;  xlim([0 11]);  ylim([0 max(P1)]);
set(gca,'FontSize',16);

% (Group) refractive index of THz (IR) and absorption
% Data from Stillhart et. al. [21]
n0 = 2.226; K = 2/c0*10^12;
ai = [0.96 5.08 10];
wi = [0.648 1.024 2.702].*2*pi;
gammai = [0.37 0.8 7.17];
```

```
f = 3.5;
w = linspace(0, f*2*pi, 1000);
longw = linspace(0, 11*2*pi, 1000);
n_DSTMS = zeros(1, length(w));
alpha_DSTMS = zeros(1, length(w));

for l = 1:length(w)
    n = n0;
    alpha = 0;
    for i = 1:3
        wiwl = wi(i)^2-w(l)^2;
        n = n + (ai(i)*(wiwl)/((wiwl)^2+(2*gammai(i)*w(l))^2));
        alpha = alpha + (2*gammai(i)*ai(i))/
            ((wi(i)^2-w(l)^2)^2+(2*gammai(i)*w(l))^2);
    end
    n_DSTMS(l) = n;
    alpha_DSTMS(l) = w(l)^2*alpha;
end

alpha_DSTMS = alpha_DSTMS*K;

[n_optical,N_group] = sellmeier.organic('DSTMS',1.5);
N(1:length(longw), 1) = N_group;

% Read data for DSTMS in range 3.5-11 THz from Montemezzani et. al. [22]
% Merge vectors from the two sources and interpolate a curve
n_props = importdata('H:/My Documents/Exjobb/thz-props/n-to-inter.csv');
abs_props = importdata('H:/My Documents/Exjobb/thz-props/abs-to-inter.csv');

f_n = n_props.data(:,1)';
n = n_props.data(:,2)';

f_abs = abs_props.data(:,1)';
abs_v = (abs_props.data(:,2).*1000)';

f_temp_n = w/(2*pi);
n_temp = n_DSTMS;

f_temp_abs = f_temp_n;
abs_temp = alpha_DSTMS;

% Find index before the frequency in the first vector equals the first
% frequency in the second vector to merge (interpolation requires no
% duplicates and ascending or descending values only)
```

```
i = 1;
while f_temp_n(i) < f_n(1)
    i = i + 1;
end

f_temp_n = f_temp_n(1:i-1);
n_temp = n_temp(1:i-1);
n_tot = [n_temp, n];

i = 1;
while f_temp_abs(i) < f_abs(1)
    i = i + 1;
end

f_temp_abs = f_temp_abs(1:i);
abs_temp = abs_temp(1:i);
abs_tot = [abs_temp, abs_v];

f_n_tot = [f_temp_n, f_n];
f_abs_tot = [f_temp_abs, f_abs];

nbr_elements = length(cropped_P);

x = linspace(0,11,nbr_elements);
n_new = interp1(f_n_tot, n_tot, x, 'pchip');
f_n_tot_new = linspace(0,11,nbr_elements);

abs_new = interp1(f_abs_tot, abs_tot, x, 'pchip');
f_abs_new = linspace(0,11,nbr_elements);

% Compute and plot effective length, expression given by Schneider et. al. [31]
alpha_thz = abs_new;
alpha_laser = 0.7e2;
w = 2*pi*linspace(0,11,nbr_elements).*10^(12);
n_thz = n_new;
N_laser = N_group(1);
z = 0.54e-3;

A = exp(-alpha_thz.*z);
B = exp(-2.*alpha_laser*z);
C = 2.*exp(-(alpha_thz/2-alpha_laser)*z).*cos((w/c0).*abs(n_thz-N_laser)*z);
D = (alpha_thz./2-alpha_laser).^2;
E = (w./C).^2.*(abs(n_thz-N_laser)).^2;
lo = ((A + B - C)./(D+E)).^(1/2);
lo = real(lo)./(n_thz+N_laser);
```

```
figure; plot(w./(2*pi).*10^(-12), lo*10^3); grid on;
xlabel('Frequency (THz)'); ylabel('Effective length (mm)');
ylim([0 1]); xlim([0 11]);

% Multiply effective length with spectral amplitude of terahertz pulse
P1_new = cropped_P;

for i = 1:length(cropped_P)
    P1_new(i) = cropped_P(i)*lo(i);
end

P1_new = P1_new.*conj(P1);
P1_new = P1_new./max(P1_new);
figure(12); hold on; plot(w./(2*pi)*10^(-12), P1_new); %xlim([0 11]);
xlabel('Frequency (THz)','FontSize',16);
ylabel('Normalized spectral amplitude','FontSize',16);
grid on;  xlim([0 11]);  ylim([0 max(P1_new)]);
set(gca,'FontSize',16);

%% Refractive index and absorption for ZnTe and GaP
% ZnTe
fsize = 20;
c0 = 3e8;

f = linspace(0, 10e12);

eel = 6.5; f0 = 5.35e12; S0 = 2.0; gamma0 = 0.09e12;

n = zeros(1, length(f));
abs = zeros(1, length(f));
for i = 1:length(f)

    permitivitty_re = real(eel + S0*f0^2/(f0^2-f(i)^2-1i*gamma0*f(i)));
    permitivitty_im = imag(eel + S0*f0^2/(f0^2-f(i)^2-1i*gamma0*f(i)));

    n(i) = sqrt(permitivitty_re);
    abs(i) = sqrt(permitivitty_im);

end

abs = abs*4*pi.*f/c0;

syms lambda;
```

```
lambda_0 = 0.8;
n_func = inline(sqrt(4.27 + 3.01*lambda^2/(lambda^2-0.142)),'lambda');

dn_dl = inline(diff(n_func(lambda),lambda),'lambda');

n_optical = n_func(lambda_0);
N_group_optical = n_optical - lambda_0*dn_dl(lambda_0)

N(1:length(f), 1) = N_group_optical;

figure; plot(f.*10^(-12), n); grid on; hold on;
xlabel('Frequency (THz)', 'FontSize', fsize);
ylabel('Refractive index', 'FontSize', fsize);
plot(f.*10^(-12), N(1:length(f)), '--');
set(gca,'FontSize',fsize);

figure; plot(f.*10^(-12), abs.*10^(-3)); grid on;
xlabel('Frequency (THz)', 'FontSize', fsize);
ylabel('Absorption (mm^-^1)', 'FontSize', fsize);
set(gca,'FontSize',fsize);

% GaP
f = linspace(0, 20e12);

eel = 8.7; f0 = 10.98e12; S0 = 1.8; gamma0 = 0.02e12;

n = zeros(1, length(f));
abs = zeros(1, length(f));
for i = 1:length(f)

    permitivitty_re = real(eel + S0*f0^2/(f0^2-f(i)^2-1i*gamma0*f(i)));
    permitivitty_im = imag(eel + S0*f0^2/(f0^2-f(i)^2-1i*gamma0*f(i)));

    n(i) = sqrt(permitivitty_re);
    abs(i) = sqrt(permitivitty_im);

end

abs = abs*4*pi.*f/c0;

syms lambda;

lambda_0 = 0.75;
n_func = inline(sqrt(2.680 + 6.40*lambda^2/(lambda^2-0.0903279)),'lambda');
```

```
dn_dl = inline(diff(n_func(lambda),lambda),'lambda');

n_optical = n_func(lambda_0);
N_group_optical = n_optical - lambda_0*dn_dl(lambda_0)

N(1:length(w), 1) = N_group_optical;

figure; plot(f.*10^(-12), n); grid on; hold on;
xlabel('Frequency (THz)', 'FontSize', fsize);
ylabel('Refractive index', 'FontSize', fsize);
plot(f.*10^(-12), N(1:length(f)), '--');
set(gca,'FontSize',fsize);

figure; plot(f.*10^(-12), abs); grid on;
xlabel('Frequency (THz)', 'FontSize', fsize);
ylabel('Absorption', 'FontSize', fsize);
set(gca,'FontSize',fsize);
```